약학박사학위논문

Development of small-molecule chemical probes for target identification: Design, synthesis and biological evaluation of 1,3,4-oxadiazin-5(6*H*)-one and indolizino[3,2,*c*]quinoline scaffolds

표적 규명을 위한 화학 프로브의 개발: 1,3,4-oxadiazin-5(6*H*)-one과 indolizino[3,2,*c*]quinoline 골격의 화합물 설계, 합성 및 생물학적 평가

2019 년 8 월

서울대학교 대학원

약학과 약품제조화학전공

임 범 희

Abstract

Bumhee Lim
College of Pharmacy
Seoul National University

I. Metal-free and mild approach to 1,3,4-oxadiazol-2(3*H*)-ones *via* oxidative C-C bond cleavage of 1,3,4-oxadiazin-5(6*H*)-ones

A mild metal-free approach to 1,3,4-oxadiazol-2(3*H*)-ones via 1,3,4-oxadiazin-5(6*H*)-ones is described. This novel transformation, promoted by the electron-withdrawing *p*-substituents on the phenyl group at the α-carbonyl position, features a tandem reaction consisting of oxidative hydroxylation and C-C bond cleavage using molecular oxygen. The method utilizes K_2CO_3 in CH_3CN without any oxidants, transition metals, or additives, enabling the tunable synthesis of 1,3,4-oxadiazin-5(6*H*)-ones, 1,3,4-oxadiazol-2(3*H*)-ones, and α-ketoamides under mild aerobic conditions.

Keyword: 1,3,4-oxadiazol-2(3*H*)-one, 1,3,4-oxadiazin-5(6*H*)-one, Oxidative C-C bond cleavage, Metal free reaction, molecular oxygen

II. Target identification of a 1,3,4-oxadiazin-5(6*H*)-one anticancer agent *via* photoaffinity labelling

Rational design and synthetic feasibility are critical factors for the photoaffinity labelling (PAL) approach, which can identify protein targets of bioactive small molecules under native cellular conditions. In this study, we developed 1,3,4-oxadiazin-5(6*H*)-ones-derived photoaffinity labelling probes (**OPALs**) for LL-2003,

a previously reported potential anticancer agent against IGF-1R and Src. Our photoaffinity labelling strategy enabled successful photo crosslinking of the probes (**OPAL-6** and **OPAL-8**) with the target proteins in both mammalian cell lysates and live MCF7, A549, HepG2 and HeLa cells *in situ*. *In vitro* and *in situ* labelling demonstrated different patterns and expression levels of the proteome, and the strongest band for Src appeared in the A549 cell line. An in-gel fluorescence scan combined with MS/MS analysis of the IGF-1R overexpressed insect proteome labelled by **OPAL-6** and **OPAL-8** identified the binding location of the synthesized probes.

Keyword: Photoaffinity labelling, Target identification, 1,3,4-oxadiazin-5(6*H*)-ones, IGF-1R, Src

III. Novel turn-on fluorescent biosensors for selective detection of cellular Fe^{3+} in lysosomes

Iron-selective turn-on sensors are indispensable tools for understanding iron-related cell death processes and human diseases. In this study, we report a novel class of fluorescent sensors derived from an indolizino[3,2-*c*]quinoline scaffold that exhibit high selectivity for Fe^{3+} over other biologically abundant cations in cells, including Fe^{2+}, Al^{3+}, Zn^{2+}, and Mn^{2+}. **IQ44** displays fluorescence enhancement upon binding with Fe^{3+} in both ethanol and water. In aqueous solution, **IQ44** exists as 150 nm nanoparticles. The suppressed fluorescent emission of **IQ44** nanoparticles in water is switched on in response to Fe^{3+}, working as a turn-on nanoparticle sensor. Structure-property relationship analysis with IQ derivatives revealed that the

thiophene ring confers selectivity for Fe^{3+}. By installing thiophene in **IQ44** as a selectivity-tuning handle, fluorescence in the presence of Fe^{3+} resulting from restriction of intramolecular rotation (RIR) and increased torsion angle induced by iron demonstrated that **IQ44** is specifically localized in lysosomes, where it recognizes cellular Fe^{3+} in live cells, as determined using confocal microscopy. In addition, the increased fluorescent puncta of **IQ44** in the presence of Fe^{3+} colocalized well with the RFP-tagged LC3 proteins (pmRFP-LC3), enabling the detection of the autophagy process.

Keyword: Fluorescent biosensor, Fe^{3+} sensor, Indolizino[3,2,*c*]quinolone, Lysosome, Autophage

Student Number: 2014-31255

Table of Contents

II. Target identification of a 1,3,4-oxadiazin-5(6*H*)-one anticancer agent *via* photoaffinity labelling

III. Novel turn-on fluorescent biosensors for selective detection of cellular Fe^{3+} in lysosomes

List of Tables

I. Metal-free and mild approach to 1,3,4-oxadiazol-2(3*H*)-ones *via* oxidative C-C bond cleavage of 1,3,4-oxadiazin-5(6*H*)-ones

III. Novel turn-on fluorescent biosensors for selective detection of cellular Fe^{3+} in lysosomes

Experimental

List of Figures

I. Metal-free and mild approach to 1,3,4-oxadiazol-2(3*H*)-ones *via* oxidative C-C bond cleavage of 1,3,4-oxadiazin-5(6*H*)-ones

II. Target identification of a 1,3,4-oxadiazin-5(6*H*)-one anticancer agent *via* photoaffinity labelling

III. Novel turn-on fluorescent biosensors for selective detection of cellular Fe^{3+} in lysosomes

List of Schemes

I. Metal-free and mild approach to 1,3,4-oxadiazol-2(3*H*)-ones *via* oxidative C-C bond cleavage of 1,3,4-oxadiazin-5(6*H*)-ones

II. Target identification of a 1,3,4-oxadiazin-5(6*H*)-one anticancer agent *via* photoaffinity labelling

III. Novel turn-on fluorescent biosensors for selective detection of cellular Fe^{3+} in lysosomes

I. Metal-free and mild approach to 1,3,4-oxadiazol-2(3*H*)-ones *via* oxidative C-C bond cleavage of 1,3,4-oxadiazin-5(6*H*)-ones

1.1 Introduction

1.1.1 1,3,4-oxadiazol-2(3*H*)-ones and 1,3,4-oxadiazin-5(6*H*)-ones scaffolds

Heterocyclic compounds that possess nitrogen and oxygen hold tremendous promise in drug discovery as bioactive compounds. 1,3,4-Oxadiazin-5(6*H*)-ones and 1,3,4-oxadiazol-2(3*H*)-ones, *N,O*-containing five or six-membered heterocycles, have drawn substantial attention as prominent scaffolds found in numerous biologically active molecules.

Peptoids are a class of peptitomimetics that overcome the drawbacks of peptides such as hydrolysis by various enzymes. Despite the various advantages of the peptoids, there are some practical limits related to the structural flexibility and limited number of hydrogen bonds. 1,3,4-oxadiazin-5(6*H*)-ones scaffolds are rigidified structures of peptoids. Therefore, 1,3,4-oxadiazin-5(6*H*)-ones have drawn attentions as promising scaffolds, but only few biological activities have been reported, including monoamine oxidase (MAO) inhibitors,[1-3] human immunodeficiency virus (HIV) reverse transcriptase inhibitors,[4] and α-amino-3-hydroxy-5-methyl-4-isoxazolepropanoic acid (AMPA) receptor antagonists [5] (Scheme 1). Besides their underrepresented biological applications, 1,3,4-oxadiazin-5(6*H*)-one scaffolds are unique with the ability to incorporate various substitutes on C2-, N4-, and C6-positions. However, the majority of the previous works have synthesized derivatives of 1,3,4-oxadiazin-5(6*H*)-one only at the N4- or C2-positions.[1, 6-7] Recently, our group reported the C6-substituted 1,3,4-oxadiazin-5(6*H*)-one derivatives for anticancer activities.[8] Based on our molecular docking analysis of 2-aryl-4*H*-1,3,4-oxadiazin-5-one derivatives, the phenyl ring at the C6

position was considered to be the key part for biological effects because the phenyl group fits well into a hydrophobic pocket of the binding site with several key interactions with target kinases.[8] Thus, there still remain unmet needs for the development of more functionalized 1,3,4-oxadiazin-5(6*H*)-one derivatives, especially with the substituted phenyl groups on the C6 position along with a facile synthetic route to these compounds.

Meanwhile, 1,3,4-oxadiazol-2(3*H*)-ones are privileged scaffolds with a broad spectrum of biological applications, encompassing antibacterial agents,[9-10] serine hydrolase inhibitors,[11-14] openers of Ca^{2+}-activated potassium (Maxi-K) channels,[15] and antifungal agents [16] (Scheme 2). Most previous synthetic methods for 1,3,4-oxadiazol-2(3*H*)-ones have involved hazardous reagents or extreme conditions, including the use of phosgene,[17-18] radicals,[19] excess reagents,[20] heating at 180-190 ºC,[21] carbon monoxide and transition metals,[22-23] or oxidizing reagents.[24] Due to environmental sustainability and regulatory aspects, more attention has been placed on eliminating transition-metal contaminants in pharmaceutical synthesis.[25] Therefore, approaches for the mild and practical preparations of 1,3,4-oxadiazol-2(3*H*)-ones have yet to be explored.[24, 26-27]

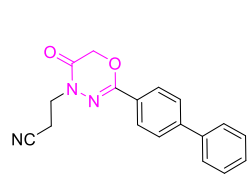

A

F. Mazouz, *et al.*,
Eur. J. Med. Chem., **1988**, *23*, 441
Monoamine oxidase (MAO) A inhibitor

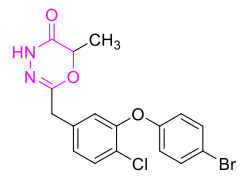

B

Z.K. Sweeney, *et al.*,
Bioorg. Med. Chem. Lett., **2008**, *18*, 4348
HIV reverse transcriptase inhibitor

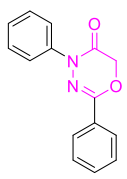

C

S. Hibi, *et al.*,
J. Med. Chem., **2012**, *55*, 10584
AMPA receptor antagonist

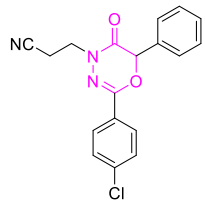

D

M. M. Alam, *et al.*,
Oncotarget, **2015**, *6*, 40598
IGF-1R and Src dual inhibitor

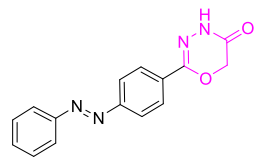

E

J. Lee, *et al.*,
Eur. J. Med. Chem., **2017**, *130*, 365
Monoamine oxidase (MAO) B inhibitor

Scheme 1. Structures of 1,3,4-oxadiazin-5(6*H*)-ones with biological activities.

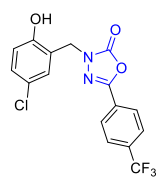

F

J. L. Romine, et al.,
J. Med. Chem., **2007**, *50*, 528
Ca^{2+}-activated potassium (Maxi-K) channels

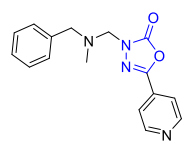

G

D. Zampieri, et al.,
Bioorg. Med. Chem., **2009**, *17*, 4693
Antibacterial agent

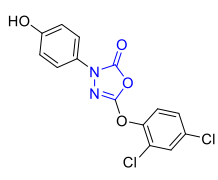

H

L. E. Kiss, et al.,
Med. Chem. Commun., **2011**, *2*, 889
Serine hydrolase inhibitor

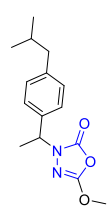

I

J. Z. Patel, et al.,
J. Med. Chem., **2013**, *56*, 8484
Serine hydrolase inhibitor

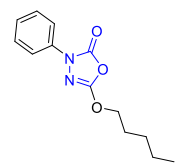

J

P. C. Nguyen, et al.,
Bioorg. Chem., **2018**, *81*, 414
Antimycobacterial activity

Scheme 2. Structures of 1,3,4-oxadiazol-2(3*H*)-ones with biological activities.

1.1.2 The metal-free and mild synthesis of 1,3,4-oxadiazol-2(3*H*)-ones

Molecular oxygen is a critical component of many biological systems in nature. Oxidation reactions are crucial in cells, particularly in metabolism. Significant progress has been made over the past decade to achieve direct C−H/C−C bond activations using molecular oxygen.[28-35] From a green chemistry perspective, stoichiometric amounts of toxic oxidants or expensive transition metals need to be avoided. Accordingly, metal-free reactions or milder conditions at room temperature utilizing molecular oxygen are highly desirable.[36-43] In particular, the direct cleavage of C(CO)-C(alkyl) or 1,2-dicarbonyl units under metal-free conditions is still challenging.[39, 44-45]

Herein, we report the metal-free and mild synthesis of 1,3,4-oxadiazol-2(3*H*)-ones via the aerobic oxidative cleavage of the C-C bonds of 1,3,4-oxadiazin-5(6*H*)-ones (Scheme 3).

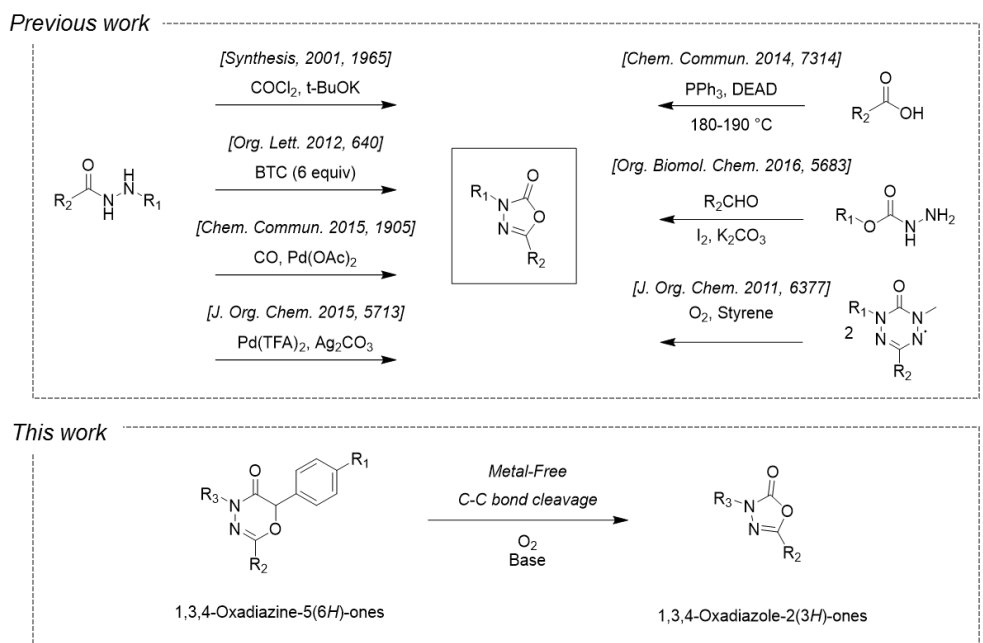

Scheme 3. C-C bond cleavage of 1,3,4-oxadiazin-5(6*H*)-ones.

1.2 Results and discussion

1.2.1 Optimization of oxidative C-C bond cleavage condition

Our initial studies commenced with an unexpected cleavage reaction of 1,3,4-oxadiazin-5(6*H*)-one (**3i**: R_1 = -NO_2, R_2 = -4-ClPh, R_3 = -CH_2CH_2CN) to 1,3,4-oxadiazol-2(3*H*)-one (**5a**: R_2 = -4-ClPh, R_3 = -CH_2CH_2CN) with K_2CO_3. To our surprise, **3i** reacted under very mild conditions to afford **5a** in high yield (88 %) without using any transition metals or stoichiometric amounts of oxidant. C-C bond cleavage generally involves base-induced fragmentations or a free-radical pathway catalysed by copper.[46-47] However, C-C cleavage without toxic metals or oxidants is less explored.

To further investigate this unprecedented reaction, we executed various control experiments (Table 1). Depending on the solvent, different sole products were obtained. The synthesis of 1,3,4-oxadiazol-2(3*H*)-one (**5a**) was preferred when CH_3CN was used as a solvent in the presence of K_2CO_3 (entry 1, 2, and 12). Along this reaction pathway, we detected an intermediate generated upon the consumption of **3i**. However, this intermediate gradually disappeared upon the formation of **5a**. The intermediate was isolated, and the structure was corroborated to be an α-ketoamide (**4**) by ^{1}H- and ^{13}C-NMR, IR, and HR-MS measurements. We hypothesized that compound **3i** underwent aerobic C-H hydroxylation using molecular oxygen and was further cyclized to yield **5a** via C-C bond cleavage. To investigate the effect of any transition-metal contaminants in K_2CO_3, a reaction using higher-purity K_2CO_3 (99.995 %, entry 2) was carried out, but compound **5a** was synthesized with a similar conversion rate. Therefore, the possibility of the transition

Table 1. Optimization of oxidative C-C bond cleavage condition.[a]

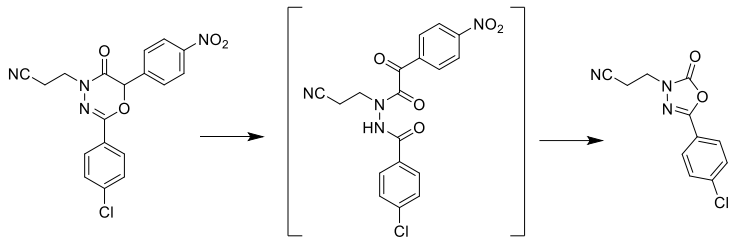

Entry	Base (equiv.)	Additive (equiv.)	Solvent	Time	Product [yield] [b] (ratio)
1	K_2CO_3		CH_3CN	4 h	**5a** [88]
2	K_2CO_3 [c]		CH_3CN	4 h	**5a** [89]
3	K_2CO_3	TEMPO (10.0)	CH_3CN	24 h	**4** [d]
4	K_2CO_3 (0.5)		CH_3CN	24 h	**3i : 4 : 5a** (2.6 : 1 : 1.6) [e]
5	K_2CO_3		DMSO	1 h	**4**
6	K_2CO_3	H_2O [f]	DMSO	1 h	**4**
7	*t*-BuOK (1.0)		DMSO	1.5 h	**4**
8	*t*-BuOK		DMSO	1 h	- [g]
9	*t*-BuOK		THF	1 h	- [g]
10	*t*-BuOK		CH_3CN	1 h	- [h]
11	K_2CO_3	CuI (0.2)	CH_3CN	1 h	**4**
12	K_2CO_3 [i]		CH_3CN	4 h	**5a** [85]
13	K_2CO_3		DMF	1 h	**4**
14	K_2CO_3		DCE	8 h	NR [j]
15	K_2CO_3		Toluene	8 h	NR [j]

[a] Reaction conditions: **3i** (0.026 mmol), base (10.0 equiv.) and solvent (1 mL) were stirred at room temperature in air until **3i** was completely converted to **4** or **5** as a single product, as monitored by TLC. [b] Yield of isolated products. [c] K_2CO_3 99.995 %. [d] See **Figure 1** for details. [e] Product ratio was analysed by LC/MS. [f] 1 drop of H_2O was added to the reaction. [g] Decomposed. [h] Side reaction product. [i] Reaction performed under dark conditions. [j] No reaction.

-metal-catalysed formation of **5a** was ruled out. We also investigated the involvement of radical reactions in the formation of **4** or in the C-C cleavage step. By using TEMPO as a radical scavenger, the reaction rates for the formation of both **4** and **5a** were also markedly decreased (entry 3 and Figure 1). Hence, the base-mediated fragmentation of anionic peroxide was ruled out. Reducing the amount of K_2CO_3 to 0.5 equiv. also generated **5a** but at a slower rate (entry 4). The reaction rate to **4** was accelerated by a stronger base (*t*-BuOK in DMSO or K_2CO_3 in DMSO, entry 5 and 7, respectively), suggesting the presence of an enolate formation step initiated by the base. However, the subsequent C-C cleavage reaction did not proceed under these conditions, even using 10.0 equiv. of *t*-BuOK in DMSO or THF (entry 8 and 9) or with the addition of water (entry 6). Termination at intermediate **4** in DMSO

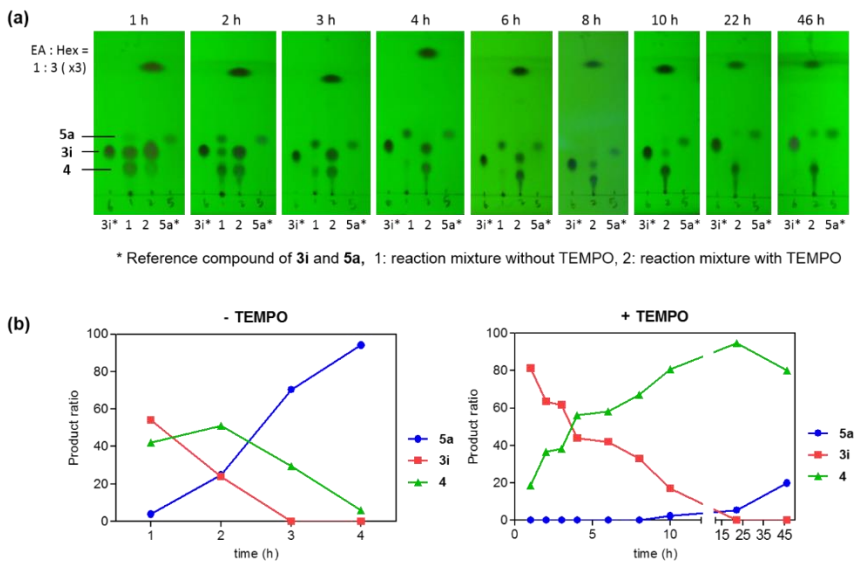

Figure 1. Quantitative TLC analyses demonstrating a reaction progress (from **3i** to **5a**) suppressed by TEMPO (10.0 equiv). **(a)** TLC analysis of the reaction mixture at different time intervals **(b)** Comparison of product ratio in the absence or presence of TEMPO.

and DMF indicates that the C-C cleavage step involved a radical reaction, as was evident from the suppression of the reaction by TEMPO (entry 3). To our surprise, use of CuI (20 mol %) accelerated the generation of intermediate **4**, but the following C-C cleavage reaction to **5a** did not proceed. This result confirmed that the C-C cleavage to **5a** was not a metal-catalysed reaction.

1.2.2 Scope of substrates for C-C bond cleavage reaction

Next, we turned our attention to the substrate scope. In previous work, we reported that 1,3,4-oxadiazin-5(6*H*)-ones were predominantly synthesized regardless of the *p*-substituents on the phenyl group at the C2 position.[8] In this work, we tested the effects of various substituents (-R_1) on phenyl group at C6 (carbonyl α-position) in the conversion of 1,3,4-oxadiazin-5(6*H*)-ones to 1,3,4-oxadiazol-2(3*H*)-ones (**5a**) (Table 2). Substrates **3f** and **3i** were completely converted to 1,3,4-oxadiazol-2(3*H*)-one (**5a**) (entry 3, 6) in the presence of K_2CO_3 after 8 h. Substrates **3g** and **3h** were also converted to **5a** but in lower yields (entry 4-5 and Figure 2). Meanwhile, the formation of **5a** was not observed with compounds possessing electron-donating groups (entry 1-2). Each 1,3,4-oxadiazin-5(6*H*)-one derivative also reacted in the absence of K_2CO_3, but the conversion to either **4** or **5a** was not detected in the absence of K_2CO_3.

Table 2. Scope of substrates for C-C cleavage reaction.

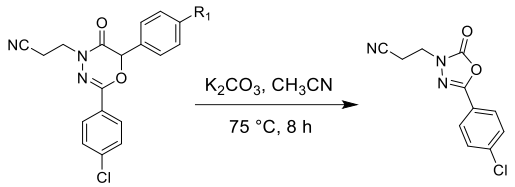

3 **5a**

Entry	Substrate	R_1	Product (ratio)		Yield (%) [a]
			K_2CO_3 (-)	K_2CO_3 (+)	
1	**3a**	OPh	NR [b]	NR	
2	**3b**	OCH_3	NR	NR	
3	**3f**	COPh	NR	**5a**	72
4	**3g**	$COCH_3$	NR	**3g : 5a** (1 : 2.0) [c]	22 : 38
5	**3h**	CF_3	NR	**3h : 5a** (1 : 1.1) [c,d]	34 : 41
6	**3i**	NO_2	NR	**5a** [e]	88

[a] Yield of isolated products. [b] No reaction. [c] Determined by ^{1}H-NMR analysis of the reaction mixture. [d] See Figure 2 for details. [d] Reaction conducted at room temperature.

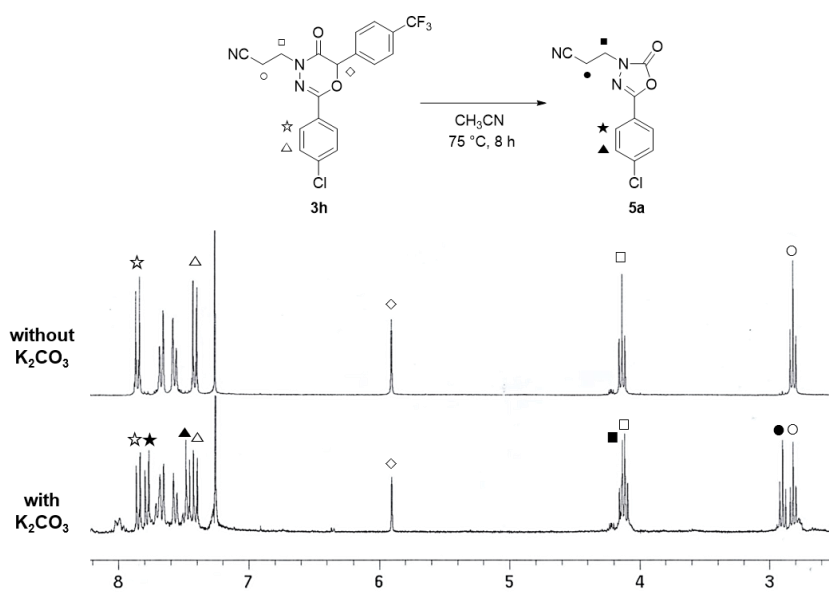

Figure 2. ^{1}H-NMR analysis of the reaction mixture (300 MHz, $CDCl_3$) in the presence or absence of K_2CO_3 (Table 2, entry 5).

1.2.3 Effects of substituents on the cyclized product selectivity

Intrigued by the dramatic observed substituent effects, we also examined the effects of substituents at the *p*-position on the phenyl group (-R_1) on the cyclized product selectivity, thereby enabling tunable syntheses of both compounds. We performed the cyclization reactions of nine substrates (**6a-6i**) with K_2CO_3 in CH_3CN at various temperatures (Scheme 4 and 5, Table 3 and Figure 3). The substituents (-R_1) of **6a-6i** dramatically affected the ratio of their cyclized products. The cyclization of compounds **6a-6e,** bearing electron-donating phenoxy, methoxy, phenyl, or acetoxy groups or -H on the phenyl ring (**6a-6e**, entry 1-15), yielded the corresponding 6-membered 1,3,4-oxadiazin-5(6*H*)-ones (**3a-3e**) as single products regardless of the reaction temperature. Furthermore, substrates with phenoxy and methoxy groups (**6a, 6b**) were spontaneously cyclized to **3a** and **3b** even without K_2CO_3 (Figure 4). When **6f-6i**, bearing electron-withdrawing substituents (-R_1) on the phenyl ring, were used as substrates, 5-membered 1,3,4-oxadiazol-2(3*H*)-one (**5a**) was simultaneously generated in addition to the 6-membered 1,3,4-oxadiazin-5-(6*H*)-one products (**3f-3i**, entry 16-26). Consistent with data in the Table 2, the electron-withdrawing nature of the *p*-substituent (-R_1) on the phenyl group of **6** obviously influenced the product ratio. The ratio of both cyclized products was also affected by the reaction temperature (Figure 3). In the reactions of **6f**, **6g** and **6h,** bearing -COPh, -$COCH_3$, and -CF_3 substituents, only 6-membered 1,3,4-oxadiazin-5(6*H*)-ones (**3f**, **3g**, and **3h**, respectively) were produced at room temperature, whereas the formation of 5-membered 1,3,4-oxadiazol-2(3*H*)-one (**5a**) was facilitated upon elevating the reaction temperature. Compound **6i** bearing -NO_2, a strong electron-withdrawing group, was exclusively transformed to 1,3,4-oxadiazol-2(3*H*)-one (**5a**) even at room

temperature (entry 26), whereas the 6-membered ring product (**3i**) was isolated at 0 ºC (entry 25). These data revealed that **5** was synthesized via **3**. The structures of both cyclized products were confirmed by X-ray crystallography (Figure 5).

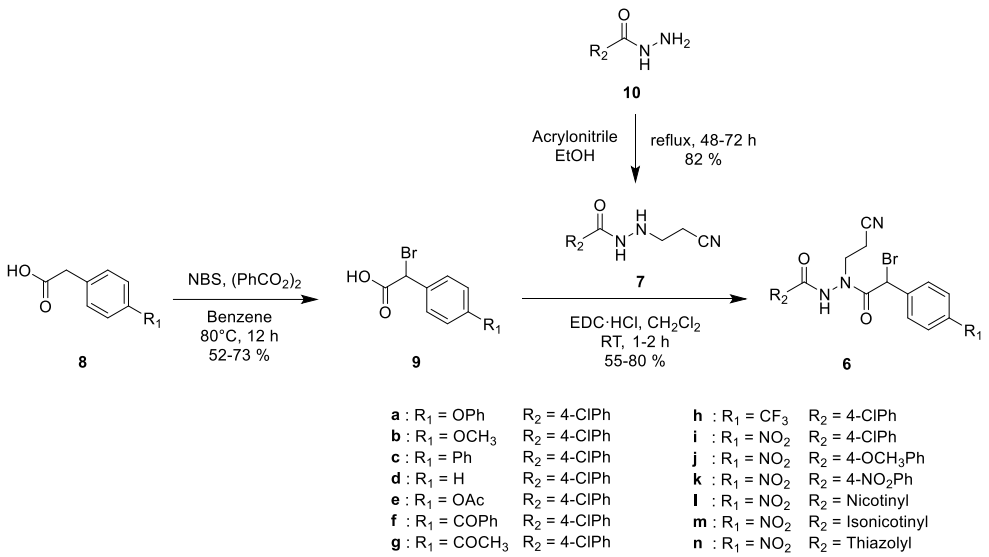

Scheme 4. Synthesis of **6a** and **6c-6n**.

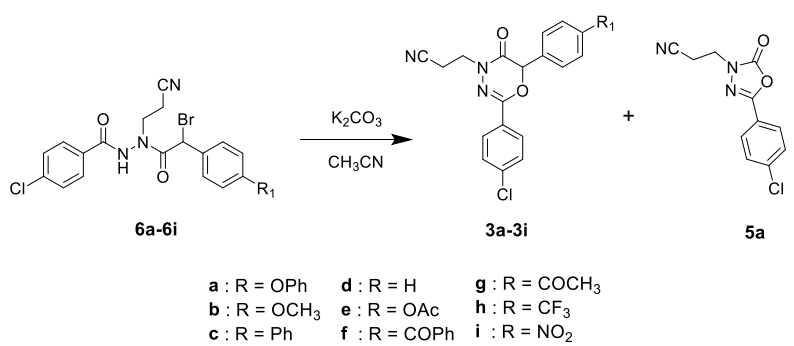

Scheme 5. Synthesis of 1,3,4-oxadiazin-5(6*H*)-ones (**3a-3i**) and 1,3,4-oxadiazol-2(3*H*)-ones (**5a**).

Table 3. Cyclization reactions of **6a-6i** at different reaction temperatures.[a]

Entry	Substrate	R_1	T (ºC)	Yield (%) [b]		Product [c] (**3** : **5**)
				3	**5**	
1			rt	85	n.d.[d]	**3a**
2	**6a**	OPh	50	87	n.d.	**3a**
3			75	88	n.d.	**3a**
4			rt	19 (54)[e]	n.d.	**3b**
5	**6b**	OCH_3	50	29	n.d.	**3b**
6			75	42	n.d.	**3b**
7			rt	86	n.d.	**3c**
8	**6c**	Ph	50	80	n.d.	**3c**
9			75	84	n.d.	**3c**
10			rt	89	n.d.	**3d**
11	**6d**	H	50	92	n.d.	**3d**
12			75	85	n.d.	**3d**
13			rt	60	n.d.	**3e**
14	**6e**	OAc	50	68	n.d.	**3e**
15			75	63	n.d.	**3e**
16			rt	75	n.d.	**3f**
17	**6f**	COPh	50	41	16	**3f : 5a** (2.3 : 1)
18			75	n.d.	42	**5a**
19			rt	98	n.d.	**3g**
20	**6g**	$COCH_3$	50	49	9	**3g : 5a** (5.0 : 1)
21			75	11	30	**3g : 5a** (1 : 2.7)
22			rt	97	n.d.	**3h**
23	**6h**	CF_3	50	68	trace	**3h : 5a** (18.5 : 1)
24			75	39	24	**3h : 5a** (1.3 : 1)
25	**6i**	NO_2	0	50	n.d.	**3i**
26			rt	n.d.	86	**5a**

[a] Reactions were conducted with **6** and 10.0 equiv. of K_2CO_3 in CH_3CN for 8 h. [b] Yield of isolated products. [c] ^{1}H-NMR spectroscopic analysis of the crude reaction mixture (see Figure 3). [d] Not detected. [e] Two-step yield from α-bromophenylacetic acid (see Scheme 4).

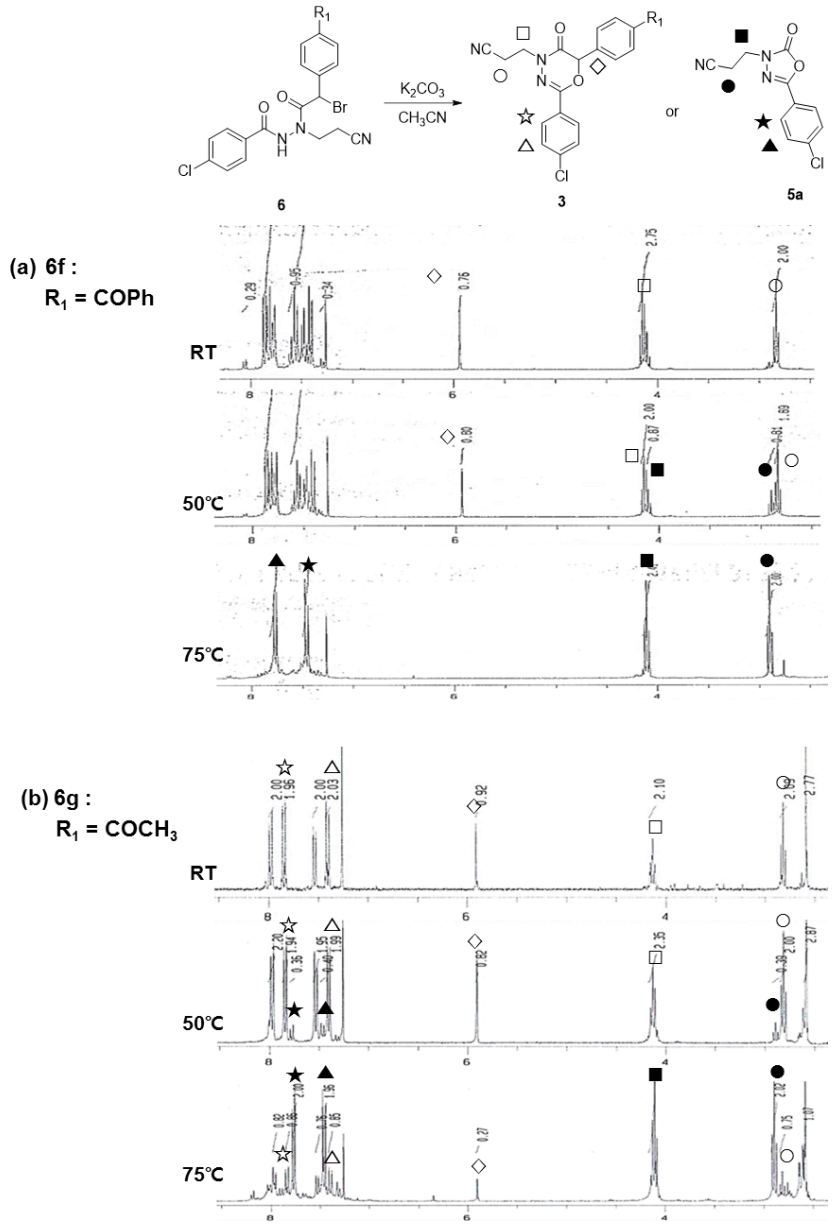

Figure 3-1. ^{1}H-NMR analysis of the reaction mixture (300 MHz, $CDCl_3$) of the cyclization products from **(a) 6f** (Table 3, entry 16-18) **(b) 6g** (Table 3, entry 19-21).

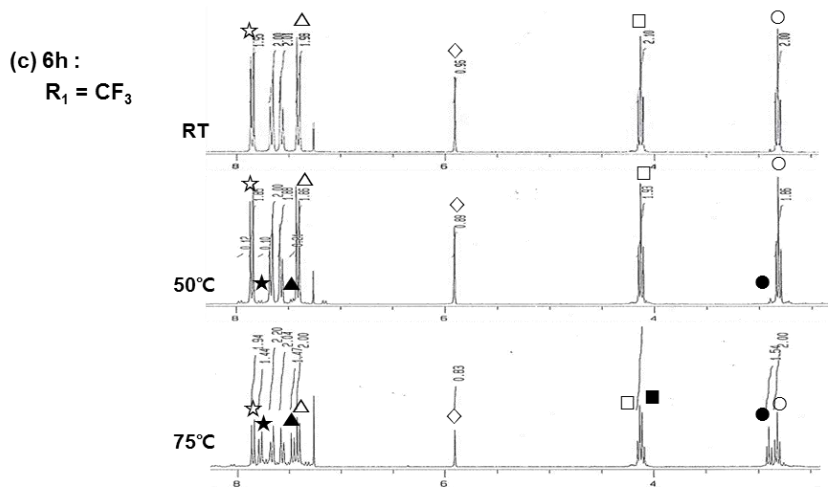

Figure 3-2. ^{1}H-NMR analysis of the reaction mixture (300 MHz, $CDCl_3$) of the cyclization products from **(c) 6h** (Table 3, entry 22-24) at room temperature, 50 ºC, and 75 ºC, respectively.

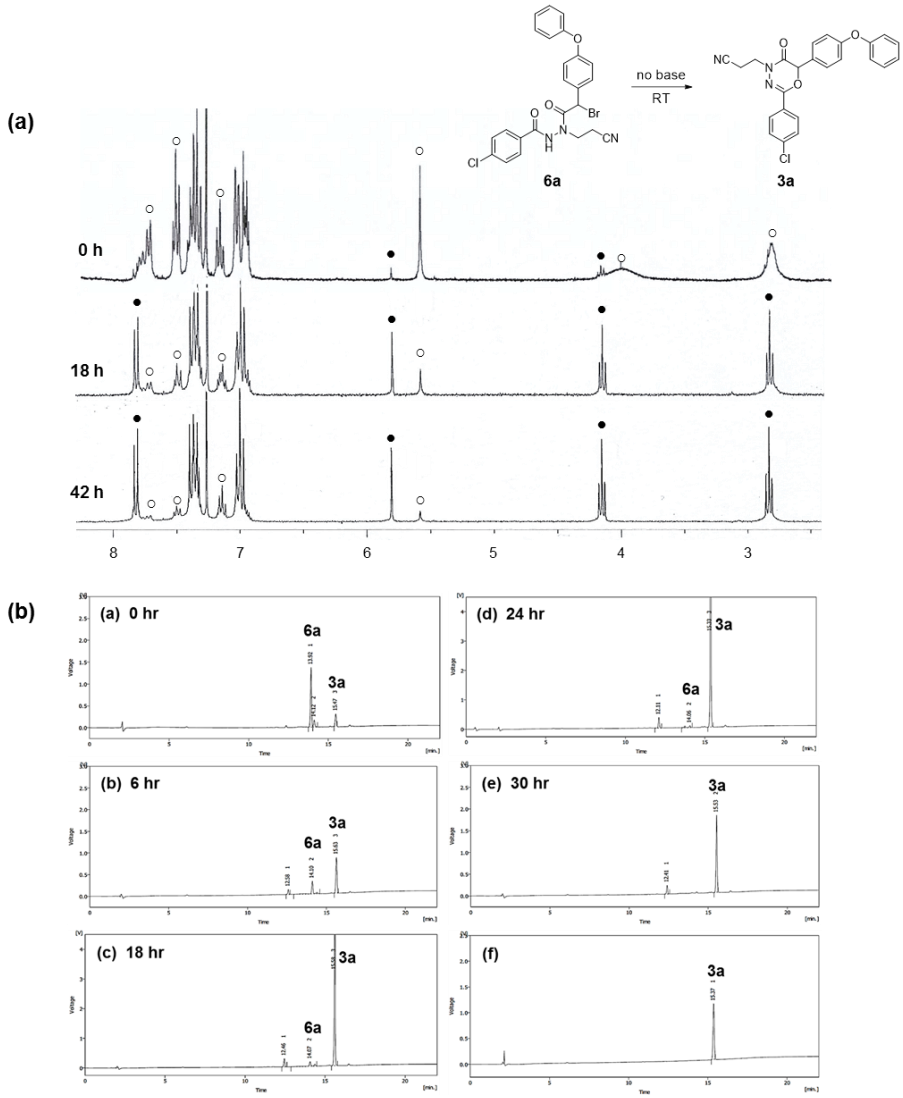

Figure 4-1. Progress of the spontaneous cyclization reaction of **6a** (○) to **3a** (●) without K_2CO_3 by **(a)** ^{1}H-NMR spectra (300 MHz, $CDCl_3$) and **(b)** HPLC analysis of the reaction mixture at different time intervals (f: compound **3a** as a reference).

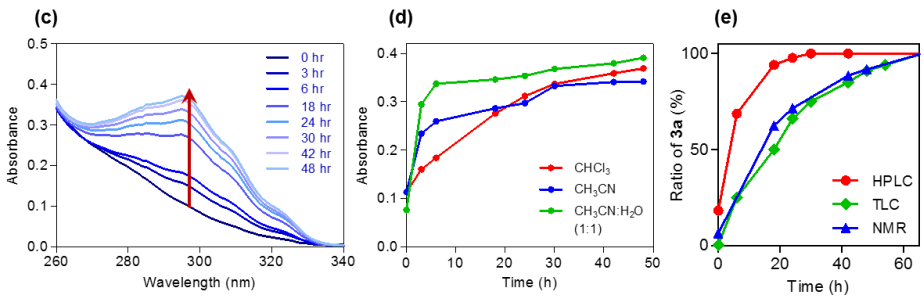

Figure 4-2. Progress of the spontaneous cyclization reaction of **6a** (○) to **3a** (●) without K_2CO_3 by **(c)** Time-dependent changes of UV-Vis absorption spectra, demonstrating the transformation of **6a** to **3a** in $CHCl_3$. **(d)** Time-dependent changes of Abs. at 294 nm in various solvents. **(e)** Comparison of kinetic profiles of the formation of **3a** monitored by HPLC, TLC and ^{1}H-NMR (red, green and blue), respectively.

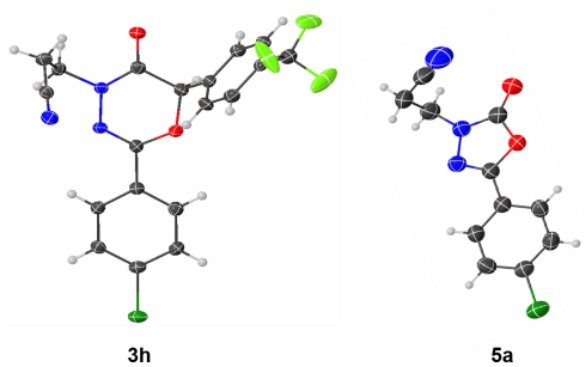

Figure 5. X-ray crystal structures of **3h** and **5a** (ORTEP diagrams).

1.2.4 Cyclized reactions with expanded substrate scope

We also examined the cyclization reactions of **6j**-**6q** for the expansion of the substrate scope, including electron-withdrawing and electron-donating groups on the phenyl ring and heteroaryl groups at the C2 position (**Table 4**, entry 1-6). Except the substrate **6n** with a thiazolyl group at R_2, the cyclization reactions yielded 5-membered 1,3,4-oxadiazol-2(3*H*)-ones (**5b**-**5e**). The substituent effects of R_2 on the C-C cleavage reaction were not as dramatic as we observed with R_1.

Table 4. Cyclized reactions of **6** with expanded substrate scope.

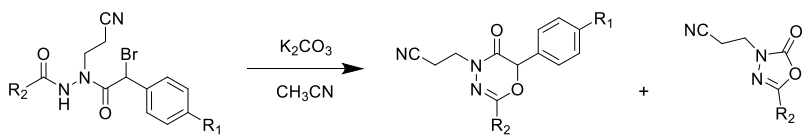

6j-q **3j-m** **5a-e**

Entry	Substrate	R_1	R_2	Temp. (ºC)	Time	Product (Yield %) [a]
1	**6j**	NO_2	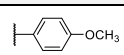	rt	20 h	**5b** (77)
2	**6k**		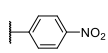	rt	8 h	**5c** (73)
3	**6i**			rt	8 h	**5a** (86)
4	**6l**			rt	8 h	**5d** (70)
5	**6m**			rt	8 h	**5e** (75)
6	**6n**			rt	2 h	**3j** (73)
7	**6o**	H	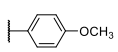	reflux	1-2 h	**3k** (73) [b]
8	**6p**		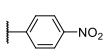	reflux	1-2 h	**3l** (82) [b]
9	**6d**			reflux	1-2 h	**3d** (86) [b]
10	**6q**			reflux	1-2 h	**3m** (76) [b]

[a] Yield of isolated products. [b] Previous reports.[8]

1.2.5 Proposed mechanism for the formation of 1,3,4-oxadiazol-2(3*H*)-ones

With these optimized results and the substrate scope in hand, we proposed a plausible mechanism for the formation of 1,3,4-oxadiazol-2(3*H*)-ones (**5**) from 1,3,4-oxadiazin-5(6*H*)-ones (**3**), as depicted in Scheme 6. The C6 position of the 1,3,4-oxadiazin-5(6*H*)-one (**3**) was deprotonated (step **A**) in the presence of base (K_2CO_3 or *t*-BuOK), and the resulting enolate was subsequently oxygenated under aerobic conditions, leading to the formation of a peroxide anion (**a**). Subsequent conversion to the α-hydroxylated form (**4'**) followed by tautomerization yielded the α-ketoamide (**4**), a ubiquitous structural unit in a variety of natural products.[48-49] Formation of the enol form of the amide (**4"**) could be possible, but our ^{13}C-NMR data indicated the presence of three carbonyl groups from the signals at 188.9, 167.0, and 165.6 ppm. Subsequent cyclization via C-C cleavage (step **C**) afforded **5**. LC/MS analysis showed benzoic acid as a fragmented counter group as well as intermediate **4** (Figure 6). Detection of benzoic acid rather than benzaldehyde indicates that a hydroxyl radical (•OH) is mechanistically involved. Reduction of peroxide by $P(OEt)_3$ might directly convert **b** to **4'** according to the report by Jiao and co-workers,[40] but no such additive was used in our case. Homolytic O-O scission (step **B**) followed by H• addition is likely to occur to generate **4'**, as reported in the study by Schoenebeck and co-workers.[32] Depending on the solvent, α-ketoamide was either exclusively obtained in high yield (DMSO, 83 %), or the reaction further proceeded to yield 1,3,4- oxadiazol-2(3*H*)-one (**5**) as a tandem reaction. The initiating step (**A**) could also be achieved by an autoxidation triggered by trace metal in the system.[47, 50-51] On the other hand, the formation of **5** via C-C bond cleavage was not observed using CuI (20 mol %) in our study (entry 11, Table 1). The isolated

α- ketoamide (**4**) was subject to C-C bond cleavage in the presence of K_2CO_3 (1.0 equiv.) and *t*-BuOOH (1.0 equiv.) at room temperature to yield **5**, which verifies the radical reaction of the C-C cleavage.

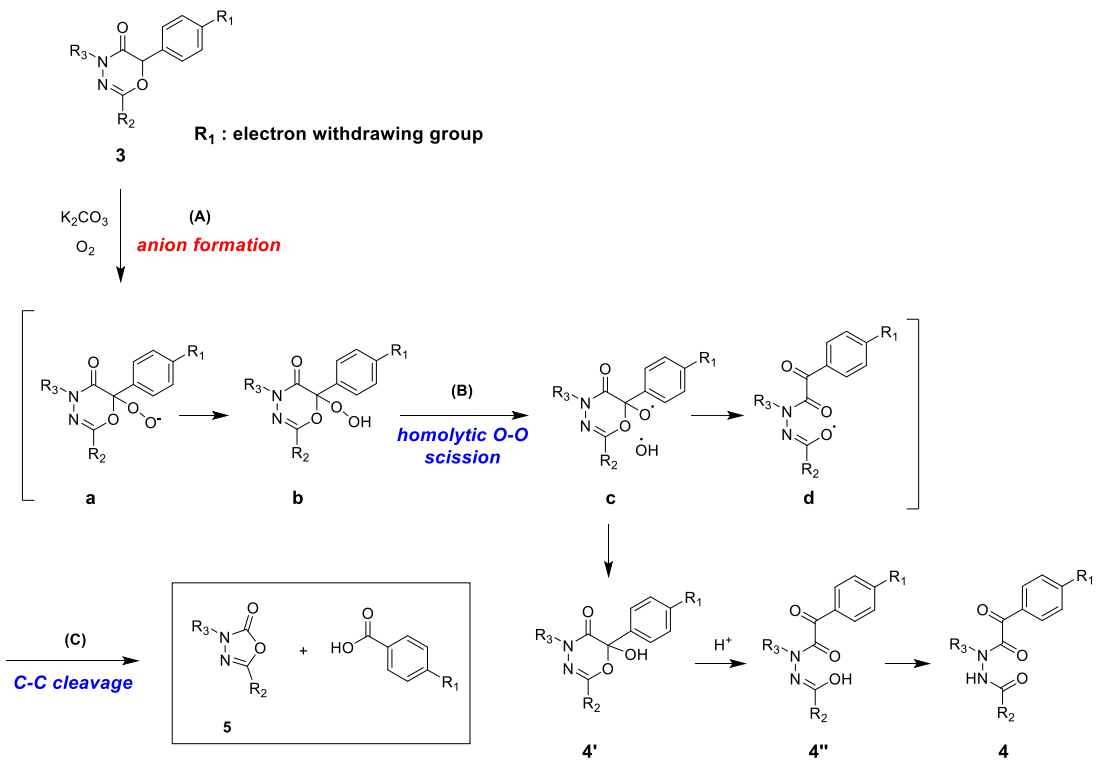

Scheme 6. Proposed mechanism of the conversion of **3** to **5**

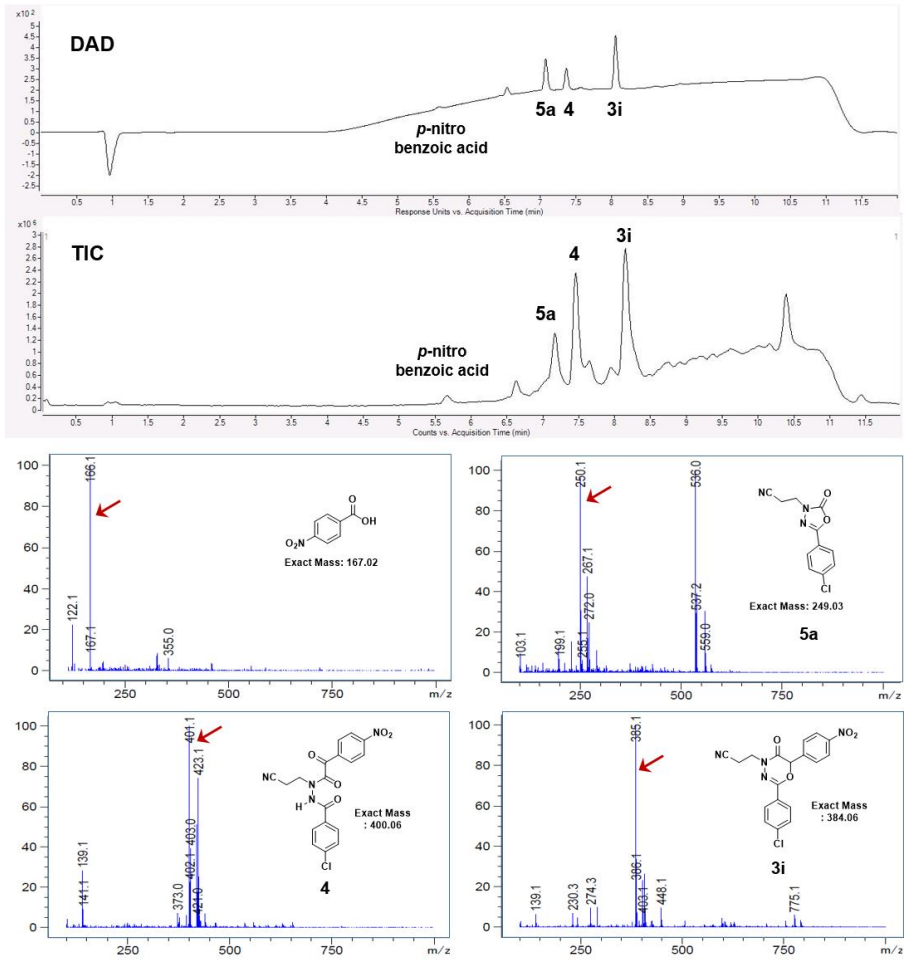

Figure 6. LC/MS analysis of the conversion of **3i** to **5a** after 24 h with K_2CO_3 in CH_3CN (entry 4 in **Table 1**).

1.2.6 Substituent effects on the product ratio

Figure 7 depicts the substituent effects (-R_1) on the product ratio. The conversion of the 6- to 5-ring product appeared to be affected by the efficiency of the aerobic oxidation at the α-carbonyl position of the 1,3,4-oxadiazin-5(6*H*)-one (step **A**) and the C-C cleavage step (step **C**), along with the release of a stable fragment by both inductive and resonance effects of the substituents (-R_1). In case of a -CF_3 substituents, which has only an inductive effect, the formation of **5** was decreased compared to the reaction with a -$COCH_3$ substituent (entry 4 vs. 5 in Table 2 and entry 20 vs. 23 in Table 3). 1,3,4-oxadiazin-5(6*H*)-ones (**3**) were predominantly synthesized (R_1 = H) regardless of the *p*-substituents on the phenyl group at the C2 position in our previous study (Table 4, entry 7-10).[8] Aliphatic substituents at the C6 position also mainly afforded 1,3,4-oxadiazin-5(6*H*)-ones.[52] Based on our data, the effect of R_2 on the formation of **5** appears to be less obvious than that of R_1.

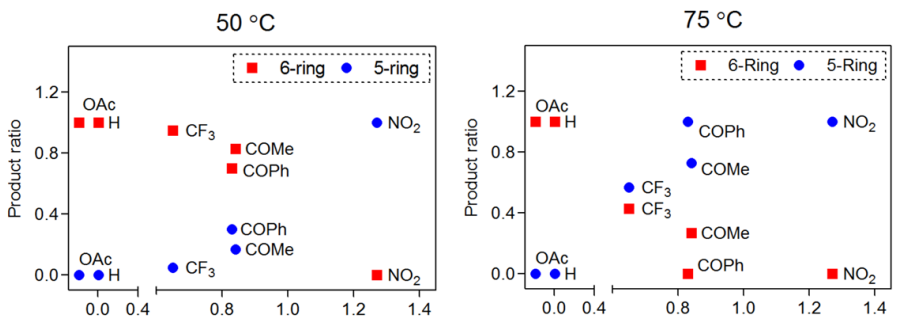

Figure 7. Correlation analysis of the substituent effects (-R_1) on the product ratio (σ^- vs. product ratio measured from the data in Table 3).[53-54]

1.3 Conclusion

We described a metal-free and mild approach to 1,3,4-oxadiazol-2(3*H*)-ones (**5**) via 1,3,4-oxadiazin-5(6*H*)- ones (**3**). Our results demonstrate that the synthesis of **5** is a tandem reaction via the α-hydroxylation of carbonyl compound **3** using molecular oxygen, followed by C-C bond cleavage without using a transition-metal catalyst or stoichiometric oxidant. The efficiencies of the aerobic oxidation and the C-C cleavage were found to be crucial to the formation of **5**, which was promoted by electron-withdrawing *p*-substituents on the phenyl group at the α-carbonyl position of the 1,3,4-oxadiazin-5(6*H*)-one. This approach for the selective construction of 1,3,4-oxadiazin-5(6*H*)-ones (**3**), 1,3,4-oxadiazol-2(3*H*)-ones (**5**), and α-ketoamides (**4**) is highly efficient, economical, and environmentally friendly without using hazardous reagents, transition metals, or oxidants. Given the wide applications of these structural motifs, our method will be of great significance to the understanding of metal-free C-C cleavage reactions, thereby paving the road for the α-cleavage of carbonyl compounds under mild conditions. Further studies towards the elucidation of the synthetic utility of this unprecedented C-C bond cleavage reaction are underway in our laboratory.

II. Target identification of a 1,3,4-oxadiazin-5(6*H*)-one anticancer agent *via* photoaffinity labelling

2.1 Introduction

2.1.1 Target identification in phenotype-based screening for drug discovery

The use of chemical probes to identify protein targets of bioactive small molecules in cells has been recognized as a powerful strategy to elucidate the function of proteins relevant to various human diseases along with their interactions with bound ligands under native cellular conditions.[55-58] Chemical probes are particularly critical for the pharmaceutical industry since many drug candidates derived from phenotype-based cellular assays suffer from a lack of knowledge regarding their direct binding with target proteins, which has been a bottle neck during the drug development process.[59] One of the important tools to corroborate the noncovalent interactions of drug candidates or bioactive small molecules with their target proteins is photoaffinity labelling (PAL) by the formation of direct covalent bonds between small molecules and target proteins via photocrosslinking based on their proximity.[60-63] In more recent cases, the unique binding site of the ligand and the detailed structural information of target protein have been elucidated by the photoaffinity labelling approach.[58, 64-65] In addition, the identification of direct binding protein targets of drug candidates *in vivo* can anticipate interactions with off-target proteins, thereby reducing the side effects or toxicity of drug candidates.[66] By using proteome-wide profiling methods with chemical probes, rapid identification of cellular off-targets has shown to be amenable to existing drugs or enzyme inhibitors.[67-71] However, incorporation of a photoaffinity or a reporter unit into the parent pharmacophore often results in changes in their native biological activity, such as cell permeability and binding affinity to target proteins. Therefore, rational

designs based on Structure-Activity Relationship (SAR) analysis and synthetic feasibility are essential for the success of chemical probes and derivatization of drug candidates.

Insulin-like growth factor 1 receptor (IGF-1R) has been shown to be important in mediating cellular signals for transformation, proliferation, survival and metastasis of cancer cells.[72-73] In our previous study, we synthesized LL-2003, a potential anticancer agent bearing a 1,3,4-oxadiazin-5(6*H*)-ones scaffold, as a dual inhibitor against IGF-1R and Src, based on the observation that Src activation is related to the resistance to IGF-1R inhibitors. Src, known as proto-oncogene tyrosine-protein kinase, also plays an important role in cancer progression.[74-75] Considering the high homology between human Src and IGF-1R, the developed dual inhibitor was well posed to the ATP binding site of both Src and IGF-1R in our molecular docking study.[8] Here, we designed photoaffinity labelling probes (**OPALs**) of LL-2003 to deconvolute the binding site and to identify interacting proteins under native cellular conditions.

2.1.2 Rational design of chemical probes

For successful labelling and identification of target proteins, we adopted a strategy in which the structural perturbations caused by introducing probing moieties into the parent core scaffold, 1,3,4-oxadiazin-5(6*H*)-ones, could be minimized. Three suitable positions in LL-2003 for installing probing units were selected using our docking analysis and SAR (Figure 1). Photoreactive groups, such as diazirine or benzophenone, which are activated upon UV irradiation to generate reactive species, were installed to form a covalent bond with adjacent amino acids in IGF-1R for

photoaffinity labelling.[76-77] The aliphatic diazirine unit was incorporated at site 1, whereas benzophenone was installed at site 2 inside the deep hydrophobic pocket of the protein. We performed the molecular docking study to make rational design regarding of the site 2 with the same method of our previous study.[8] **OPAL-10**, incorporated a benzophenone group instead of phenyl ring in LL-2003, was analyzed with the crystal structures of IGF-1R with ligands (PDB: 3D94) and resulting docking score was increased when a benzophenone group was added (Figure 2). Site 3 was chosen for the installation of a clickable terminal alkyne unit in replacement of –Cl or for a minimalist linker unit that attaches both a crosslinking tag and a reporter tag via Cu(I)-catalysed azide-alkyne cycloaddtion (CuAAC), the orthogonal click reaction.[78-79] The terminal alkyne unit was expected to be positioned toward the surface of the binding pocket, ensuring sufficient space to conduct a conjugation reaction with a bulky fluorophore unit.

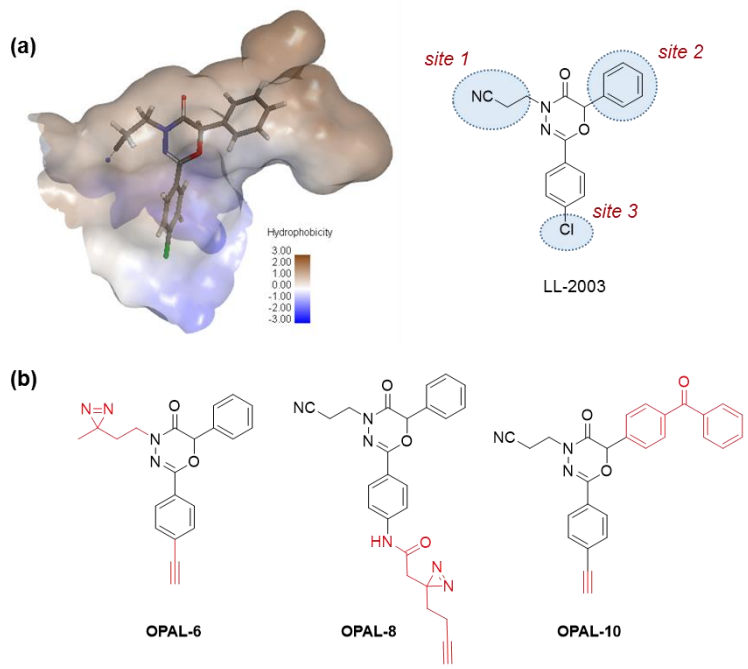

Figure 1. (a) Rational design of chemical probes for LL-2003 based on a molecular docking study with IGF-1R (PDB : 3D94).[80] The selected positions for photoaffinity and alkyne tags are highlighted. **(b)** Chemical structures of the synthesized **OPAL** probes.

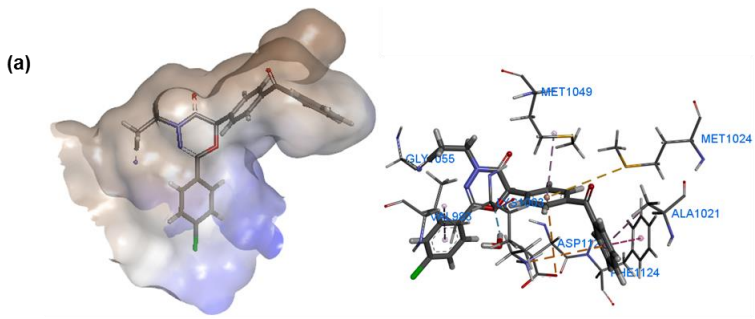

(b)

Ligand	Total_Score	Crash	Polar	Similarity
OPAL-10	9.6753	-0.9073	0.9057	0.538
LL-2003	6.8829	-0.605	1.0381	0.447

Figure 2. The molecular docking study **OPAL-10** with IGF-1R (PDB : 3D94). Surface and interaction diagram **(a)** and docking scores **(b)** in IGF-1R binding site.

2.2 Results and Discussion

2.2.1 Synthesis OPAL-6 and OPAL-10

Synthesis of **OPAL-6** and **OPAL-10** are described in Scheme 1-3. An amide coupling reaction between 4-ethynyl phenyl benzohydrazides possessing the clickable terminal alkyne group (**1a-b**) and α-bromophenyl phenyl acetyl unit (**2a-b**) followed by cyclization of **3a-b** under basic conditions afforded **OPAL-6** and **OPAL-10**, as shown in Scheme 1.

The intermediates for synthesis of **OPAL-6**, *tert*-butyl-(1,3-dioxoisoindolin-2-yl)carbamate (**13**), 2-(3-methyl-3*H*-diazirin-3-yl)ethanol (**14**), 4-ethynylbenzoic acid (**17**) were synthesized according to the procedure described in the previous report.[81-83] To introduce the diazirine moiety at site 1 in **OPAL-6**, the initial synthesis began from a reaction with a Boc-protected hydrazine and a phthalic anhydride (Scheme 2). We selected phthalic anhydride as a suitable protecting group since two different protecting groups need to be successively introduced on the two nitrogens of the hydrazine. After a Mitsunobu-type reaction with a primary alcohol

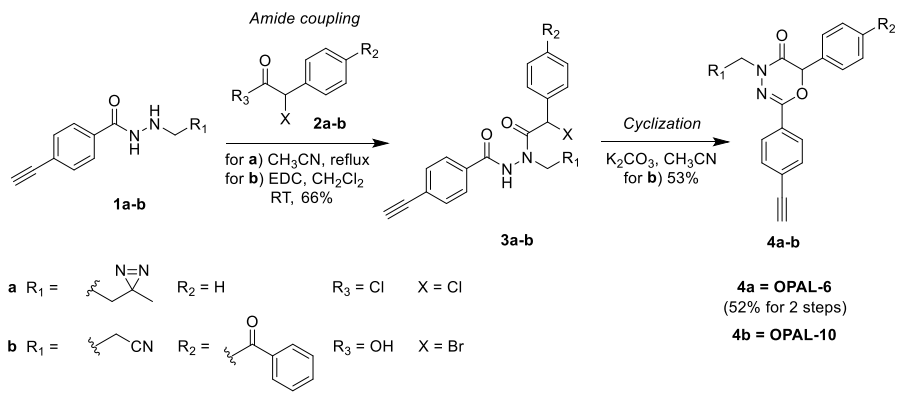

Scheme 1. Synthetic routes of **OPAL-6** and **OPAL-10**.

containing a diazirine moiety (**14**), deprotection of phthalimide with hydrazine and an amide coupling reaction with 4-ethynylbenzoic acid (**17**) followed by the deprotection of Boc yielded the intermediate **1a**, which contains both the diazirine and terminal alkyne groups. Further amide coupling and cyclization produced the final probe, **OPAL-6**, at an overall 8 % yield from **13**. For the synthesis of **OPAL-10**, we modified the α-halogenated phenyl acetyl unit to incorporate a benzophenone group by using **2b** prepared by the previously reported method (Scheme 3).[84-85]

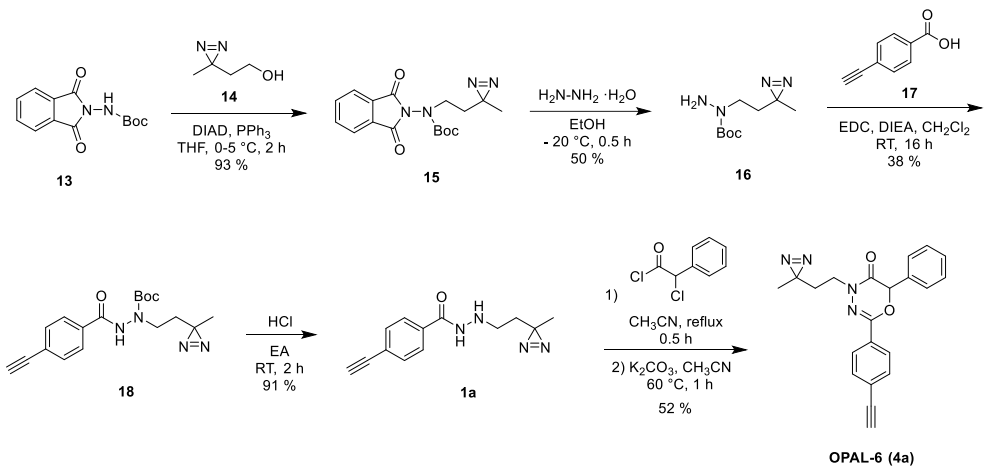

Scheme 2. Synthesis of **OPAL-6**

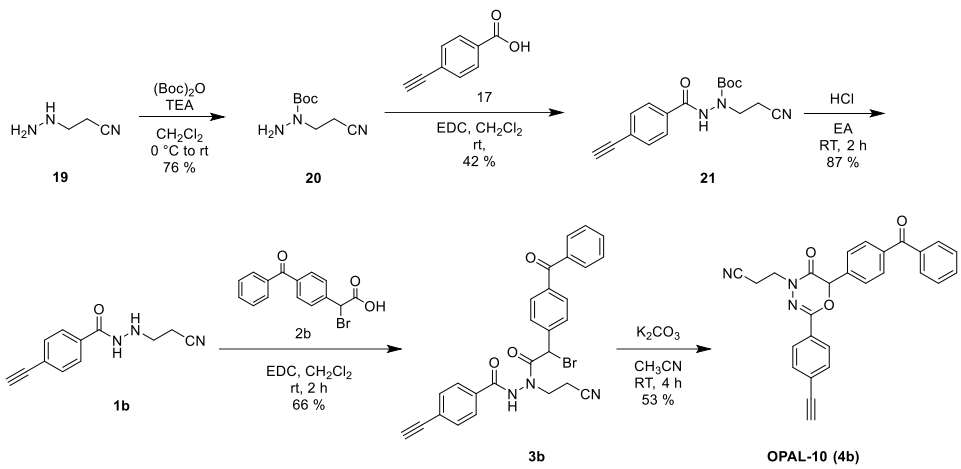

Scheme 3. Synthesis of **OPAL-10**

2.2.2 Synthesis of photoaffinity tag and OPAL-8

We also established a facile synthetic method for a dual-functioning affinity tag (**9**) containing a terminal alkyne and a diazirine group (Scheme 4). While one carbon shorter than the first minimalist linker by Yao and identical to Sieber's linker,[68, 70] the photoaffinity tag (**9)** was synthesized via a reduced number of steps under mild conditions (4 steps, overall yields 14%). The synthesis of **9** proceeded via a coupling reaction of 4-pentynoic acid with Meldrum's acid to generate compound **6** with an additional carbonyl group introduced. Further step-wise deprotection steps followed by diazirine synthesis using liquid ammonia and iodine afforded the desired affinity tag (**9**) (Scheme 4). Reduction of the previously reported **10** with tin chloride in ethanol followed by an amide coupling reaction with the dual-functioning affinity tag (**9**) yielded **OPAL-8** in 51% yield (Scheme 5).

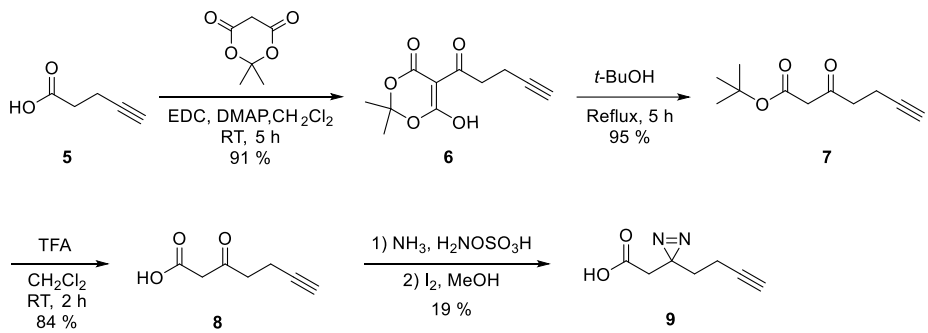

Scheme 4. Synthesis of the photoaffinity tag (**9**).

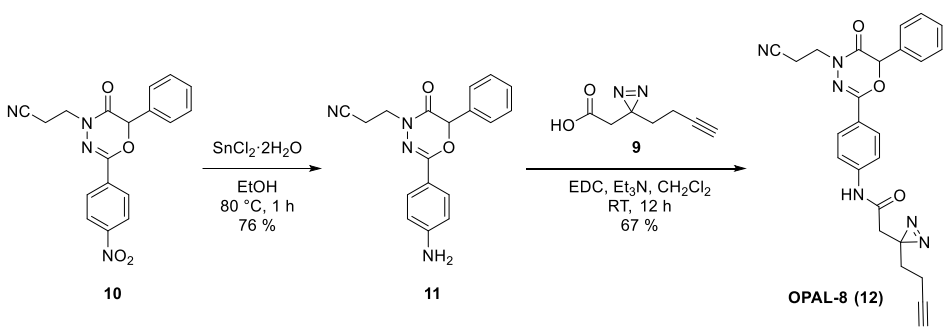

Scheme 5. Synthesis of **OPAL-8**.

2.2.3 Proteome reactivity profile of the OPALs

We evaluated the performance of three probes for their proteome labelling efficiency against cellular lysates of MCF7 cells. For *in vitro* labelling, MCF7 cell lysates were incubated with **OPAL-6**, **OPAL-8** and **OPAL-10** (50 μM) for 1 h to ensure they bound to their cellular targets and were subsequently exposed to the UV irradiation at 365 nm for 20 min at 4 °C to form covalent bonds between the probes and their target proteins. Labelled proteins were conjugated with rhodamine-azide under CuAAC conditions and were visualized using in-gel fluorescence scanning of

SDS-PAGE gels. As shown in Figure 3a, **OPAL-6** and **OPAL-8** resulted in a similar proteome labelling pattern. In addition, distinct fluorescent bands at 97 kDa and 60 kDa (red marks) in the **OPAL-6** and **OPAL-8** lanes were detected, which corresponded to the molecular weights of IGF-1R and Src, respectively. Western blot analysis with anti-IGF-1R- and Src antibodies confirmed that our probes were able to label both endogenous IGR-1R and Src in cell lysates. Meanwhile, **OPAL-10** failed to efficiently label proteins, although similar band intensities were observed in Coomassie-stained gels, indicating that similar amounts of samples were loaded. The excitation of the benzophenone group by UV light is known to be a reversible process.[86] In addition, sterically bulky benzophenone group may not be favorable for binding with the target, which might require a longer irradiation time for the photocrosslinking reaction than the diazirine moiety. Due to the poor crosslinking efficiency of **OPAL-10**, we proceeded with further biological evaluations of **OPAL-6** and **OPAL-8**.

We next labelled the endogenous proteome using both cell lysates and live cells of various mammalian cancer cell lines (A549, HepG2, HeLa and MCF7) to capture IGF-1R and Src in complex cellular proteomes (Figure 3b and 3c, respectively). For the in situ labelling experiments, cells were incubated with **OPAL-6** (10 μM) for 5 h, followed by irradiation with UV light prior to lysis. Then, the CuAAC reaction was conducted to allow rhodamine azide conjugation for visualization. As shown in Figure 3b and 3c, in-gel fluorescence scanning of rhodamine-labelled proteins revealed that **OPAL-6** was able to label Src both in cell lysates and live cells, although different proteome patterns were detected between *in vitro* and *in situ* labelling. In addition, the prominent fluorescent band from *in situ* labelled A549 cells

suggested that **OPAL-6** efficiently and selectively labelled the Src protein. On the other hand, the intensity of the band at 97 kDa for IGF-1R was weak and ambiguous, as the protein is buried in other abundant intrinsic proteins via nonspecific binding, presumably due to the low expression level of endogenous IGF-1R or the instability of the protein in the lysate, leading to a low abundance that was not sufficient to be detected by fluorescence.

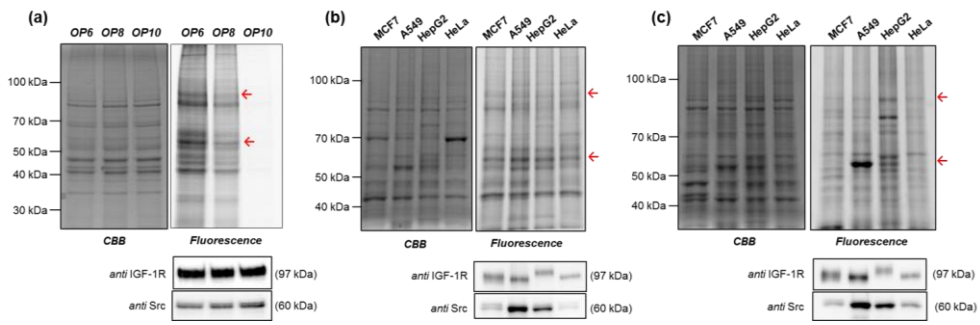

Figure 3. (a) Proteome reactivity profile of the synthesized probes in lysates of MCF7 cells. Cell lysate (50 μg) was treated with **OPAL** probes (50 μM) under 365 nm UV irradiation for 20 min, clicked with rhodamine-azide, and then subjected to SDS-PAGE and in-gel fluorescence scanning. **(b)** The *in vitro* (cell lysate) and **(c)** *in situ* (live cells) labelling profiles of **OPAL-6** in MCF7, A549, HepG2 and HeLa cells. For *in situ* labelling, cells were treated with **OPAL-6** (10 μM) for 5 h at 37 ºC and then exposed to UV light (365 nm) prior to lysis. The red arrows indicate labelled endogenous IGF-1R (upper) and Src (lower). In each labelling experiment, captured proteins, IGF-1R and Src, were confirmed by western blot analysis (bottom black boxes). CBB = Coomassie Brilliant Blue.

2.2.4 Identification of the binding location of OPAL-6

To ensure sufficient amounts of target proteins in cells for photocrosslinking, we also prepared insect cell lysates with recombinant human IGF-1R overexpressed by transfecting pFastBac1-IGF-1R. The detailed procedures for the preparation of the insect cell lysates are described in the Experimental section. The insect proteome labelled by **OPAL-6** and **OPAL-8** demonstrated a strong fluorescent band corresponding to the molecular weight of recombinant IGF-1R (Figure 4a), which indicates that detection of IGF-1R was dependent on the expression level. The labelling efficiency of the **OPAL-6** probe appears to be superior to that of **OPAL-8**, being consistent with the results of the photoaffinity labelling experiment on MCF7 cell lysates (Figure 3a). The difference in the fluorescence intensity of the detected bands between **OPAL-6** and **OPAL-8** was presumably due to the position of the installed affinity tag. The diazirine moiety in **OPAL-6** was designed to be located deeply inside the binding pocket based on the binding pose of LL-2003 in molecular docking studies.[80] On the other hand, the diazirine group of **OPAL-8** is located in the surface region of the binding site, making it difficult to selectively conjugate to proteins due to the loose contact between the carbene and amino acid residue. In addition, the flexibility of the terminal alkyl chain of **OPAL-8** decreases its ability to crosslink with proteins, although a shorter minimalist linker was adapted.

To further confirm the target protein and the binding locations of **OPAL-6** and **OPAL-8**, we used liquid chromatography-tandem mass spectrometry (LC-MS/MS) analysis of trypsin-digested peptide fragments of the protein band corresponding to the molecular weight of IGF-1R (59 kDa) detected in the in-gel fluorescence gel. IGF-1R was identified as the target protein that was labelled by both **OPAL-6** and

OPAL-8, with high percentages of coverage and scores (Figures 5-6). Distinguished labelling patterns were observed by **OPAL-6** and **OPAL-8**, as depicted on the structure of the human IGF-1R (PDB:3D94, Figure 4b).[14] The green parts in the ribbon structure represent the sequences matched by both **OPAL-6** and **OPAL-8,** whereas the yellow parts represent the sequence matched by only **OPAL-8**, not by **OPAL-6** (Figures 7). The data suggest that the formation of covalent bonds between **OPAL-6** and crosslinked amino acid of proteins resulted in the unmatched peptide sequence to the original protein sequence, revealing the binding location of the probe. The diazirine group is believed to be positioned near the yellow sequences, possibly in close contact with the side chain of Met1049 (Figure 4b, right).

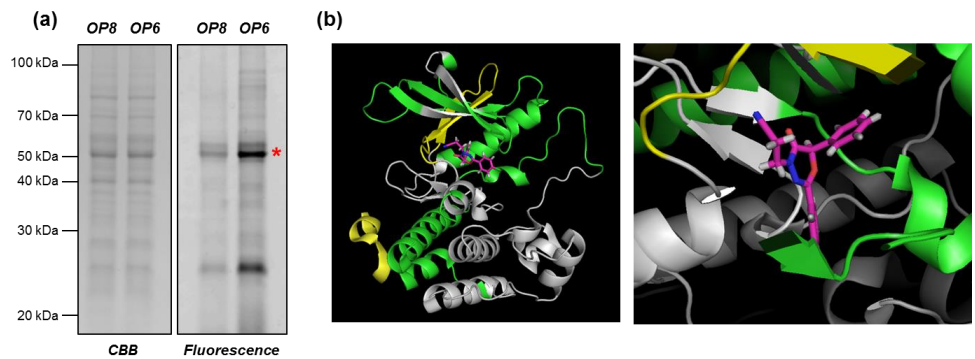

Figure 4. (a) In-gel fluorescence scan and CBB staining of SDS-PAGE-separated insect cell proteomes labelled by **OPAL-6** and **OPAL-8**. Insect cell lysates (200 μg) were treated with the probes (100 μM) under 365 nm UV irradiation for 20 min, clicked with rhodamine-azide, and then subjected to SDS-PAGE and in-gel fluorescence scanning. CBB = Coomassie Brilliant Blue. **(b)** The structure of human IGF-1R marked with the identified sequence from LC-MS/MS analysis (left) along with the predicted region of photocrosslinking of the diazirine group of **OPAL-6** (right).

	Accession	Coverage	# PSMs	# Peptides	# AAs	MW [kDa]	calc. pI	Score	Description
▶	IGF1R	51.06 %	327	30	517	59.4	5.57	1176.01	IGF1R

Sequence Comparison

	1	11	21	31	41	51	61	71	81	91	101
IGF1R	1	MSPILGYWKI	KGLVQPTRLL	LEYLEEKYEE	HLYERDEGDK	WRNKKFELGL	EFPNLPYYID	GDVKLTQSMA	IIRYIADKHN	MLGGCPKERA	EISMLEGAVL	DIRYGVSRIA
IGF1R	111	YSKDFETLKV	DFLSKLPEML	KMFEDRLCHK	TYLNGDHVTH	PDFMLYDALD	VVLYMDPMCL	DAFPKLVCFK	KRIEAIPQID	KYLKSSKYIA	WPLQGWQATF	GGGDHPPKSD
IGF1R	221	LVPRGSVYVP	DEWEVAREKI	TMSPELQDGS	FGMVYEGVAK	GVVKDEPETR	VAIKTVNEAA	SMRERIEFLN	EASVMKEFNC	HHVVRLLGVV	SQGQPTLVIM	ELMTRGDLKS
IGF1R	331	YLRSLRPEME	NNPVLAPPSL	SKMIQMAGEI	ADGMAYLNAN	KFVHRDLAAR	NCMVAEDFTV	KIGDFGMTRD	IYETDYYRKG	GKGLLPVRWM	SPESLKDGVF	TTYSDVWSFG
IGF1R	441	VVLWEIATLA	EQPYQGLSNE	QVLRFVMEGG	LLDKPDNCPD	MLFELMRMCW	QYNPKMRPSF	LEIISSIKEE	MEPGFRE			

Accession	MW [kDa]	calc. pI	Score	Description
gi194709190	**34.4**	**5.06**	**669.79**	**Chain A, Crystal Structure Of The Insulin-Like Growth Factor-1 Receptor Kinase In Complex With Pqip**
gi119608775	48.8	4.98	589.38	tubulin, beta 2C, isoform CRA_b [Homo sapiens]
gi27227551	49.9	4.92	565.40	class II beta tubulin isotype [Homo sapiens]
gi194381502	40.5	4.89	516.27	unnamed protein product [Homo sapiens]
gi84708830	50.1	4.89	383.82	TUBB6 protein [Homo sapiens]
gi2843123	49.8	5.10	380.78	alpha tubulin [Homo sapiens]
gi38014278	45.6	5.00	362.59	TUBB3 protein, partial [Homo sapiens]
gi530424971	34.1	4.84	317.34	PREDICTED: tubulin beta-6 chain isoform X2 [Homo sapiens]
gi119590106	9.2	8.98	142.29	hCG27371 [Homo sapiens]
gi119594722	166.9	6.30	61.73	CDC42 binding protein kinase gamma (DMPK-like) [Homo sapiens]
gi119569544	80.6	9.94	44.95	early B-cell factor 3, isoform CRA_a [Homo sapiens]
gi119613178	16.2	8.31	37.59	hCG2038390 [Homo sapiens]
gi119614552	12.2	9.74	36.43	hCG2041211 [Homo sapiens]
gi578810772	164.4	10.18	32.38	PREDICTED: LOW QUALITY PROTEIN: putative POM121-like protein 1-like [Homo sapiens]
gi530418321	49.8	5.00	28.48	PREDICTED: phosphatidate phosphatase LPIN3 isoform X2 [Homo sapiens]
gi316925459	11.8	6.76	25.41	anti-vaccinia virus immunoglobulin light chain variable region [Homo sapiens]
gi382546190	54.5	8.24	22.09	ATP synthase subunit alpha, mitochondrial isoform c [Homo sapiens]
gi13938355	55.4	5.58	18.80	ATP6V1B2 protein, partial [Homo sapiens]
gi444738009	18.0	9.76	18.67	alternative protein ZNF154 [Homo sapiens]
gi194378438	64.8	8.72	17.83	unnamed protein product [Homo sapiens]
gi194389700	70.6	8.51	16.30	unnamed protein product [Homo sapiens]
gi440575937	4.9	11.71	16.24	alternative protein NDST1 [Homo sapiens]
gi194389480	13.2	5.22	15.69	unnamed protein product [Homo sapiens]
gi193788274	23.9	9.14	15.17	unnamed protein product [Homo sapiens]
gi33624861	48.1	6.73	14.74	nesprin-2 isoform 2 [Homo sapiens]
gi119627920	46.1	5.07	14.74	retinoblastoma binding protein 4, isoform CRA_b [Homo sapiens]
gi47168965	15.1	5.97	14.54	Chain B, Crystal Structure Of Kv4.3 T1 Domain

Figure 5. Target identification of **OPAL-6** based on MS/MS analysis and on an in-gel fluorescence scan of the insect lysate shown in Figure 3(a).

	Accession	Coverage	MW [kDa]	calc. pI	Score	Description
⊞ ▶	IGF1R	53.00 %	59.4	5.57	478.97	IGF1R

Sequence Comparison

	1	11	21	31	41	51	61	71	81	91
IGF1R	1	MSPILGYWKI	KGLVQPTRLL	LEYLEEKYEE	HLYERDEGDK	WRNKKFELGL	EFPNLPYYID	GDVKLTQSMA	IIRYIADKHN	MLGGCPKERA	EISMLEGAVL
IGF1R	101	DIRYGVSRIA	YSKDFETLKV	DFLSKLPEML	KMFEDRLCHK	TYLNGDHVTH	PDFMLYDALD	VVLYMDPMCL	DAFPKLVCFK	KRIEAIPQID	KYLKSSKYIA
IGF1R	201	WPLQGWQATF	GGGDHPPKSD	LVPRGSVYVP	DEWEVAREKI	TMSRELGQGS	FGMVYEGVAK	GVVKDEPETR	VAIKTVNEAA	SMRERIEFLN	EASVMKEFNC
IGF1R	301	HHVVRLLGVV	SQGQPTLVIM	ELMTRGDLKS	YLRSLRPEME	NNPVLAPPSL	SKMIQMAGEI	ADGMAYLNAN	KFVHRDLAAR	NCMVAEDFTV	KIGDFGMTRD
IGF1R	401	IYETDYYRKG	GKGLLPVRWM	SPESLKDGVF	TTYSDVWSFG	VVLWEIATLA	EQPYQGLSNE	QVLRFVMEGG	LLDKPDNCPD	MLFELMRMCW	QYNPKMRPSF
IGF1R	501	LEIISSIKEE	MEPGFRE								

Accession	Coverage	MW [kDa]	calc. pI	Score	Description
gi27227551	37.98	49.9	4.92	421.45	class II beta tubulin isotype [Homo sapiens]
gi119608775	39.36	48.8	4.98	397.67	tubulin, beta 2C, isoform CRA_b [Homo sapiens]
gi221045918	33.73	46.5	4.93	324.33	unnamed protein product [Homo sapiens]
gi194373785	39.85	45.8	4.87	307.11	unnamed protein product [Homo sapiens]
gi194709190	**45.51**	**34.4**	**5.06**	**257.57**	**Chain A, Crystal Structure Of The Insulin-Like Growth Factor-1 Receptor Kinase In Complex With Pqip**
gi84708830	24.38	50.1	4.89	252.54	TUBB6 protein [Homo sapiens]
gi38014278	33.99	45.6	5.00	243.37	TUBB3 protein, partial [Homo sapiens]
gi2843123	37.86	49.8	5.10	233.88	alpha tubulin [Homo sapiens]
gi119621958	22.73	41.9	4.91	191.12	tubulin, beta 6, isoform CRA_a [Homo sapiens]
gi133777273	19.05	49.3	4.88	135.03	TUBB8 protein [Homo sapiens]
gi119590106	28.57	9.2	8.98	57.19	hCG27371 [Homo sapiens]
gi382546190	16.90	54.5	8.24	33.65	ATP synthase subunit alpha, mitochondrial isoform c [Homo sapiens]
gi119395750	9.32	66.0	8.12	31.80	keratin, type II cytoskeletal 1 [Homo sapiens]
gi89574029	10.56	48.1	5.07	27.40	mitochondrial ATP synthase, H+ transporting F1 complex beta subunit [Homo sapiens]
gi13938355	9.98	55.4	5.58	26.23	ATP6V1B2 protein, partial [Homo sapiens]
gi550545083	4.83	54.4	5.96	24.00	Chain A, Crystal Structure Of The Human Seryl-trna Synthetase In Complex With Ser-sa At 2.9 Angstrom Resolution
gi47168965	14.52	15.1	5.97	17.57	Chain B, Crystal Structure Of Kv4.3 T1 Domain
gi113197968	8.14	48.1	4.93	17.04	KRT9 protein [Homo sapiens]
gi119627920	6.83	46.1	5.07	16.34	retinoblastoma binding protein 4, isoform CRA_b [Homo sapiens]
gi189055353	4.26	57.2	6.99	16.13	unnamed protein product [Homo sapiens]
gi12006049	7.03	46.4	7.44	15.39	EF1a-like protein [Homo sapiens]
gi7768709	5.10	44.7	8.40	14.25	disintegrin-like and metalloprotease with thrombospondin type 1 motif, 5 [Homo sapiens]
gi194386730	6.54	41.1	5.01	12.95	unnamed protein product [Homo sapiens]
gi194389480	11.02	13.2	5.22	12.41	unnamed protein product [Homo sapiens]
gi480312198	5.86	25.5	5.30	11.81	Chain A, Structure Of The Npp2ac-alpha4 Complex
gi193787468	5.80	37.6	8.19	11.52	unnamed protein product [Homo sapiens]
gi213499333	5.54	49.6	8.60	10.83	unnamed protein product [Homo sapiens]

Figure 6. Target identification of **OPAL-8** based on MS/MS analysis and on an in-gel fluorescence scan of the insect lysate shown in Figure 3(a).

	1	11	21	31	41	51	61	71	81	91	
1	MSPILGYWKI	KGLVQPTRLL	LEYLEEKYEE	HLYERDEGDK	WRNKKFELGL	EFPNLPYYID	GDVKLTQSMA	IIRYIADKHN	MLGGCPKERA	EISMLEGAVL	OP8
	MSPILGYWKI	KGLVQPTRLL	LEYLEEKYEE	HLYERDEGDK	WRNKKFELGL	EFPNLPYYID	GDVKLTQSMA	IIRYIADKHN	MLGGCPKERA	EISMLEGAVL	OP6
101	DIRYGVSRIA	YSKDFETLKV	DFLSKLPEML	KMFEDRLCHK	TYLNGDHVTH	PDFMLYDALD	VVLYMDPMCL	DAFPKLVCFK	KRIEAIPQID	KYLKSSKYIA	OP8
	DIRYGVSRIA	YSKDFETLKV	DFLSKLPEML	KMFEDRLCHK	TYLNGDHVTH	PDFMLYDALD	VVLYMDPMCL	DAFPKLVCFK	KRIEAIPQID	KYLKSSKYIA	OP6
201	WPLQGWQATI	GGGDHPPKSD	LVPRGS//VYVP	DEWEVAREKI	TMSRELGQGS	FGMVYEGVAK	GVVKDEPETR	VAIKTVNEAA	SMRERIEFLN	EASVMKEFNC	OP8
	WPLQGWQATI	GGGDHPPKSD	LVPRGS//VYVP	DEWEVAREKI	TMSRELGQGS	FGMVYEGVAK	GVVKDEPETR	VAIKTVNEAA	SMRERIEFLN	EASVMKEFNC	OP6
301	HHVVRLLGVV	SQGQPTLVIM	ELMTRGDLKS	YLRSLRPEME	NNPVLAPPSL	SKMIQMAGEI	ADGMAYLNAN	KFVHRDLAAR	NCMVAEDFTV	KIGDFGMTRD	OP8
	HHVVRLLGVV	SQGQPTLVIM	ELMTRGDLKS	YLRSLRPEME	NNPVLAPPSL	SKMIQMAGEI	ADGMAYLNAN	KFVHRDLAAR	NCMVAEDFTV	KIGDFGMTRD	OP6
401	IYETDYYRKG	GKGLLPVRWM	SPESLKDGVF	TTYSDVWSFG	VVLWEIATLA	EQPYQGLSNE	QVLRFVMEGG	LLDKPDNCPD	MLFELMRMCW	QYNPKMRPSF	OP8
	IYETDYYRKG	GKGLLPVRWM	SPESLKDGVF	TTYSDVWSFG	VVLWEIATLA	EQPYQGLSNE	QVLRFVMEGG	LLDKPDNCPD	MLFELMRMCW	QYNPKMRPSF	OP6
501	LEIISSIKEE	MEPGFRE									OP8
	LEIISSIKEE	MEPGFRE									OP6

Figure 7. Comparison of the matched peptide sequences from the LC-MS/MS analysis of IGF-1R labelled by **OPAL-6** and **OPAL-8** (Figures 4-6).

2.3 Conclusion

In summary, we rationally designed and synthesized photo affinity labelling probes, **OPALs**, modified from LL-2003, which were previously reported to be dual inhibitors of IGF-1R and Src. Our photoaffinity labelling strategy enabled successful crosslinking with target proteins in both insect cell lysates and mammalian live cells, demonstrating the efficient and selective labelling of Src. **OPAL-6** and **OPAL-8**, which contain a diazirine photoaffinity tag, consistently performed better than **OPAL-10** in labelling cellular proteomes. The labelling capabilities of the probes varied depending on the position of the incorporated crosslinking moiety. **OPAL-6**, which has diazirine installed inside the binding pocket based on the binding pose of the parent LL-2003 in target proteins, was shown to be more efficient at crosslinking target proteins than **OPAL-8**, which has diazirine installed on the surface. We also identified the amino acid sequence with which **OPAL-6** reacted, and the crosslinking position in IGF-1R are suggested from this sequence. The data revealed by the **OPAL** probes in this study provide valuable information to better understand the efficient detection of target proteins and the location of binding sites of chemical probes.

III. Novel turn-on fluorescent biosensors for selective detection of cellular Fe^{3+} in lysosomes

3.1 Introduction

3.1.1 Fluorescent sensors for detection of Fe^{3+}

Fluorescent probes that detect cellular components or analytes in combination with high resolution confocal imaging techniques provide versatile tools for cell biology and disease diagnosis.[87-92] In addition to the general benefits of fluorescence spectroscopy, including non-invasiveness, convenience, and rapid detection, these probes have become indispensable tools for real-time monitoring of various cellular processes, including proliferation, differentiation, and cell death.[93-96] In particular, fluorescent sensors for metal ions can visualize and quantify metal ions in the cytoplasm or in specific organelles, revealing the information regarding the microenvironments in which they are located.[97-98]

Of the various metal ions, iron is one of the most abundant in the human body. It is ubiquitous in cells and plays vital roles in a variety of human diseases, particularly in anaemia, cancers, and neurodegenerative disorders including Parkinson's disease and Alzheimer's disease.[99-102] Therefore, modulation of intracellular iron can provide valuable insight to better understand iron-related cell death processes, including ferroptosis and autophagy.[103-105] Iron-selective probes can be used to visualize the distribution of labile iron in specific organelles involved in cellular iron trafficking or metabolism.[106-109] Recently, the importance of iron metabolism in cancer as well as in drug resistance has been explored with iron-chelating compounds.[110-111] For this purpose, fluorescent sensors that function as iron chelators as well as visualization probes would be immensely important to monitor

cellular iron.[98, 112-113] However, fluorescent sensors for Fe^{3+} are generally turn-off sensors due to the fluorescence-quenching properties of paramagnetic iron.

3.1.2 Aggregation-induced emission

Fluorescent probes with Aggregation-induced emission (AIE) or Aggregation-induced emission enhancement (AIEE) characteristics have emerged as a new, promising class of probes, allowing higher contrast in fluorescence bioimaging.[114-117] Enormous efforts have been dedicated to the development of novel fluorophores with AIE or AIEE characteristics.[118-121] These molecules exhibit weak fluorescence in dilute solutions but become highly emissive upon aggregation or in the solid state, which is due to the restriction of intramolecular motions/rotations upon aggregation. Until now, most AIE luminogens that have been explored comprise only a limited number of systems including tetraphenylethene (TPE) and hexaphenyl-silole (HPS).[119, 122] Novel chemical scaffolds with AIE characteristics and synthetic feasibility hold tremendous potential for the development of efficient sensors with enhanced biocompatibility and photostability.[123] Furthermore, the photophysical properties and structural fundamentals of AIE-driven sensors based on various luminogen chemical scaffolds have not been explored extensively.[124-126]

To date, the majority of reported Fe^{3+} sensors with AIE characteristics are still quenched upon the addition of metal ions.[120, 127-132] Turn-on fluorescent Fe^{3+} sensors with AIE characteristics would be highly valuable due to their broad possible applications in biological systems.[133-135] However, most AIE sensors require nanoparticle fabrication processes to be applied in aqueous media, particularly for bioimaging and drug delivery.[136-144] In addition, self-assembly of nanoparticles for

the desired turn-on switch in real-time imaging remains a challenge.[145-149] Despite the development of various organic nanoparticles as a new class of fluorescent probes with better biocompatibility, turn-on nanoprobes for selective Fe^{3+} sensing are very rare.[150-151] Here, we report the development of indolizino[3,2-*c*]quinoline (IQ)-based metal sensor, a turn-on fluorescent sensor (**IQ44**) with AIE properties (Figure 1). We hypothesized that a lone pair of electrons on the furan/thiophene rings of IQ are involved in the ligand-metal complex, enabling us to develop selective iron sensors.

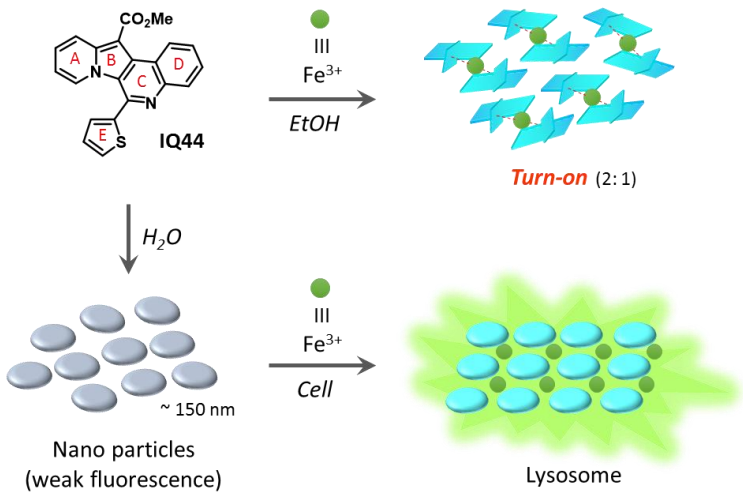

Figure 1. Structures of indolizino[3,2-*c*]quinoline based Fe^{3+} sensors and a schematic illustration of IQ turn-on sensor.

3.2 Results and discussion

3.2.1 Synthesis and metal sensing properties of IQ sensors

The synthesis of IQ metal sensors is depicted in Scheme 1.[152-153] With the synthesized compounds in our hands, we obtained the absorption and emission spectra in various solvents (Table 1). And we explored the metal sensing abilities of **IQ44** with 15 metal cations including Fe^{2+}, Fe^{3+}, Cd^{2+}, K^{+}, Na^{+}, Mg^{2+}, Ag^{+}, Al^{3+}, Zn^{2+}, Hg^{2+}, Mn^{2+}, Co^{2+}, Cu^{2+}, Pb^{2+}, and Cr^{3+}. **IQ44** exhibited significant fluorescence enhancement upon the addition of Fe^{3+} or Cr^{3+} in ethanol (Figure 2a). As Cr^{3+} is not a biologically relevant cation in cells, the observed cross-reactivity between Fe^{3+} and Cr^{3+} would not be critical for the application as biosensors.

Interestingly, **IQ44** exhibited an increase in emission in water as well, with the selectivity for Fe^{3+} being retained (Figure 2b). It is worth noting that both compounds exhibited distinct sensing properties for Fe^{3+} over Fe^{2+}. Job plot analysis of the UV-Vis spectra indicated that the stoichiometry of **IQ44** to Fe^{3+} was 2:1 (Figure 2c).

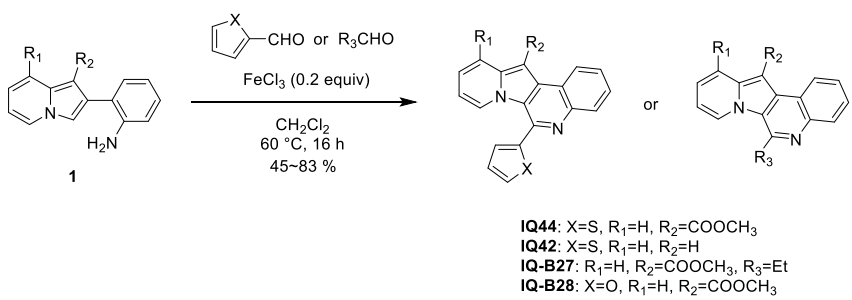

Scheme 1. General synthesis of indolizino[3,2-*c*]quinoline derivatives

Table 1. Optical properties of indolizino[3,2-*c*]quinoline-derived Fe^{3+} sensors.

Compound	λ_{abs} (nm) [a]	λ_{em} (nm)			ε_{max} ($M^{-1}cm^{-1}$)
		DMSO	EtOH	H_2O	
IQ44	366, 384	475	470	493	12900
IQ42	420, 442	509	489	539	10700
IQ-B27	354, 372	439	435	453	11100
IQ-B28	366, 383	472	467	480	11300

[a] in DMSO solution.

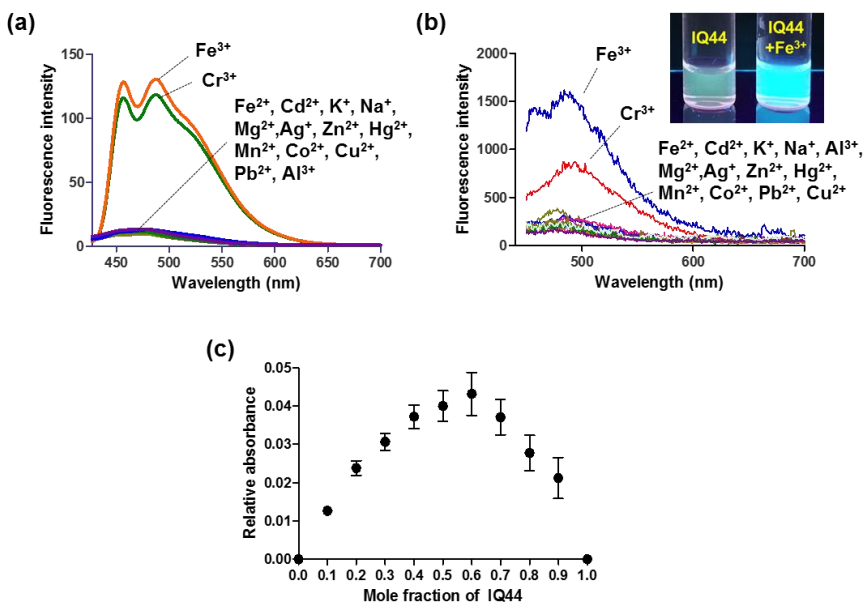

Figure 2. (a) Turn-on fluorescence response of **IQ44** (2 μM) in the presence of various metal ions (40 μM) in ethanol after 60 min (λ_{ex} = 417 nm). **(b)** Fluorescence response of **IQ44** (4 μM) in the presence of various metal ions (100 μM) in water measured after 30 sec. λ_{ex} = 422 nm. Photos of **IQ44** in response to Fe^{3+} in water. **(c)** Job plot analysis of **IQ44**-Fe^{3+} complexes in ethanol. The total concentrations of **IQ44** and Fe^{3+} were 10 μM. The monitored wavelength was 383 nm.

3.2.2 IQ44 as a nanoparticle sensor for Fe^{3+} in water

Because the selective turn-on response of **IQ44** for Fe^{3+} against other metal cations in water would be enormously beneficial for its further application as a biosensor, we focused on elucidation of the turn-on sensing mechanism of **IQ44** in water. As opposed to the severe quenching effect of conventional fluorophores in highly concentrated solutions, emission from **IQ44** at a high concentration (0.5 mM) in water was not diminished, indicating AIE properties. The AIE properties of **IQ44** were investigated in water/THF mixed solutions and compared to those of **IQ-B27**, a derivative without the thiophene (Figure 3-5). The emission of **IQ44** was enhanced by increasing the water fraction up to 80 % due to the formation of organic aggregates. Meanwhile, the emission intensity of **IQ-B27** was much higher than that of **IQ44** and was highest at 70 % of the water fraction. The mixed 80 % water solution of **IQ44** remained emissive even after 15 days at room temperature, indicating a stabilized emissive state of the aggregates was induced by restriction of intramolecular rotation (RIR). However, the RIR process was compromised at > 80 % water. Dynamic light scattering (DLS) revealed that **IQ44** and **IQ-B27** in aqueous solution at 10 μM formed nanoparticles with average particle sizes of 151 ± 13 nm and 132 ± 6.4 nm, respectively (Figure 3). The size of the particles was lower with higher water content (Figure 4a), reflecting solvent-driven assembly.[25] The solid state emission and quantum yields (QY) of **IQ44** and **IQ-B27** are shown in Figure 3 and Table 2. Note that the fluorescence QY of **IQ-B27** is much higher than that of **IQ44** (40 vs 3.0 %) in solution, which suggests that the rotation of the thiophene ring in **IQ44** serves as a nonradiative relaxing pathway in solution. The suppression of this rotation of the thiophene ring in **IQ44** by Fe^{3+} blocked the nonradiative energy

dissipation pathway, resulting in high emission from the ABCD ring, as shown in **IQ-B27**.

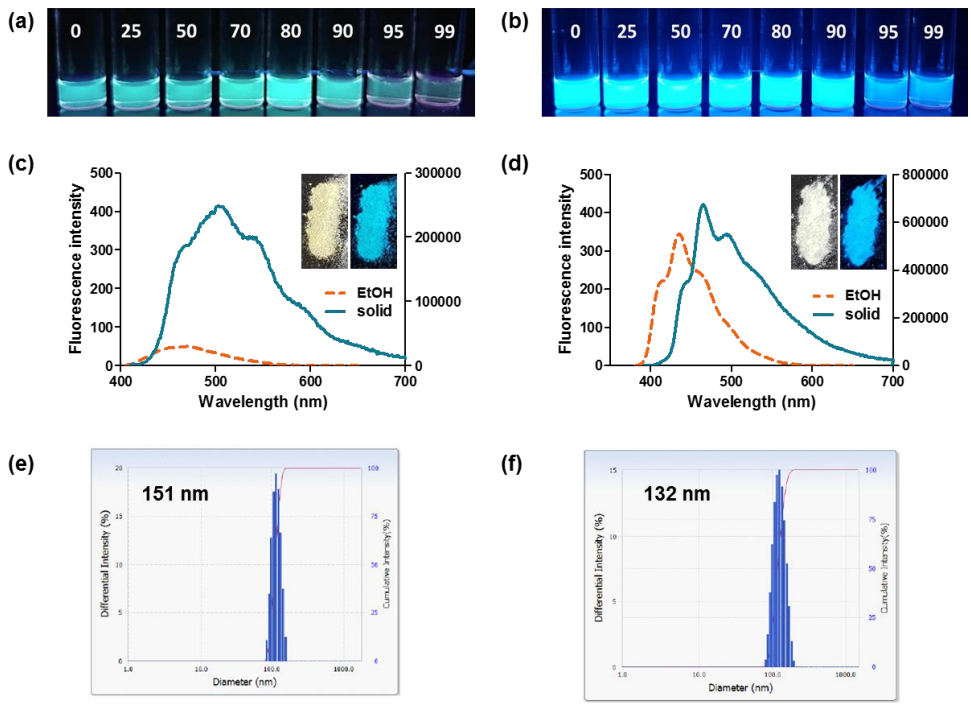

Figure 3. Photographs of 10 μM **IQ44 (a)** and **IQ-B27 (b)** in a water/THF mixture (0-99 %) under UV light (312 nm). Fluorescence spectra of **IQ44 (c)** and **IQ-B27 (d)** in ethanol (2 μM, dashed line) and solid states (solid line); excited at 388 nm **(c)**, 372 nm **(d)**; inset: photographs of **IQ44 (c)** and **IQ-B27 (d)** in the solid state under UV light (365 nm). Particle size distribution of 10 μM **IQ44 (e)** and **IQ-B27** (10 μM) **(f)** in a DMSO/water mixture (1/9: v/v).

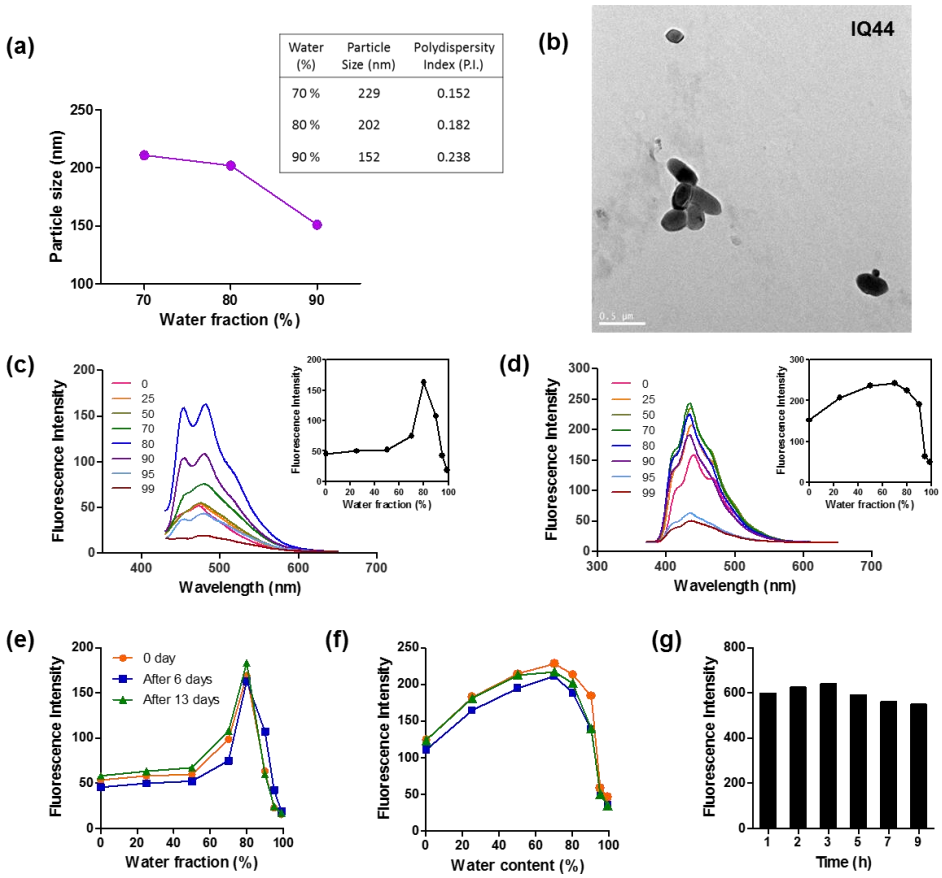

Figure 4. AIE properties of **IQ44** and **IQ-B27**. **(a)** Particle size distributions of **IQ44** (10 μM) at varied fractions of water. **(b)** TEM images of **IQ44** (10 μM) in a DMSO/water mixture (1/9: v/v). Fluorescence spectra of 10 μM **IQ44 (c)** and **IQ-B27 (d)** in THF/water mixture (0-99%) with excitation at 417 nm **(c)** and at 354 nm **(d)**; inset: plots of fluorescence intensity of **IQ44** at 482 nm **(c)** and **IQ-B27** at 435 nm **(d)**. Fluorescent stability of **IQ44** and **IQ-B27 (e-g)**. Plot of fluorescence intensity 10 μM **IQ44 (e)** and **IQ-B27 (g)** in THF/water mixture (0-99%) stored room temperature for 6 days (blue line) and 13 days (green line); emission at 482 and 435 nm for **IQ44** and **IQ-B27**, respectively. Fluorescence intensity of **IQ44** (2 μM) over time after addition of Fe^{3+} (20 equiv) in ethanol; λ_{ex} = 417 nm, λ_{em} = 455 nm.

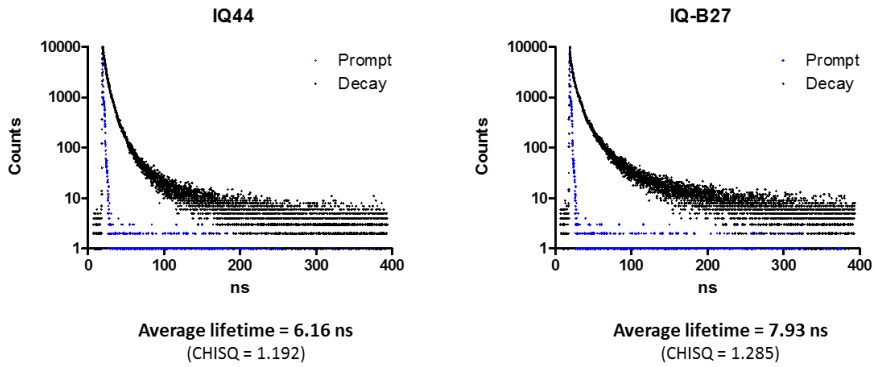

Figure 5. Fluorescence decay profiles of **IQ44** and **IQ-B27** in their solid states.

Table 2. Quantum yields and fluorescence decays of **IQ44** and **IQ-B27**.

Compound	Φ_F (%)		τ (ns) [b]
	EtOH [a]	Solid	Solid
IQ44	3.0	4.5	6.2
IQ-B27	40	20	8.0

[a] Quantum yields in ethanol determined using coumarin 153 as the standard (Φ = 0.53 in ethanol). [b] Mean fluorescence lifetime fitted with a triple exponential function.

3.2.5 Structure-property relationships of IQ metal sensors

Intrigued by the dramatic differences between **IQ18** and **IQ44** as Fe^{3+} sensors, we explored the critical elements of turn-on sensing of **IQ44** by comparing the fluorescence responses of IQ derivatives (Scheme 1) upon binding various cations (Figure 6). Based on the structure-property relationships of the synthesized compounds, the presence of a carboxylic ester at the B ring was critical for turn-on fluorescence. In **IQ42**, which lacks this COOR, the turn-off emission property dominated, as we observed with **IQ18** in ethanol. Turn-on selectivity for Fe^{3+} or Cr^{3+} was retained but to a lesser extent by replacing S with O, as shown in **IQ-B28**. In both ethanol and water, metal selectivity was significantly compromised in the absence of thiophene, as shown in **IQ-B27**, suggesting that thiophene is a critical element for tuning the Fe^{3+} selectivity.

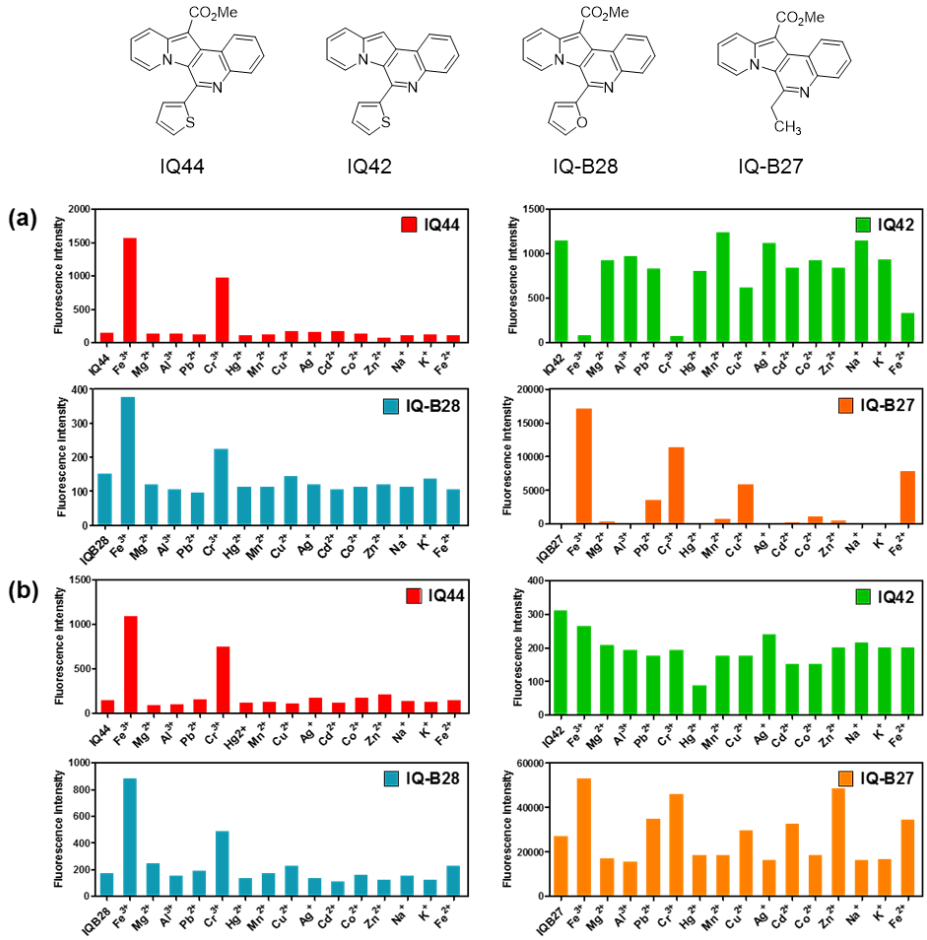

Figure 6. Fluorescence response of **IQ44** (red)**, IQ42** (green)**, IQ-B28** (blue), and **IQ-B27** (orange) in the presence of Fe^{3+} or other metal ions (400 μM) in ethanol **(a)** and in water **(b)** after incubation for 30 sec. Samples containing 4 μM IQ compounds were excited at 420 nm, and emission was measured at 458 nm, 480 nm, 510 nm and 458 nm, for **IQ44**, **IQ42**, **IQ-B28**, and **IQ-B27**, respectively

3.2.4 Bioimaging of IQ44 as a probe for Fe^{3+} in live cells

The fact that the thiophene group conferred the selectivity of **IQ44** prompted us to investigate the turn-on sensing abilities of **IQ44** for Fe^{3+} in live cell imaging using fluorescence confocal microscopy. The cytotoxicity of **IQ44** at 10 μM was negligible (Figure 7) even with blue light exposure (800 lm/m^2) for 5 min, suggesting that it could be used as a biosensor. Figure 8 depicts the fluorescence response of **IQ44** in iron-overloaded HepG2 cells. Fluorescence increase was observed when Fe^{3+} was applied with **IQ44**. Due to the low solubility of ferric chloride, we treated cells with ammonium ferric citrate followed by washing with PBS buffer containing 100 μM EDTA to remove extracellular ferric iron precipitates. This treatment resulted in an increase in fluorescence in the presence of Fe^{3+} (Figure 8a-b). The quantification of cell images based on the statistical analysis of the fluorescence intensities of individual cell images is demonstrated in Figure 9. To identify the cellular location of **IQ44**, Lysotracker and Mitotracker were used for co-localization experiments (Figure 10). When treated with Fe^{3+}, **IQ44** showed an increased Pearson coefficient and an overlap coefficient with Lysotracker (0.748 and 0.784, respectively) but not with Mitotracker (0.434 and 0.618, respectively), revealing the specific location of **IQ44** in the lysosomes of live cells due to activation of its fluorescence in the presence of Fe^{3+} (Figure 10). Lysosomes, the major digestive compartments of cells, contain relatively high contents of labile iron derived from the degradation of endocytosed and autophagocytosed iron-containing proteins.[7, 10, 13, 29]

Autophagy is linked with the endocytosis pathway, with most late endosomes or lysosomes fusing with autophagosomes.[11] Figure 8c shows that the increased fluorescent puncta of **IQ44** in the presence of Fe^{3+} colocalized well with the

fluorescent protein-tagged LC3 proteins (pmRFP-LC3), indicating that autophagy was induced and **IQ44** enabled autolysosome detection. The LC3 puncta are evenly spread in both cells treated with IQ44 only (Figure 8c, top) and **IQ44** with ammonium ferric citrate (Figure 8c, bottom), whereas the colocalization of **IQ44** and LC3 puncta is higher in **IQ44** with ammonium ferric citrate than in **IQ44** only. Our data indicate significant amounts of Fe^{3+} in lysosomes in iron-overloaded HepG2 cells, although the exact pathway of ferric ion uptake and trafficking within the cell remain to be determined. Iron overload and iron toxicity are linked to cancers and neuron degeneration, and probes for iron trafficking are of tremendous importance to understand these links.

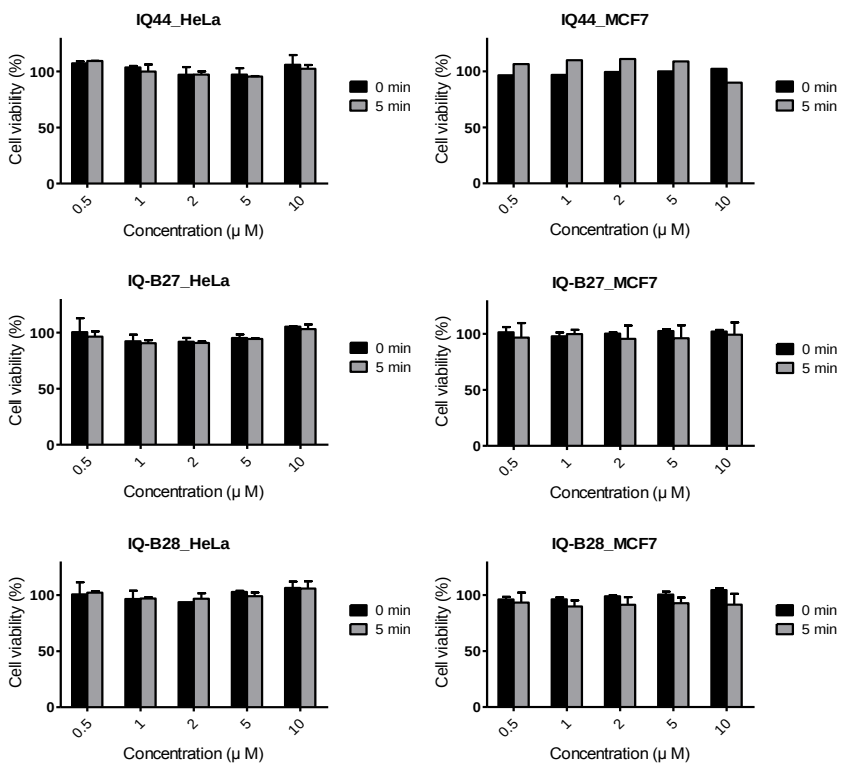

Figure 7. Cytotoxicity of **IQ44**, **IQ-B27** and **IQ-B28** in HeLa and MCF7 cells with blue light exposure for 5 min.

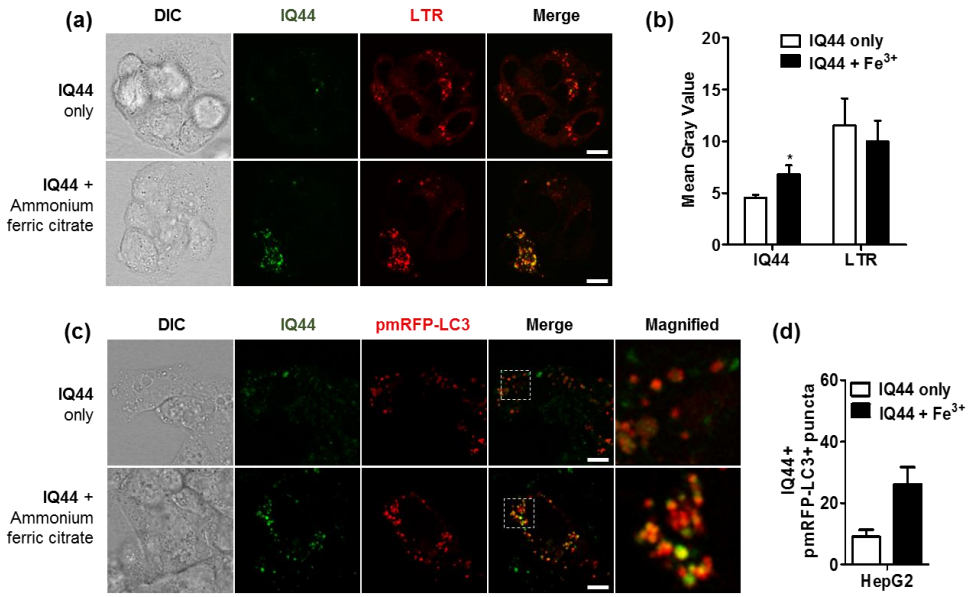

Figure 8. Live confocal images of **IQ44** in HepG2 cells. **(a-b)** The colocalization of **IQ44** and LysoTracker Red in the presence of ammonium ferric citrate. Cells were pretreated with and without 100 μM ammonium ferric citrate for 18 h, incubated with 10 μM **IQ44** for 1 h, and then treated with 75 nM LysoTracker Red for 30 min. **(c-d)** The colocalization of **IQ44** and LC3 puncta in the presence of ammonium ferric citrate. HepG2 cells transfected with pmRFP-LC3 were incubated with 100 μM of ammonium ferric citrate in serum-free medium for 18 h. Then, 10 μM of **IQ44** was added to the pmRFP-LC3-transfected cells, either untreated or treated with ammonium ferric citrate. The green channel (Ex: 488 nm, Em: 493–560 nm) arose from **IQ44** fluorescence, and the red channel (Ex: 561 nm, Em: >566 nm) from LysoTracker Red fluorescence or LC3 (Ex: 561 nm, Em: 566-630 nm). The scale bar represents 10 μm. *$P < 0.05$, as determined by Student's *t*-test.

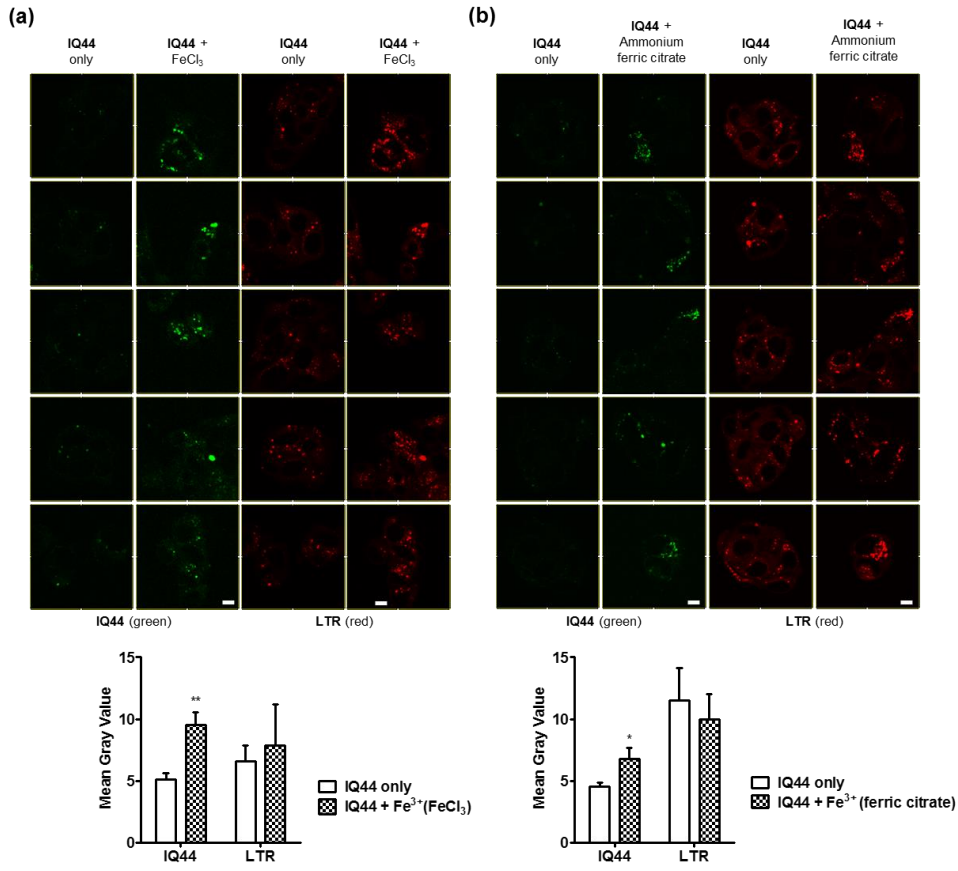

Figure 9. Quantification of cell images in the absence or presence of ferric chloride **(a)** or ammonium ferric citrate **(b)** with the statistical analysis of the fluorescence intensities of individual cell images. The green channel (Ex: 488 nm, Em: 493–560 nm) arose from **IQ44** fluorescence, and the red channel (Ex: 561 nm, Em: >566 nm) from LysoTracker Red fluorescence. *P < 0.05 and **P < 0.005, as determined by Student's *t*-test.

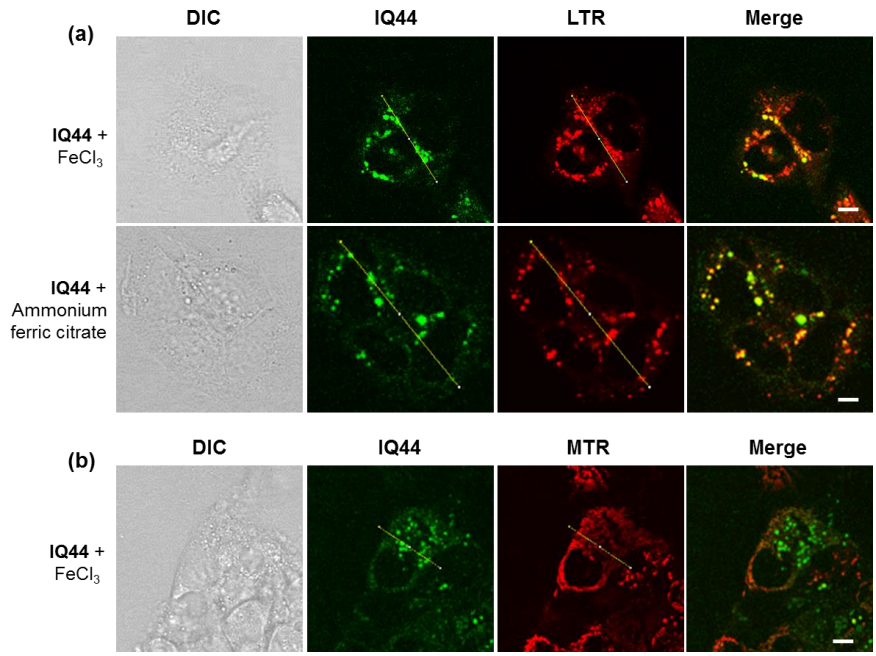

Figure 10. Intracellular localization of **IQ44** in HepG2 cells. HepG2 cells were pretreated with 100 μM ferric chloride (**a**, top) or ammonium ferric citrate (**a**, down) for 18 h, incubated with 10 μM **IQ44** for 1 h, and followed by treatment with 75 nM LysoTracker Red for 30 min (**a**) or with 150 nM MitoTracker Red for 20 min **(b)**. The green channel (Ex: 488 nm, Em: 493–560 nm) arose from **IQ44** fluorescence, and the red channel (Ex: 561 nm, Em: >566 nm) from LysoTracker Red fluorescence or MitoTracker Red fluorescence. The scale bar represents 10 μm. Intensity profile of the region of interest (ROI) is presented with a yellow line across the HepG2 cells.

3.2.5 pH effects on the fluorescence of IQ44 in lysosomes

Since the fluorescence change in **IQ44** observed in the confocal imaging data could result from complicated cellular environments (for example, pH, polarity), other factors affecting the emission of **IQ44** in lysosomes need to be examined. In contrast to the previous IQ derivatives with significant solvatochromic effects,[8] **IQ44** was less sensitive to polarity (Figure 11a), thereby eliminating the potential for fluorescence change caused by the polarity change in lysosomes. One might argue that the protons generated by titrating trivalent cations (Fe^{3+}, Cr^{3+}, and Al^{3+}) would lead to the protonation of the quinoline group of IQs, thereby inducing pH-dependent turn-on fluorescence. To examine whether the observed fluorescence increases in **IQ44** in live cell imaging were caused by the acidic environment of the lysosome (pH 4-6), titration experiments using **IQ44** with Fe^{3+} were performed in a buffered solution at pH 4.5. A fluorescence increase was still observed for **IQ44** upon the addition of ferric iron, whereas no significant fluorescence change was observed for **IQ-B27** (Figures 11b-c), supporting our structure-property relationship data in that selective turn-on sensing was only observed in **IQ44**, and not in **IQ-B27** (Figure 6). We also measured the fluorescence responses of **IQ44** upon the addition of an excess amount of acids, which resulted in no change until the addition of 50 equiv. of TFA or HCl in ethanol (Figures 11d-e). Even after the addition of 100 equiv. of these acids, a further fluorescence increase in **IQ44** was observed by the subsequent addition of Fe^{3+}, supporting the contribution from the Fe^{3+} complex formation besides the protonation. Increases in fluorescence upon the addition of acids and Fe^{3+} are compared in Figures 11e-f. The exact turn-on sensing element for Fe^{3+} in lysosomes and the presence of labile ferric ions in the lysosome, particularly in iron-overloaded

cells, remain controversial. The possibility that the fluorescence increase in lysosomes was caused by the protonation of **IQ44** cannot be completely eliminated, but the affinity of **IQ44** for ferric ion is higher than for protons in our data, at least in ethanol.

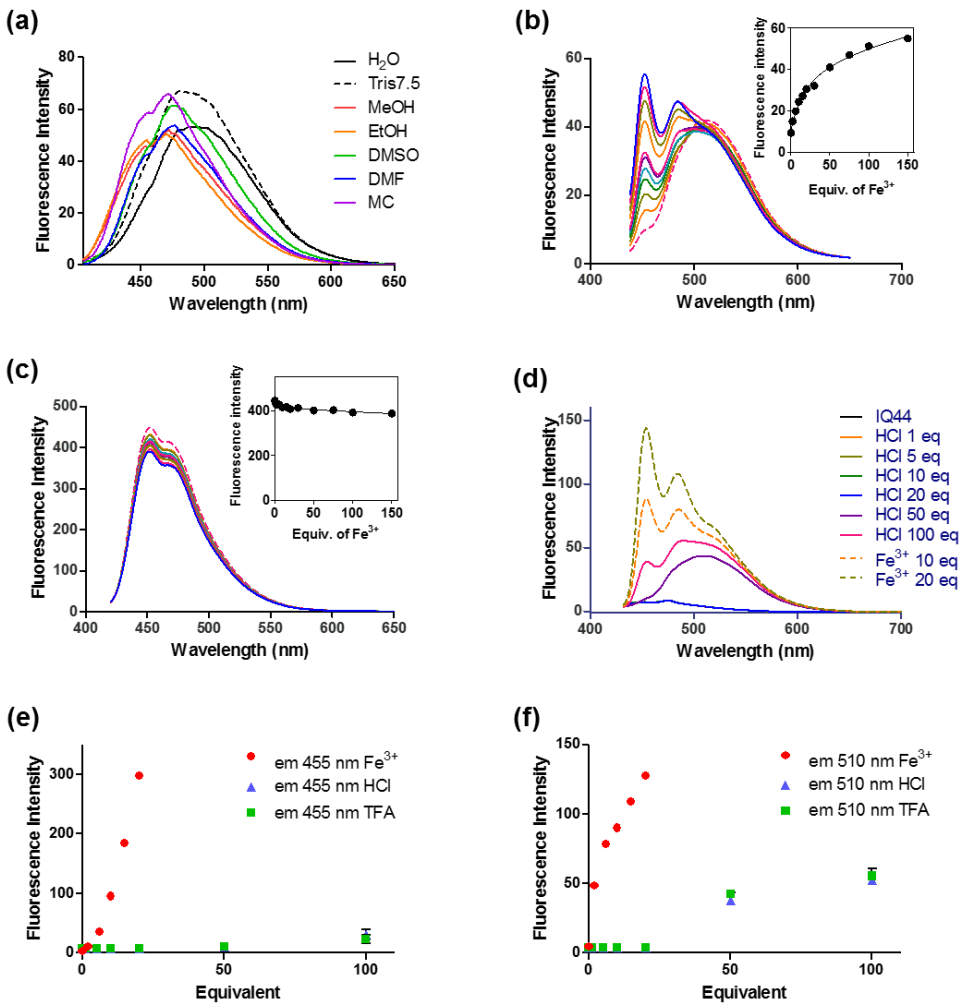

Figure 11. (a) Emission spectra of **IQ44** in various solvents. **(b)** Fluorescence responses of **IQ44** (2 μM) excited at 428 nm upon the addition of various amounts of Fe^{3+} (0-150 equiv.) in a buffered solution at pH 4.5. **(c)** Fluorescence responses of **IQ-B27** (2 μM) excited at 410 nm upon the addition of various amounts of Fe^{3+} (0-150 equiv.) in a buffered solution at pH 4.5. **(d)** Fluorescence changes in **IQ44** (2

μM) upon the addition of HCl (0-100 equiv.) in ethanol. **(e-f)** Comparison of fluorescence increases in **IQ44** (2 μM) induced by Fe^{3+}, HCl, and TFA in ethanol.

3.2.6 X-ray crystallographic analysis

To understand the influence of intermolecular interactions on the solid-state emission of **IQ44** and **IQ-B27**, their geometry and packing arrangements were analysed in crystal states (Figure 12). The single crystal of **IQ44** is depicted as a tilted dimer, with each monomer stacked in a head-to-head arrangement. The intermolecular distances between indolizino-quinoline rings were not parallel (3.958 Å and 3.042 Å), which deviated from conventional π-π stacking interactions that usually reduce fluorescence. Intermolecular CH-π and intramolecular CH-π interactions between the thiophene ring and CH are shown in Figure 12b. Nonclassical hydrogen bonds between 1) C=O(O1) and H9, and 2) H17 and N1 compose the intermolecular networks, rigidifying the molecular conformation of **IQ44**. The X-ray structure of the **IQ44**-Fe^{3+} complex could not be obtained at sufficient quality. Nevertheless, a single cell unit of **IQ44** with Fe^{3+} showed significant intermolecular interactions between **IQ44** and Fe^{3+}, demonstrating the short distance between S-Fe-carbonyl O. In addition, the torsion angle of N-C-C-S in **IQ44** in the presence of Fe^{3+} was larger compared with that of the free form (81.9/98.1 vs 70.0/72.5 degrees, Figure 12 and 13), indicating that the thiophene is not conjugated with the ABCD ring in the presence of Fe^{3+} and that the observed blue shift in emission was caused by minimal electronic communication with the ABCD ring of IQ. ^{1}H NOESY NMR spectra of the **IQ44**-Fe^{3+} complex in CD_3OD were found to be in the protonated form due to the hydrolysis of the **IQ44**-Fe^{3+}

complex. Nevertheless, the c-i NOE peak correlation between the indolizine proton and thiophene proton of **IQ44** in the **IQ44**-Fe^{3+} complex decreased, indicating an increase in the torsion angle of the thiophene in this complex. (Figure 14).

Meanwhile, **IQ-B27** exhibited a clustered structure composed of alternating layers with opposite directions (i.e., anti-parallel alignment), which also avoids conventional π-π–stacking interactions (Figure 12e-f). Intramolecular as well as intermolecular hydrogen bonds along with van der Waals interactions between methyl groups compose a tight network that blocks the non-radiative pathway in the solid state of **IQ-B27**. The presence of the carboxylic ester group at the B ring appears to adjust the dipole–dipole direction, which further controls the self-assembled architecture of **IQ44** and **IQ-B27**.

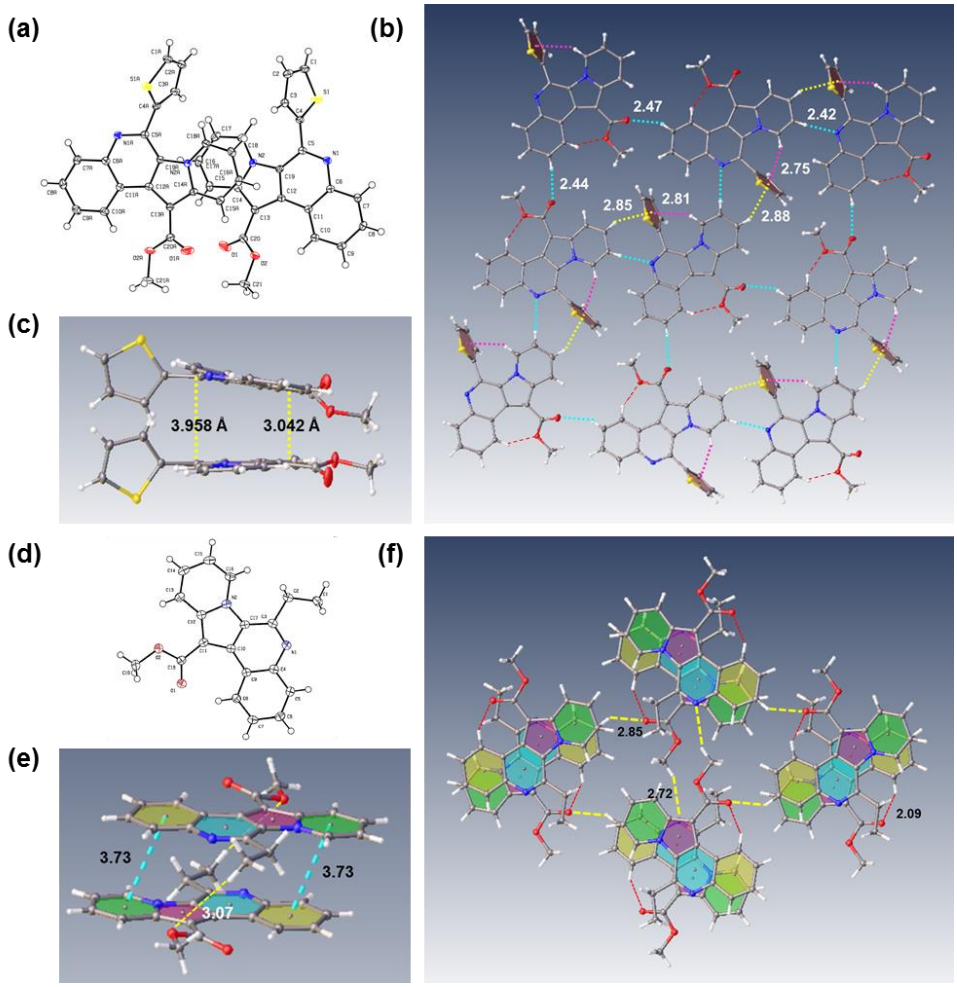

Figure 12. (a) Crystal structure of **IQ44. (b)** Packing structures including inter- and intramolecular interactions; pink: intramolecular CH-π interaction, yellow: intermolecular CH-π interaction, cyan: intermolecular hydrogen bonding, red: intramolecular hydrogen bonding. **(c)** The distance of the tilted dimer of **IQ44** in crystal structure. **(d)** Crystal structure of **IQ-B27** in ORTEP diagram at 50 % probability. **(e)** Anti-parallel alignment with opposite directions from a side view. **(f)** Cluster packing structure including inter- and intramolecular interaction from a top view; yellow: intermolecular nonclassic hydrogen bonding, red: intramolecular hydrogen bonding.

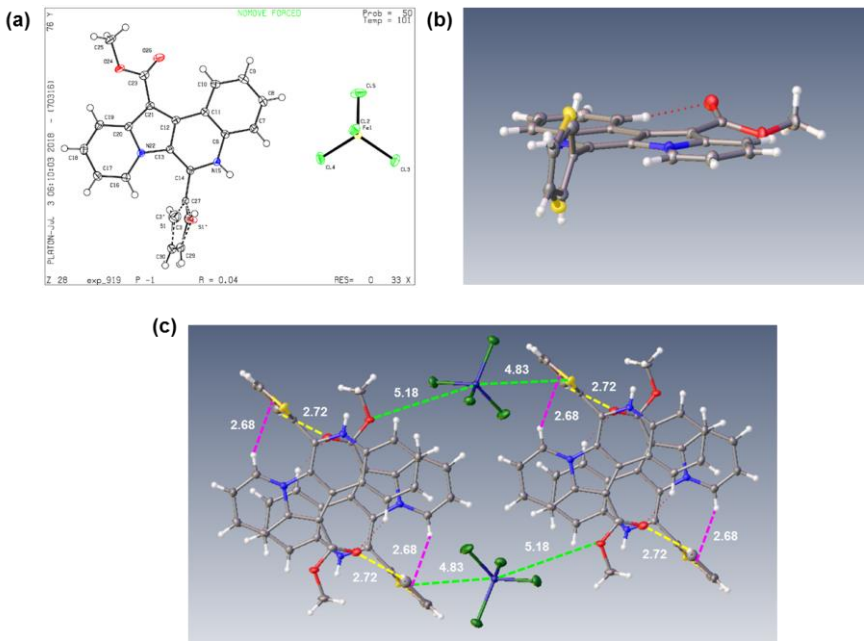

Figure 13. Crystal structure of **IQ44** with Fe^{3+}. **(a)** ORTEP diagram at 50 % probability. The thiophene ring is disordered with two different orientations. **(b)** Side view of **IQ44**, displaying the increased torsion angle in the presence of Fe^{3+}. **(c)** Packing structure including interaction with Fe^{3+} in top view.

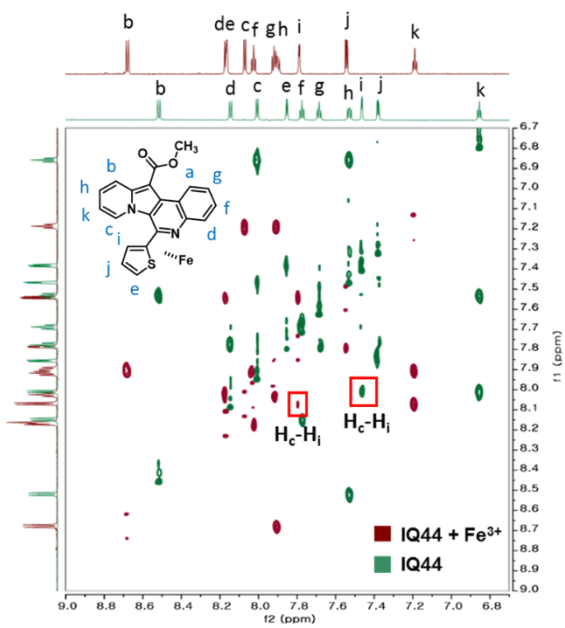

Figure 14. ^{1}H NOESY NMR (800 MHz, CD_3OD) spectra of **IQ44** (green) and **IQ44**-Fe^{3+} (red). The resonance (H_c-H_i) that decreased in presence of Fe^{3+} is highlighted with a red box. The **IQ44**-Fe^{3+} complex was an orange powder synthesized from the reaction between **IQ44** and $FeCl_3$ in ethanol.

3.3 Conclusion

We developed novel IQ-based fluorescent Fe^{3+} sensors, **IQ44**, which selectively differentiate Fe^{3+} from Fe^{2+} and other metal ions. **IQ44** exhibited fluorescence enhancement in response to Fe^{3+}. Interestingly, **IQ44** worked as a ~150 nm turn-on nanoparticle sensor for Fe^{3+} in water. The working mechanism of the turn-on sensing by **IQ44** in water is explained by the combined effect of aggregation-induced emission (AIE) characteristics of IQ in addition to the metal-induced restriction of rotation of the thiophenyl group, through which this molecule resembles the highly emissive state of **IQ-B27**. Live cell confocal microscopy images of Fe^{3+}-overloaded HepG2 cells demonstrated that **IQ44** specifically localized to the lysosomes. In addition, **IQ44** fluorescent puncta colocalized well with pmRFP-LC3 transfected autophagosomes, enabling the detection of autophagosome-lysosome fusion during the autophagy process. Structure-property relationship analysis revealed that the thiophene/furan ring confers selectivity for Fe^{3+}. Restriction of rotation of thiophene by Fe^{3+} serves as a critical tuning handle, leading to selective Fe^{3+} sensing. Further investigations are underway to precisely control the morphology of these emissive aggregates.

IV. EXPERIMENTAL

4.1 Experiments described in chapter I

4.1.1 General information

Unless otherwise noted, all reagents and starting materials were purchased from commercial suppliers (ACS grade or higher quality) and were used without further purification. Reactions were monitored by thin layer chromatography carried out on silica gel 60 F254 plate (Merck, Darmstadt, Germany) using UV illumination at 254 nm (VL-4.LC, Vilber Lourmat, Eberhardzell, Germany). Column chromatography was performed on silica gel (230~400 mesh; Zeochem, Lake Zurich, Switzerland) using a mixture of n-hexane, EtOAc and CH_2Cl_2 as eluents. 1H- (300, 500, 600, or 800 MHz) and 13C-NMR (75, 125, 150, or 200 MHz) spectra were recorded on a GEMINI 2000 (VARIAN, Palo Alto, CA, USA) or FT-NMR Avance III HD (Bruker, Billerica, MA, USA) at ambient temperature. The chemical shifts are reported in δ unit, parts per million (ppm) relative to $CHCl_3$ (7.26 ppm), DMSO (2.49 ppm), or MeOH (3.30 ppm) in the deuterated solvent and coupling constants (J) are expressed in hertz (Hz). All ESI-MS were recorded with a 6130 Single Quadrupole LC/MS (Agilent Technologies, Santa Clara, CA, USA) and high-resolution mass spectra (HR-MS) were acquired under fast atom bombardments (FAB) condition on a JMS-700 MStation (JEOL, Tokyo, Japan). UV-Vis analysis was performed on a Lambda 25 (Perkin Elmer, Waltham, MA, USA) and high-performance liquid chromatography (HPLC) chromatogram were obtained using a YL9100 reversed-phase HPLC (Younglin, Anyang, South Korea). IR spectra were recorded on a FT/IR-4200 spectrometer (Jasco, Easton, MD, USA).

4.1.2 General synthetic procedure for 6a and 6c-6n

To a stirred solution of α-bromophenylacetic acid **9** (1.0 mmol) and *N*-ethyl-*N′*-(3-dimethylaminopropyl)carbodiimide hydrochloride (EDC·HCl, 1.5 mmol) in 10 mL of CH_2Cl_2, compound **7** (1.0 mmol) was added. The reaction mixture was allowed to stir at room temperature until complete conversion was observed by TLC. The reaction mixture was washed with brine (10 mL) and the organic layers were dried over anhydrous sodium sulfate and concentrated to give the crude product, which was further purified by flash chromatography on silica gel (EtOAc/*n*-hexane = 1:2) to afford the compound **6**.

***N′*-(2-bromo-2-(4-phenoxyphenyl)acetyl)-4-chloro-*N′*-(2-cyanoethyl)benzohydrazide (6a).** 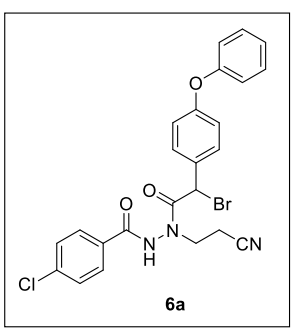

6a

2-bromo -2-(4-phenoxyphenyl)acetic acid (**9a**, 307 mg, 1.00 mmol) was reacted for 1 h according to the general procedure described above to yield **6a** (309 mg, 60%) as a bright yellow oil. ^{1}H-NMR (300 MHz, $CDCl_3$): δ 8.28 (bs, 1H, -CONH), 7.77*/ 7.71 (2 × d, J = 8.7 / 8.4 Hz, 2H), 7.50 (dd, J_1 = 8.1 Hz, J_2 = 6.0 Hz, 2H), 7.41-7.30 (m, 4H), 7.15 (t, J = 7.5 Hz, 1H), 7.01 (dd, J_1 = 7.5 Hz, J_2 = 122 Hz, 2H), 6.97-6.92 (m, 2H), 5.58 (s, 1H), 3.99 (bs, 2H), 2.80 (bs, 2H); ^{13}C-NMR (75 MHz, $CDCl_3$): 169.7, 164.8, 164.7*, 158.4, 156.1, 139.8, 130.5, 129.9 (2C), 128.8 (2C), 129.4 (2C), 128.9 (2C), 128.1 (2C), 124.1, 119.7, 118.5 (2C), 118.4, 46.1, 43.4, 16.3 *represents the isomer

***N′*-(2-([1,1'-biphenyl]-4-yl)-2-bromoacetyl)-4-chloro-*N′*-(2-cyanoethyl)benzoh-**

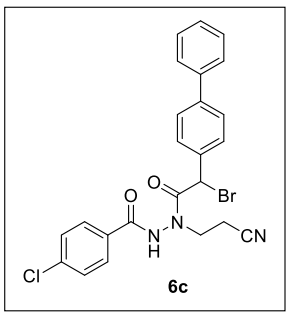

6c

ydrazide (6c). 2-([1,1'-biphenyl]-4-yl)-2-bromoacetic acid (**9c**, 495 mg, 1.70 mmol) was reacted for 2 h according to the general procedure to yield **6c** (383 mg, 45%) as a bright yellow oil. ^{1}H-NMR (600 MHz, $CDCl_3$): δ 7.75*/ 7.70 (bs / d, *J* = 7.3 Hz, 2H), 7.56-7.53 (m, 4H), 7.49-7.40 (m, 6H), 7.36 (t, *J* = 7.3 Hz, 1H), 5.66 (s, 1H), 3.96 (bs, 2H), 2.76 (bs, 2H); ^{13}C-NMR (150 MHz, $CDCl_3$): 169.7, 164.7, 142.3, 142.2*, 139.9*, 139.8, 129.5, 129.4 (4C), 128.9, 128,89 (2C), 128.87 (2C), 128.8*, 128.5, 127.8, 127.6*, 127.1 (4C), 118.4, 46.25, 46.24, 16.3, 16.2*; HR-MS (FAB+): *m/z* calcd for $C_{24}H_{20}BrClN_3O_2$ $[M+H]^+$: 496.0427, found: 496.0421 *represents the isomer

***N′*-(2-bromo-2-phenylacetyl)-4-chloro-*N′*-(2-cyanoethyl)benzohydrazide (6d).**

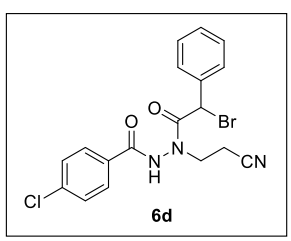

6d

2-bromo-2-phenyl acetic acid (**9d**, 713 mg, 3.32 mmol) was reacted for 2 h according to the general procedure to yield **6d** (710 mg, 51%) as a bright yellow oil. ^{1}H-NMR (500 MHz, $CDCl_3$): δ 9.01 (bs, 1H, -CONH), 7.70*/ 7.66 (2 × d, *J* = 6.5 / 8.0 Hz, 2H), 7.43 (t, *J* = 8.0 Hz, 2H), 7.37-7.36 (m, 1H), 7.31-7.29 (m, 4H), 5.67 (s, 1H), 3.95 (bs, 2H), 2.87 (bs, 2H); ^{13}C-NMR (125 MHz, $CDCl_3$): 169.9, 164.9, 164.8*, 139.7, 129.4 (2C), 129.3 (2C), 129.0 (2C), 128.9 (2C), 128.8, 128.7, 128.0, 118.5, 118.4*, 46.08, 46.07, 16.3, 16.2*; HR-MS (FAB+): *m/z* calcd for $C_{18}H_{16}BrClN_3O_2$ $[M+H]^+$: 420.0114, found: 420.0111 *represents the isomer

4-(1-bromo-2-(2-(4-chlorobenzoyl)-1-(2-cyanoethyl)hydrazinyl)-2-oxoethyl)phenyl acetate (6e). 2-(4-acetoxyphenyl)-2-bromoacetic acid (**9e**, 732 mg, 2.68 mmol) was reacted for 2 h according to the general procedure to yield **6e** (744 mg, 58%) as a bright yellow oil. ^{1}H-NMR (600 MHz, $CDCl_3$): δ 8.61 (bs, 1H, -CONH), 7.72*/ 7.67 (bs / d, *J* = 7.4 Hz, 2H), 7.45 (d, *J* = 8.7 Hz, 2H), 7.35 (d, *J* = 8.7 Hz, 2H), 7.05 (d, *J* = 8.7 Hz, 2H), 5.56 (s, 1H), 3.94 (bs, 2H), 2.74 (bs, 2H), 2.28 (s, 3H); ^{13}C-NMR (150 MHz, $CDCl_3$): 169.5 (2C), 164.9, 151.3, 139.9, 129.6, 129.5 (4C), 129.02, 129.0 (4C), 118.5, 46.5 (2C), 21.2, 16.4, 16.3*; HR-MS (FAB+): *m/z* calcd for $C_{20}H_{18}BrClN_3O_4$ $[M+H]^+$: 478.0169, found: 478.0169 *represents the isomer

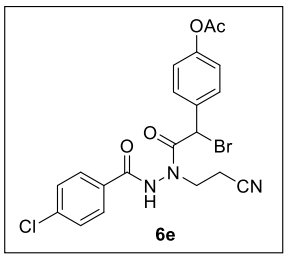

***N'*-(2-(4-benzoylphenyl)-2-bromoacetyl)-4-chloro-*N'*-(2-cyanoethyl)benzohydrazide (6f).** 2-(4-benzoylphenyl)-2-bromoacetic acid (**9f**, 500 mg, 1.57 mmol) was reacted for 2 h according to the general procedure to yield **6f** (353 mg, 43%) as a bright yellow oil. ^{1}H-NMR (800 MHz, $CDCl_3$): δ 9.41 (bs, 1H, -CONH), 7.77 (bs, 2H), 7.69 (d, *J* = 7.7 Hz, 2H), 7.67 (d, *J* = 8.2 Hz, 2H), 7.58 (t, *J* = 7.4 Hz, 1H), 7.46-7.42 (m, 6H), 5.72 (s, 1H), 4.20 (bs, 1H), 3.66 (bs, 1H), 2.82 (bs, 2H); ^{13}C-NMR (200 MHz, $CDCl_3$): δ 196.4, 169.4, 165.08*, 165.03, 139.8, 138.1, 138.0, 136.8, 133.0, 130.4, 130.1 (2C), 129.4 (4C), 129.0 (4C), 128.4 (2C), 118.3, 45.9, 45,8, 16.3, 16.2*; HR-MS (FAB+): *m/z* calcd for $C_{25}H_{20}BrClN_3O_3$ $[M+H]^+$: 524.0377, found: 524.0378 *represents the isomer

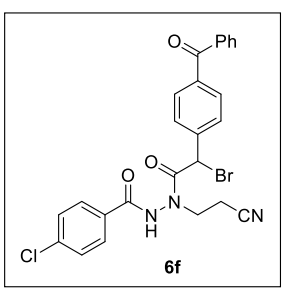

***N'*-(2-(4-acetylphenyl)-2-bromoacetyl)-4-chloro-*N'*-(2-cyanoethyl)benzohydrazide (6g).** 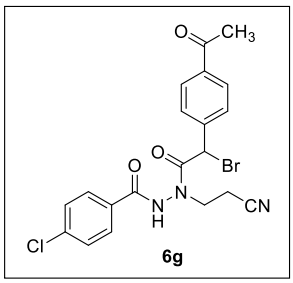

6g

2-(4-acetylphenyl)-2-bromoacetic acid (**9g**, 800 mg, 3.12 mmol) was reacted for 2 h according to the general procedure to yield **6g** (515 mg, 36%) as a colorless oil. ^{1}H-NMR (300 MHz, CD_3OD): δ 8.00-7.89 (m, 2H), 7.81 (d, J = 8.8 Hz, 2H), 7.56-7.53 (m, 4H), 5.97 (s, 1H), 4.14 (bs, 1H), 3.74 (bs, 1H), 2.79 (bs, 2H), 2.58 (s, 3H); ^{13}C-NMR (75 MHz, CD_3OD): δ 200.5, 172.1, 171.8, 140.9, 132.0, 131.6 (4C), 130.7 (4C), 130.6 (2C), 120.0, 41.2 (2C), 27.1, 17.5; HR-MS (FAB+): *m/z* calcd for $C_{20}H_{18}BrClN_3O_3$ $[M+H]^+$: 462.0220, found: 462.0209 *represents the isomer

***N'*-(2-bromo-2-(4-(trifluoromethyl)phenyl)acetyl)-4-chloro-*N'*-(2-cyanoethyl) benzohydrazide (6h).** 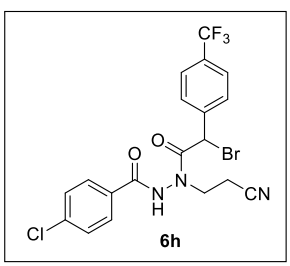

6h

2-bromo-2-(4-(trifluoromethyl) phenyl)acetic acid (**9h**, 800 mg, 2.83 mmol) was reacted for 2 h according to the general procedure to yield **6h** (807 mg, 59%) as a bright yellow oil. ^{1}H-NMR (800 MHz, $CDCl_3$): δ 9.13 (bs, 1H, -CONH), 7.73-7.70 (bd, 2H), 7.55-7.54 (m, 2H), 7.52-7.51 (m, 2H), 7.47-7.44 (m, 2H), 5.65 /5.62* (s / bs, 1H). 4.26 (bs, 1H), 3.58 (bs, 1H), 2.87-2.70 (bm, 2H); ^{13}C-NMR (200 MHz, $CDCl_3$): δ 169.6, 165.0*, 164.9, 140.0, 139.9, 131.3 (dq, J_1 = 63.4 Hz, J_2 = 130.2 Hz), 129.5 (2C), 129.4 (2C), 128.93 (2C), 128.88 (2C), 128.5, 123.6 (q, J = 270.7 Hz). 118.55, 118.54*, 46.0, 45.9, 16.3, 16.2*; HR-MS (FAB+): *m/z* calcd for $C_{19}H_{15}BrClF_3N_3O_2$ $[M+H]^+$: 487.9988, found: 487.9996 *represents the isomer

***N′*-(2-bromo-2-(4-nitrophenyl)acetyl)-4-chloro-*N′*-(2-cyanoethyl)benzohydrazide (6i).** 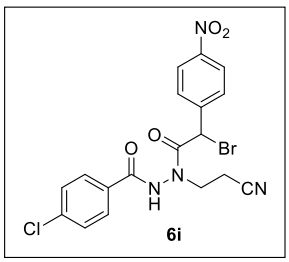

6i

2-bromo-2-(4-nitrophenyl)acetic acid (**9i**, 516 mg, 2.31 mmol) was reacted for 2 h according to the general procedure to yield **6i** (619 mg, 58%) as a colorless oil. ^{1}H-NMR (300 MHz, CD_3OD): δ 8.30-8.13 (bd, 2H), 7.86-7.79 (m, 2H), 7.74-7.64 (bm, 2H), 7.57-7.53 (m, 2H), 6.03 (s, 1H), 4.13 (bs, 1H), 3.78 (bs, 1H), 2.78 (t, *J* = 6.4 Hz, 2H); ^{13}C-NMR (75 MHz, CD_3OD): δ 171.5, 168.7, 150.2, 141.0, 132.3, 131.46 (2C), 131.42 (2C), 130.9 (4C), 125.3, 120.0, 47.2, 44.7, 17.47, 17.44*; HR-MS (FAB+): *m/z* calcd for $C_{18}H_{15}BrClN_4O_4$ $[M+H]^+$: 464.9965, found: 464.9952 *represents the isomer

***N′*-(2-bromo-2-(4-nitrophenyl)acetyl)-*N′*-(2-cyanoethyl)-4-methoxybenzohydrazide (6j).** 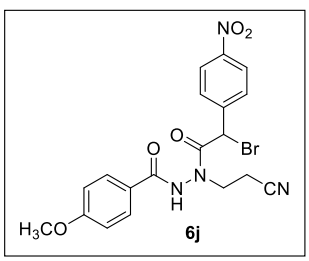

6j

N′-(2-cyanoethyl)-4-methoxybenzo hydrazide (**7j**, 56 mg, 0.26 mmol) and 2-bromo-2-(4-nitrophenyl)acetic acid (**9j**, 66 mg, 0.26 mmol) were reacted for 16 h according to the general procedure to yield **6j** (43 mg, 36%) as a colorless oil. ^{1}H-NMR (800 MHz, $CDCl_3$): δ 8.79 (bs, 1H), 8.16 (d, *J* = 8.6 Hz, 2H), 7.77 (bs, 2H), 7.56 (d, *J* = 7.8 Hz, 2H), 6.97 (d, *J* = 8.2 Hz, 2H), 5.66 (s, 1H), 4.26 (bs, 1H), 3.87 (s, 3H), 3.63 (bs, 1H), 2.86 (bs, 1H), 2.68 (bs, 1H); ^{13}C-NMR (200 MHz, $CDCl_3$): 176.3, 169.4*, 165.5, 163.8, 148.1, 129.5 (2C), 129.2 (2C), 128.7 , 126.5 (2C), 122.2, 118.4, 114.5 (2C), 55.6, 46.4, 28.4, 16.3. *represents the isomer

***N′*-(2-bromo-2-(4-nitrophenyl)acetyl)-*N′*-(2-cyanoethyl)-4-nitrobenzohydrazide (6k).** 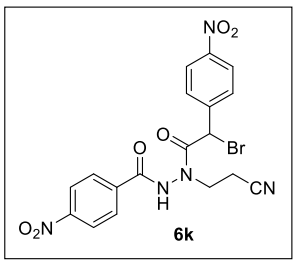

N′-(2-cyanoethyl)-4-nitrobenzohydrazide (**7k**, 80 mg, 0.34 mmol) and 2-bromo-2-(4-nitrophenyl)acetic acid (**9k**, 89 mg, 0.34 mmol) were reacted for 2 h according to the general procedure to yield **6k** (69 mg, 43%) as a bright yellow oil. ^{1}H-NMR (800 MHz, DMSO-d_6): δ 8.33 (d, J = 9.0 Hz, 2H), 8.30 (d, J = 8.8 Hz, 2H), 8.12 (d, J = 9.0 Hz, 2H), 7.79 (d, J = 8.7 Hz, 2H), 6.47 (s, 1H), 4.10-4.03 (m, 2H), 3.01 (td, J = 6.4, 1.7 Hz, 2H); ^{13}C-NMR (200 MHz, DMSO-d_6): 158.8, 148.9, 148.0, 145.9, 141.4, 134.7, 128.8 (2C), 127.7 (2C), 124.0 (2C), 123.9 (2C), 118.8, 75.5, 54.9, 15.9.

***N′*-(2-bromo-2-(4-nitrophenyl)acetyl)-*N′*-(2-cyanoethyl)nicotinohydrazide (6l).** 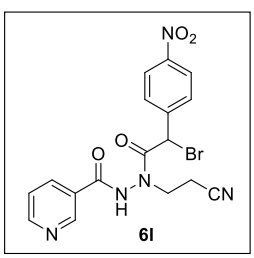

N′-(2-cyanoethyl)nicotinohydrazide (**7l**, 110 mg, 0.58 mmol) and 2-bromo-2-(4-nitrophenyl)acetic acid (**9l**, 150 mg, 0.58 mmol) were reacted for 16 h according to the general procedure to yield **6l** (107 mg, 43%) as a colorless oil. ^{1}H-NMR (800 MHz, CD_3OD): δ 9.02* / 8.99 (bs / bs, 1H), 8.76 (dd, J = 4.8, 1.6 Hz, 1H), 8.28* / 8.25 (d / d, J = 8.2 / 7.9 Hz, 2H), 8.15 (d, J = 5.4 Hz, 1H), 7.72* / 7.65 (bs / bs, 2H), 7.61-7.59 (m, 1H), 6.08 (s, 1H), 4.14 (bs, 1H), 3.80 (bs, 1H), 2.81 (bs, 2H); ^{13}C-NMR (200 MHz, CD_3OD): 171.6, 171.4*, 167.6, 154.6 (2C), 154.5*, 150.3 (2C), 138.5, 138.4, 131.7, 131.3, 126.1 (2C), 125.3, 120.0, 57.0, 46.9, 17.5. *represents the isomer

***N′*-(2-bromo-2-(4-nitrophenyl)acetyl)-*N′*-(2-cyanoethyl)isonicotinohydrazide**

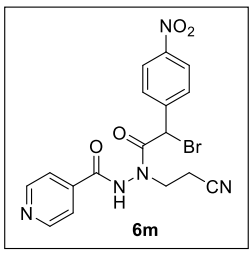

(6m). *N′*-(2-cyanoethyl)isonicotinohydrazide (**7m**, 110 mg, 0.58 mmol) and 2-bromo-2- (4-nitrophenyl)acetic acid (**9m**, 150 mg, 0.58 mmol) were reacted for 16 h according to the general procedure to yield **6m** (128 mg, 51%) as a colorless oil. ^{1}H-NMR (800 MHz, CD_3OD): δ 8.76-8.75 (m, 2H), 8.24* / 8.12 (bs / d, *J* = 8.7 Hz, 2H), 7.83 / 7.70* (d / bs, *J* = 6.0 Hz, 2H), 7.78 (d, *J* = 6.1 Hz, 2H), 7.64* / 7.43 (bs / d, *J* = 8.9 Hz, 2H), 6.07 (s, 1H), 4.14 (bs, 1H), 3.81 (bs, 1H), 2.80 (t, *J* = 6.6 Hz, 2H); ^{13}C-NMR (200 MHz, CD_3OD): 174.9, 171.5*, 167.6, 167.5*, 152.1 (2C), 149.2, 144.3, 141.8, 132.7 (2C), 152.2 (2C), 124.0 (2C), 120.3*, 120.1, 46.2, 40.5, 17.7*, 17.5. *represents the isomer

***N′*-(2-bromo-2-(4-nitrophenyl)acetyl)-*N′*-(2-cyanoethyl)thiazole-2-carbohydra-**

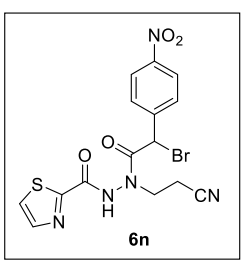

zide (6n). *N′*-(2-cyanoethyl)thiazole-2-carbohydrazide (**7n**, 48 mg, 0.26 mmol) and 2-bromo-2-(4-nitrophenyl)acetic acid (**9n**, 69 mg, 0.26 mmol) were reacted for 2 h according to the general procedure to yield **6n** (69 mg, 33%) as a colorless oil. ^{1}H-NMR (800 MHz, $CDCl_3$): δ 9.35 (bs, 1H), 8.17 (d, *J* = 8.6 Hz, 2H), 7.98 (d, *J* = 2.8 Hz, 1H), 7.76 (d, *J* = 2.9 Hz, 1H), 7.57 (d, *J* = 8.7 Hz, 2H), 5.67 (s, 1H), 4.02 (bs, 1H), 3.94 (bs, 1H), 2.80 (bs, 1H), 2.76 (bs, 1H); ^{13}C-NMR (200 MHz, $CDCl_3$): 168.6, 159.0, 158.2, 148.2, 144.6 (2C), 141.5, 129.3, 126.8 (2C), 123.9, 117.4, 77.2, 46.6, 16.2.

4.1.3 General synthetic procedure for 3a-3j

Potassium carbonate (K_2CO_3, 10.0 equiv.) was added to a stirred solution of compound **6** (1.0 equiv.) dissolved in CH_3CN, and the reaction mixture was stirred for 8 h at room temperature, 50 ºC and 75 ºC, respectively (except **3i**, where the reaction temperature was set to 0 ºC). After cooling to room temperature, the reaction mixture was filtered to remove K_2CO_3 and concentrated under reduced pressure. The residue was purified by flash chromatography on silica gel (EtOAc/*n*-hexane = 1:2) to give **3**.

3-(2-(4-chlorophenyl)-5-oxo-6-(4-phenoxyphenyl)-5,6-dihydro-4*H*-1,3,4-oxadiazin-4-yl)propanenitrile (3a). Compound **6a** (110 mg, 0.21 mmol) was reacted according to the general procedure to yield **3a** (82 mg, 88%) as a white solid. Mp 129.6 – 130.0 ºC; ^{1}H-NMR (500 MHz, $CDCl_3$): δ 7.81 (d, J = 8.6 Hz, 2H), 7.37-7.31 (m, 6H), 7.12 (t, J = 8.6 Hz, 1H), 6.98 (dd, J_1 = 10.3 Hz, J_2 = 8.5 Hz, 4H), 5.79 (s, 1H), 4.13 (t, J = 6.7 Hz, 2H), 2.81 (t, J = 6.7 Hz, 2H); ^{13}C-NMR (125 MHz, $CDCl_3$): δ 159.9, 158.8, 156.0, 148.1, 137.5, 129.8 (2C), 128.8 (2C), 128.6, 128.4 (2C), 128.0 (2C), 127.7, 124.0, 119.6 (2C), 118.6 (2C), 117.2, 76.6, 43.4, 16.4; FT-IR (KBr): 2994, 2357, 1770, 1685, 1636, 1589, 1507, 1489, 1403, 1241, 1170, 1091, 1013, 873, 838, 755, 693 cm^{-1}; HR-MS (FAB+): *m/z* calcd for $C_{24}H_{19}ClN_3O_3$ $[M+H]^+$: 432.1115, found: 432.1119.

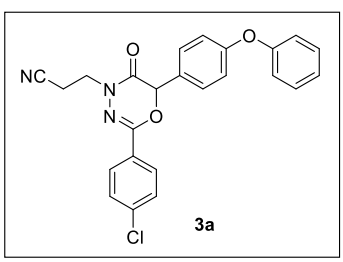

3-(2-(4-chlorophenyl)-5-oxo-6-(4-methoxyphenyl)-5,6-dihydro-4*H*-1,3,4-oxadi-

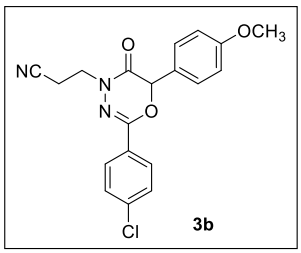

azin-4-yl)propanenitrile (3b). To a stirred solution of 2-bromo-2-(4-methoxyphenyl)acetic acid **9b** (158 mg, 0.64 mmol) and *N*-Ethyl-*N'*-(3-dimethylaminopropyl) carbo- diimide hydrochloride (184 mg, 0.96 mmol) in 5 mL of CH_2Cl_2, compound **7** (144 mg, 0.64 mmol) was added. The reaction mixture was stirred at room temperature for 8 h and the progress was monitored by TLC. The reaction mixture was washed with water (10 mL) and the organic layer was dried by Na_2SO_4 and concentrated under reduced pressure. The residue was purified by flash chromatography on silica gel (EtOAc/*n*-hexane = 1:3) to afford **3b** (118 mg, 54% yield in two steps) as a white solid. Mp 160.9 – 161.4 ºC; ^{1}H-NMR (500 MHz, $CDCl_3$): δ 7.78 (d, *J* = 8.6 Hz, 2H), 7.35 (d, *J* = 8.6 Hz, 2H), 7.30 (d, *J* = 8.7 Hz, 2H), 6.88 (d, *J* = 8.7 Hz, 2H), 5.75 (s, 1H), 4.17-4.10 (m, 2H), 3.77 (s, 3H), 2.81 (t, *J* = 6.75 Hz, 2H); ^{13}C-NMR (125 MHz, $CDCl_3$): δ 160.6, 160.1, 148.3, 137.5, 128.8 (2C), 128.3 (2C), 128.1 (2C), 127.9, 126.4, 117.2, 114.5 (2C), 76.8, 55.3, 43.4, 16.5; FT-IR (KBr): 2959, 2838, 2251, 1685, 1636, 1611, 1514, 1493, 1441, 1403, 1352, 1328, 1307, 1250, 1178, 1109, 1091, 1031, 1014, 838, 791, 774, 722, 677, 647, 630 cm^{-1}; HR-MS (FAB+): *m/z* calcd for $C_{19}H_{17}ClN_3O_3$ $[M+H]^+$: 370.0958, found: 370.0961.

3-(6-([1,1'-biphenyl]-4-yl)-2-(4-chlorophenyl)-5-oxo-5,6-dihydro-4*H*-1,3,4-oxa-

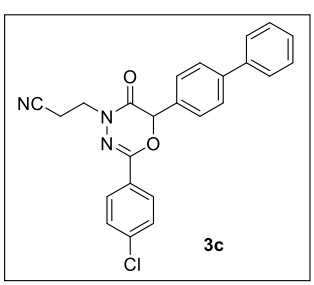

diazin-4-yl) propanenitrile (3c). Compound **6c** (125 mg, 0.25 mmol) was reacted according to the general procedure to yield **3c** (90 mg, 86%) as a white solid. Mp 108.7 – 109.2 ºC; ^{1}H-NMR (500 MHz, $CDCl_3$): δ

7.84 (d, *J* = 8.6 Hz, 2H), 7.59 (d, *J* = 8.2 Hz, 2H), 7.53 (d, *J* = 7.4 Hz, 2H), 7.46 (d, *J* = 8.2 Hz, 2H), 7.43-7.33 (m, 5H), 5.87 (s, 1H), 4.15 (t, *J* = 6.8 Hz, 2H), 2.82 (t, *J* = 6.8 Hz, 2H) ; ^{13}C-NMR (125 MHz, $CDCl_3$): δ 159.8, 148.2, 142.6, 140.1, 137.6, 133.1, 128.9 (2C), 128.8 (2C), 128.1 (2C), 127.8 (2C), 127.7 (2C), 127.1 (2C), 127.0 (2C), 117.2, 76.9, 43.5, 16.5; FT-IR (KBr): 3032, 2310, 1685, 1638, 1599, 1491, 1403, 1248, 1162, 1092, 1014, 839, 757, 736, 697 cm^{-1}; HR-MS (FAB+): *m/z* calcd for $C_{24}H_{19}ClN_3O_2$ $[M+H]^+$: 416.1166, found: 416.1176.

3-(2-(4-chlorophenyl)-5-oxo-6-phenyl-5,6-dihydro-4*H*-1,3,4-oxadiazin-4-yl)propanenitrile (3d). Compound **6d** (185 mg, 0.44 mmol) was reacted according to the general procedure to yield **3d** (137 mg, 92%) as a white solid. Mp 119.6 – 120.5 ºC; ^{1}H-NMR (500 MHz, $CDCl_3$): δ 7.81 (d, *J* = 8.6 Hz, 2H), 7.39-7.35 (m, 7H), 5.82 (s, 1H), 4.12 (t, *J* = 6.75 Hz, 2H), 2.80 (t, *J* = 6.75 Hz, 2H) ; ^{13}C-NMR (125 MHz, $CDCl_3$): δ 159.8, 148.1, 137.5, 134.3, 129.6, 129.1 (2C), 128.8 (2C), 128.0 (2C), 127.8, 126.6 (2C), 117.1, 76.7, 43.4, 16.4; FT-IR (KBr) 3065, 2956, 2309, 2251, 1685, 1638, 1599, 1492, 1403, 1361, 1330, 1270, 1197, 1163, 1108, 1092, 1014, 839, 758, 722, 699, 616 cm^{-1}; HR-MS (FAB+): *m/z* calcd for $C_{18}H_{15}ClN_3O_2$ $[M+H]^+$: 340.0853, found: 340.0859.

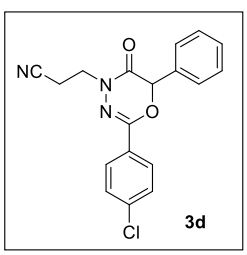

4-(2-(4-chlorophenyl)-4-(2-cyanoethyl)-5-oxo-5,6-dihydro-4*H*-1,3,4-oxadiazin-6-yl)phenyl acetate (3e). Compound **6e** (264 mg, 0.55 mmol) was reacted according to the general procedure to yield **3e** (150 mg, 68%) as a white solid. Mp 139.3 – 139.9 ºC; ^{1}H-NMR (500 MHz, $CDCl_3$): δ 7.81 (d, *J* = 8.7 Hz, 2H), 7.41 (d, *J* = 8.6

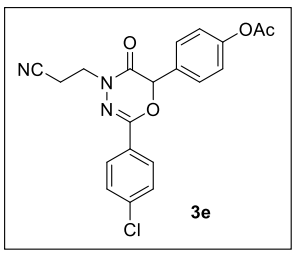

Hz, 2H), 7.37 (d, *J* = 8.7 Hz, 2H), 7.10 (d, *J* = 8.6 Hz, 2H), 5.82 (s, 1H), 4.15-4.05 (m, 2H), 2.78 (t, *J* = 6.75 Hz, 2H), 2.26 (s, 3H); ^{13}C-NMR (125 MHz, $CDCl_3$): δ 169.0, 159.5, 151.5, 147.9, 137.6, 131.7, 128.8 (2C), 128.0 (2C), 127.8 (2C), 127.6, 122.3 (2C), 117.1, 76.4, 43.4, 21.0, 16.4; FT-IR (KBr): 2349, 2309, 1761, 1685, 1638, 1508, 1493, 1403, 1369, 1201, 1169, 1092, 1014, 912, 840, 773, 721 cm^{-1}; HR-MS (FAB+): *m/z* calcd for $C_{20}H_{17}ClN_3O_4$ $[M+H]^+$: 398.0908, found: 398.0904.

3-(6-(4-benzoylphenyl)-2-(4-chlorophenyl)-5-oxo-5,6-dihydro-4*H*-1,3,4-oxadiazin-4-yl)propanenitrile (3f). Compound **6f** (82 mg, 0.16 mmol) was reacted at room temperature according to the general procedure to yield **3f** (52 mg, 75%) as a white solid. Mp 136.4 – 137.0 ºC; ^{1}H-NMR (500 MHz, $CDCl_3$): δ 7.84 (d, *J* = 8.6 Hz, 2H), 7.80 (d, *J* = 8.3 Hz, 2H), 7.75 (d, *J* = 7.5 Hz, 2H), 7.57 (t, *J* = 7.42 Hz, 1H), 7.53 (d, *J* = 8.2 Hz, 2H), 7.45 (t, *J* = 7.7 Hz, 2H), 7.39 (d, *J* = 8.7 Hz, 2H), 5.92 (s, 1H), 4.13 (t, *J* = 6.7 Hz, 2H), 2.81 (t, *J* = 6.7 Hz, 2H); ^{13}C-NMR (125 MHz, $CDCl_3$): δ 195.8, 159.2, 148.0, 138.6, 138.1, 137.7, 137.0, 132.7, 130.6 (2C), 130.0 (2C), 128.9 (2C), 128.4 (2C), 128.0 (2C), 127.4, 126.4 (2C), 117.1, 76.5, 43.4, 16.4; FT-IR (KBr): 3726, 3706, 3625, 3063, 2382, 2360, 2349, 2308, 2251, 1686, 1659, 1598, 1492, 1446, 1402, 1351, 1317, 1279, 1109, 1091, 1014, 939, 926, 839, 720, 701, 677 cm^{-1}; HR-MS (FAB+): *m/z* calcd for $C_{25}H_{19}ClN_3O_3$ $[M+H]^+$: 444.1115, found: 444.1123.

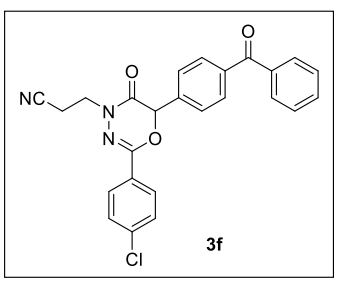

3-(6-(4-acetylphenyl)-2-(4-chlorophenyl)-5-oxo-5,6-dihydro-4*H*-1,3,4-oxadiazin-4-yl)propanenitri-le (3g). Compound **6g** (10 mg, 0.04 mmol) was reacted at room temperature according to the general procedure to yield **3g** (8 mg, 98%) as a white solid. Mp 197.7 – 198.4 ºC; ^{1}H-NMR (600 MHz, $CDCl_3$): δ 7.96 (d, *J* = 8.2 Hz, 2H), 7.82 (d, *J* = 8.7 Hz, 2H), 7.52 (d, *J* = 8.2 Hz, 2H), 7.38 (d, *J* = 8.7 Hz, 2H), 5.88 (s, 1H), 4.14-4.09 (m, 2H), 2.80 (dd, J_1 = 6.9 Hz, J_2 = 1.9 Hz, 2H), 2.56 (s, 3H); ^{13}C-NMR (150 MHz, $CDCl_3$): δ 197.2, 159.2, 148.0, 138.8, 137.9, 137.8, 129.0 (4C), 128.0 (2C), 127.4, 126.8 (2C), 117.0, 76.5, 43.5, 26.7, 16.4; FT-IR (KBr) 3726, 3625, 2349, 2308, 1685, 1640, 1491, 1402, 1362, 1267, 1091, 1013, 838, 679, 649 cm^{-1}; HR-MS (FAB+): *m/z* calcd for $C_{20}H_{17}ClN_3O_3$ $[M+H]^+$: 382.0958, found: 382.0945.

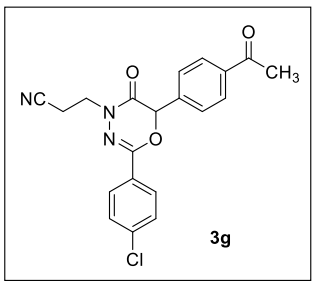

3-(2-(4-chlorophenyl)-5-oxo-6-(4-trifluoromethylphenyl)-5,6-dihydro-4*H*-1,3,4-oxadiazin-4-yl)propanenitrile (3h). Compound **6h** (18 mg, 0.04 mmol) was reacted at room temperature according to the general procedure to yield **3h** (15 mg, 97%) as a white solid. Mp 108.3 – 109.3 ºC; ^{1}H-NMR (500 MHz, $CDCl_3$): δ 7.83 (d, *J* = 8.6 Hz, 2H), 7.64 (d, *J* = 8.2 Hz, 2H), 7.55 (d, *J* = 8.2 Hz, 2H), 7.39 (d, *J* = 8.6 Hz, 2H), 5.89 (s, 1H), 4.11 (t, *J* = 6.7 Hz, 2H), 2.80 (t, *J* = 6.7 Hz, 2H); ^{13}C-NMR (125 MHz, $CDCl_3$): δ 159.1, 147.9, 137.9, 137.8, 131.7 (q, *J* = 32.6 Hz), 128.9 (2C), 128.0 (2C), 127.3, 126.9 (2C), 126.0 (q, *J* = 3.5 Hz, 2C), 123.6 (d, *J* = 271 Hz), 117.1, 76.3, 43.4, 16.4; FT-IR (KBr): 3725, 3624, 2381, 2359, 2349, 2308, 1487, 1640, 1493, 1404, 1326, 1167, 1126, 1092, 1067, 1015, 839, 778, 720, 672, 649 cm^{-1}; HR-MS (FAB+): *m/z* calcd for $C_{19}H_{13}ClF_3N_3O_2$ $[M+H]^+$:

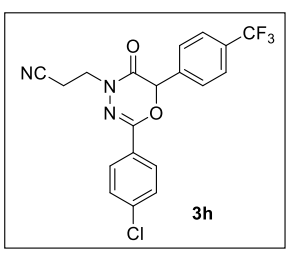

407.0648, found: 407.0644.

3-(2-(4-chlorophenyl)-6-(4-nitrophenyl)-5-oxo-5,6-dihydro-4*H*-1,3,4-oxadiazin-4-yl)propanenitrile (3i). 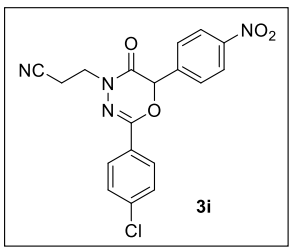

3i

Compound **6i** (70 mg, 0.15 mmol) was reacted at 0 ºC according to the general procedure to yield **3i** as a white solid (29 mg, 50%). Mp 157.6 – 158.4 ºC; ^{1}H-NMR (500 MHz, $CDCl_3$): δ 8.23 (d, *J* = 8.7 Hz, 2H), 7.84 (d, *J* = 8.6 Hz, 2H), 7.63 (d, *J* = 8.7 Hz, 2H), 7.40 (d, *J* = 8.6 Hz, 2H), 5.93 (s, 1H), 4.14-4.07 (m, 2H), 2.82-2.79 (m, 2H); ^{13}C-NMR (125 MHz, $CDCl_3$): δ 158.6, 148.5, 147.7, 140.6, 137.9, 129.0 (2C), 127.9 (2C), 127.5 (2C), 127.1, 124.1 (2C), 117.0. 75.9, 43.4, 16.4; FT-IR (KBr): 3726, 3080, 2349, 2308, 2251, 1686, 1639, 1600, 1524, 1493, 1403, 1349, 1271, 1161, 1110, 1092, 1014, 839, 735, 721, 694, 652 cm^{-1}; HR-MS (FAB+): *m/z* calcd for $C_{18}H_{14}ClN_4O_4$ $[M+H]^+$: 385.0704, found: 385.0700.

3-(6-(4-nitrophenyl)-5-oxo-2-(thiazol-2-yl)-5,6-dihydro-4*H*-1, 3,4-oxadiazin-4-yl)propanenitrile (3j). 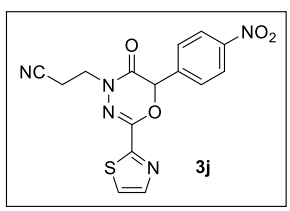

3j

Compound **6n** (13 mg, 0.03 mmol) was reacted at room temperature according to the general procedure to yield **3j** as a white solid (8 mg, 73%). Mp 163.5 – 164.1 ºC; ^{1}H-NMR (400 MHz, $CDCl_3$): δ 8.27 (d, *J* = 8.8 Hz, 2H), 8.00 (d, *J* = 3.2 Hz, 1H), 7.75 (d, *J* = 8.4 Hz, 2H), 7.58 (d, *J* = 2.8 Hz, 1H), 6.07 (s, 1H), 4.22-4.09 (m, 2H), 2.83 (td, *J* = 6.8, 2.8 Hz, 2H) ^{13}C-NMR (100 MHz, $CDCl_3$): δ 158.8, 156.6, 148.7, 144.9, 144.4, 140.0, 127.5 (2C), 124.3 (2C), 123.6, 116.8, 76.5, 43.6, 16.6; HR-MS (ESI+): m/z calcd for $C_{15}H_{11}N_5O_4S$ [M+H]+: 358.0605, found: 368.0619.

4.1.4 Synthesis of 4

4-chloro-*N'*-(2-cyanoethyl)-*N'*-(2-(4-nitrophenyl)-2-oxoacetyl)benzohydrazide

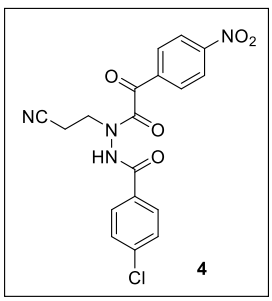

(4). A round-bottom flask equipped with a stir bar was charged with compound **3i** (12 mg, 0.031 mmol), CH_3CN (4 mL) and K_2CO_3 (43 mg, 0.31 mmol). The reaction mixture was stirred at room temperature for 1 h. The reaction mixture was filtered to remove K_2CO_3 and concentrated under reduced pressure. The crude product was purified by flash chromatography on silica gel (EtOAc/CH_2Cl_2/*n*-hexane = 1:1:2) to afford **4** (4 mg, 36%) as a white solid. Mp 201.4 – 202.4 ºC; ^{1}H-NMR (800 MHz, DMSO-d_6): δ 11.46 (s, 1H, -CONH), 8.37 (d, *J* = 8.8 Hz, 2H), 8.13 (d, *J* = 8.8 Hz, 2H), 7.62 (d, *J* = 8.6 Hz, 2H), 7.53 (d, *J* = 8.6 Hz, 2H), 4.28 (bs, 1H), 3.74 (bs, 1H), 2.92 (bs, 2H); ^{13}C-NMR (200 MHz, DMSO-d_6): δ 188.9, 167.0, 165.6, 150.9, 137.5, 136.0, 130.7 (2C), 129.7, 129.4 (2C), 128.7 (2C), 124.1 (2C), 119.0, 42.8, 15,7; FT-IR (KBr): 3282, 2926, 2253, 1785, 1689, 1598, 1527, 1485, 1407, 1349, 1271, 1227, 1196, 1095, 1014, 848, 788, 759, 725, 703, 679 cm^{-1}; HR-MS (FAB+): *m/z* calcd for $C_{18}H_{14}ClN_4O_5$ $[M+H]^+$: 401.0653, found: 401.0665.

4.1.5 General synthetic procedure for 5

To a stirred solution of compound 3 in CH_3CN, K_2CO_3 (10.0 equiv.) was added, and the reaction mixture was stirred at room temperature. On completion, the reaction mixture was filtered to remove K_2CO_3 and concentrated under reduced pressure. The residue was purified by flash chromatography on silica gel to give 5.

5-(4-chlorophenyl)-3-(2-isocyanoethyl)-1,3,4-oxadiazol-2(3*H*)-one (5a). 5a was

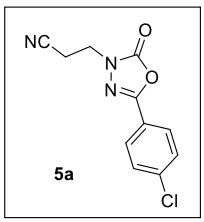

obtained from **6f**, **6g**, **6h**, **6i** (Table 3) or **3i**. **6i** (9 mg, 0.02 mmol) was reacted at room temperature according to the general procedure to yield **5a** (5.7 mg, 88%) as a white solid. Mp 119.4 – 120.9 ºC; ^{1}H-NMR (600 MHz, $CDCl_3$): δ 7.76 (d, *J* = 8.7 Hz, 2H), 7.44 (d, *J* = 8.2 Hz, 2H), 4.09 (t, *J* = 6.9 Hz, 2H), 2.88 (t, *J* = 6.9 Hz, 2H); ^{13}C-NMR (150 MHz, $CDCl_3$): δ 153.3, 152.7, 138.3, 129.5 (2C), 127.1 (2C), 121.8, 116.1, 41.6, 17.1; FT-IR (KBr): 3725, 2349, 2309, 1769, 1490, 1457, 1406, 1362, 1092, 1011, 838, 742, 679, 656 cm^{-1}; HR-MS (FAB+): *m/z* calcd for $C_{11}H_9ClN_3O_2$ $[M+H]^+$: 250.0383, found: 250.0381.

3-(5-(4-methoxyphenyl)-2-oxo-1,3,4-oxadiazol-3(2*H*)-yl)propanenitrile (5b). 6j

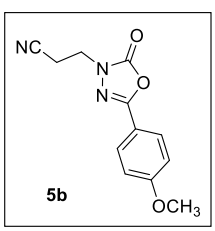

(9 mg, 0.02 mmol) was reacted at room temperature according to the general procedure to yield **5b** as a white solid (3.5 mg, 77%). Mp 115.9 – 116.8 ºC; ^{1}H-NMR (800 MHz, $CDCl_3$): δ 7.76 (d, *J* = 8.9 Hz, 2H), 6.96 (d, *J* = 9.0 Hz, 2H), 4.07 (t, *J* = 6.9 Hz, 2H), 3.85 (s, 3H), 2.87 (t, *J* = 6.9 Hz, 2H); ^{13}C-NMR (200 MHz, $CDCl_3$): δ 162.5, 154.1, 153.0, 127.6 (2C), 116.2, 115.7, 114.5 (2C), 55.5, 41.5, 17.1 ; HR-MS (ESI+): *m/z* calcd for $C_{12}H_{12}N_3O_3$ $[M+H]^+$: 246.0873, found: 246.0883.

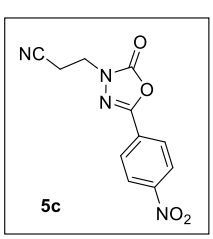

3-(5-(4-nitrophenyl)-2-oxo-1,3,4-oxadiazol-3(2*H*)-yl)propanenitrile (5c). 6k (10 mg, 0.021 mmol) was reacted at room temperature according to the general procedure to yield **5c** as a white solid (4 mg, 73%). Mp 161.5 – 162.4 ºC; ^{1}H-NMR (400

MHz, $CDCl_3$): δ 8.36 (d, *J* = 9.2 Hz, 2H), 8.04 (d, *J* = 9.2 Hz, 2H), 4.17 (t, *J* = 7.0 Hz, 2H), 2.93 (t, *J* = 6.6 Hz, 2H) ^{13}C-NMR (200 MHz, $CDCl_3$): δ 152.31, 152.18, 149.64, 128.77, 126.75 (2C), 124.40 (2C), 115.95, 41.86, 17.18; HR-MS (ESI+): *m/z* calcd for $C_{11}H_8N_4O_4$ $[M+Na]^+$: 283.0443, found: 283.0448.

3-(2-oxo-5-(pyridin-3-yl)-1,3,4-oxadiazol-3(2*H*)-yl)propanenitrile (5d). 6l (20

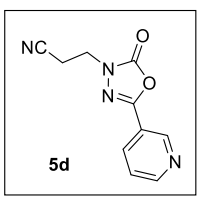

mg, 0.046 mmol) was reacted at room temperature according to the general procedure to yield **5d** as a white solid (7 mg, 70%). Mp 106.5 – 107.7 ºC; ^{1}H-NMR (400 MHz, $CDCl_3$): δ 9.10 (s, 1H), 8.78 (d, *J* = 4.4 Hz, 1H), 8.14 (d, *J* = 8.4 Hz, 1H), 7.47 (dd, *J* = 8.0, 4.8 Hz, 1H), 4.15 (t, *J* = 6.8 Hz, 2H), 2.92 (t, *J* = 7.0 Hz, 2H); ^{13}C-NMR (200 MHz, $CDCl_3$): 152.44, 152.39, 152.04, 146.86, 133.18, 123.80, 119.99, 116.04, 41.72, 17.14; HR-MS (ESI+): *m/z* calcd for $C_{10}H_9N_4O_2$ $[M+H]^+$: 217.0720, found: 217.0730.

3-(2-oxo-5-(pyridin-4-yl)-1,3,4-oxadiazol-3(2*H*)-yl)propanenitrile (5e). 6m (20

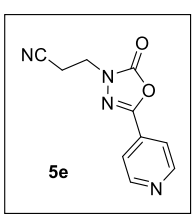

mg, 0.046 mmol) was reacted at room temperature according to the general procedure to yield **5e** as a white solid (7.5 mg, 75%). Mp 129.7 – 130.5 ºC; ^{1}H-NMR (400 MHz, $CDCl_3$): δ 8.80 (d, *J* = 6.0 Hz, 2H), 7.71 (d, *J* = 6.0 Hz, 2H), 4.16 (t, *J* = 6.8 Hz, 2H), 2.92 (t, *J* = 6.6 Hz, 2H); ^{13}C-NMR (200 MHz, $CDCl_3$): δ 152.28, 152.04, 150.64 (2C), 130.71, 119.21 (2C), 115.95, 41.83, 17.15; HR-MS (ESI+): *m/z* calcd for $C_{10}H_9N_4O_2$ $[M+H]^+$: 217.0720, found: 217.0726

4.1.6 Single crystal x-ray crystallographic data

Single Crystal X-ray Diffraction Studies. Single crystals of compound **3h** and **5a** with the dimension of 0.263 × 0.094 × 0.021 mm^3 and 0.157 × 0.134 × 0.069 mm^3, respectively, were obtained by the vapor diffusion method using dichloromethane / hexane solutions. The suitable crystals were introduced into Paraton-N oil and carefully mounted on the top of a nylon loop on SuperNova, Dual, Cu at zero, AtlasS2 diffractometer. The crystal was kept at 99.9 K for compound **3h** and 295.6 K for compound **5a** during data collection performed on SuperNova dual source diffractometer operating with Cu-K_α radiation (λ= 1.542 mm^{-1}). The structure was solved by direct methods with the ShelXT[1] structure solution program using Olex2[2] and refined by least squares minimization method using the ShelXL[3] incorporated in the refinement package. Details for data collection and structure refinement of compound **3h** and **5a** are summarized in Table S1-S12. Supplementary crystallographic data for this paper can be obtained free of charge from the Cambridge Crystallographic Data Centre (CCDC-1538325 and CCDC-1538326) via www.ccdc.cam.ac.uk/data_request/cif .

Crystal structure determination of 3h. Crystal Data for $C_{19}H_{13}ClF_3N_3O_2$ (*M* = 407.77 g/mol): monoclinic, space group $P2_1/n$ (no. 14), *a* = 5.77529(12) A, *b* = 22.1018(5) A, *c* = 14.0999(3) A, *β* = 101.1816(19)°, *V* = 1765.61(6) A^3, Z = 4, *T* = 99.9(3) K, μ(CuKα) = 2.396 mm^{-1}, *Dcalc* = 1.534 g/cm^3, 23127 reflections measured (7.54° ≤ 2Θ ≤ 153.392°), 3602 unique (R_{int} = 0.0444, R_{sigma} = 0.0332) which were used in all calculations. The final R_1 was 0.0605 (I >2σ(I)) and *w*R_2 was 0.1110 (all data).

Crystal structure determination of 5a. Crystal Data for $C_{11}H_8ClN_3O_2$ (*M* = 249.65 g/mol): triclinic, space group P-1 (no. 2), *a* = 5.7810(2) A, *b* = 8.5176(3) A, *c* = 11.7466(4) A, α = 102.453(3)°, β = 90.500(2)°, γ = 98.113(2)°, *V* = 558.69(3) A^3, *Z* = 2, *T* = 295.6(2) K, μ(CuKα) = 2.993 mm^{-1}, *Dcalc* = 1.484 g/cm^3, 10790 reflections measured (7.714° ≤ 2Θ ≤ 152.808°), 2339 unique (R_{int} = 0.0198, R_{sigma} = 0.0140) which were used in all calculations. The final R_1 was 0.0345 (I > 2σ(I)) and wR_2 was 0.0989 (all data).

Table 1. Crystallographic data of **3h** and **5a**

	3h	**5a**
molecular formula	$C_{19}H_{13}ClF_3N_3O_2$	$C_{11}H_8ClN_3O_2$
formula weight	407.77	249.65
crystal system	monoclinic	Crystal system
space group	$P2_1/n$	Space group
a [Å]	5.77529(12)	a/Å
b [Å]	22.1018(5)	b/Å
c [Å]	14.0999(3)	c/Å
α [°]	90	α/°
β [°]	101.1816(19)	β/°
γ [°]	90	γ/°
V [$Å^3$]	1765.61(6)	Volume/$Å^3$
Z	4	Z
ρ_{calcd} [g cm^{-3}]	1.534	$\rho_{calc}g/cm^3$
μ [mm^{-1}]	2.396	μ/mm^{-1}
F(000)	832.0	F(000)
reflns measured	23127	10790
unique reflns (R_{int})	3602 (0.0444)	2339 (0.0198)
R_1 [$I > 2\sigma(I)$]	0.0605	0.0345
wR_2 (all data)	0.1087	0.0966
Goodness of fit	1.118	1.054

4.2 Experiments described in chapter II

4.2.1 General information

All reagents and starting materials were purchased from commercial venders and used without further purification, unless otherwise noted. All reactions were carried out under nitrogen atmosphere using oven-dried glassware. Reactions were monitored by thin layer chromatography carried out on silica gel 60 F254 plate (Merck, Darmstadt, Germany) using UV illumination at 254 nm (VL-4.LC, Vilber Lourmat, Eberhardzell, Germany), $KMnO_4$ or anisaldehyde staining. Column chromatography was performed using ZEOprep silica gel (230~400 mesh; Zeochem, Lake Zurich, Switzerland) with hexane, ethyl acetate as eluents. ^{1}H-(300, 400 MHz) and ^{13}C-NMR (100 MHz) spectra were recorded on a GEMINI 2000 (VARIAN, Palo Alto, CA, USA), JNM-ECZ400s (JEOL, Tokyo, Japan) and JNM-ECA-600 (JEOL, Tokyo, Japan) at ambient temperature. Chemical shifts (δ) are reported in parts per million (ppm) referenced with respect to residual solvent peak ($CDCl_3$ = 7.26 ppm) and coupling constants (*J*) are reported in hertz (Hz). The multiplicity of peaks is indicated as follows: s (singlet), d (doublet), t (triplet), q (quartet), m (muliplet) bs (broad singlet). All ESI-MS were recorded on a 6130 Single Quadrupole LC/MS (Agilent Technologies, Santa Clara, CA, USA) and high-resolution mass spectra (HR-MS) were acquired under fast atom bombardments (FAB) condition on a JMS-700 MStation (JEOL, Tokyo, Japan). Reagents for click reaction including Tris(2-carboxyethyl)phosphine hydrochloride (TCEP), tris[(1-benzyl-1*H*-1,2,3-triazol-4-yl)methyl]amine (TBTA) and Rhodamine 110-azide were purchased from Sigma-Aldrich. In-gel fluorescence scanning of the SDS-PAGE was carried out with

ImageQuant LAS4000 (GE Healthcare Life Sciences, Marlborough, MA, USA). LC–MS/MS analysis was carried out using an LTQ-Orbitrap Velos mass spectrometer (Thermo Scientific, Waltham, MA, USA) equipped with the LTQ Velos dual cell linear trap.

4.2.2 Synthesis of OPAL-6

***tert*-Butyl-(1,3-dioxoisoindolin-2-yl)(2-(3-methyl-3*H*-diazirin-3-yl)ethyl)carbamate** (**15**) To a stirred solution of **13** (0.35 g, 1.3 mmol), **9** (0.2 g, 2.0 mmol) and PPh_3 (0.53 g, 2.0 mmol) in 5 mL dry THF under the nitrogen was added DIAD (diisopropyl azodicarboxylate, 0.35 g, 1.3 mmol) in one portion at 0 °C. The reaction mixture was stirred for 2 h and the solvent was removed in vacuo. The residual was purified by column chromatography (EtOAc : *n*-Hex = 1 : 2) to yield **15** (0.42 g, 93%). R_f =0.60 (EtOAc /*n*-Hex 1:1); ^{1}H-NMR (300 MHz, $CDCl_3$): δ 7.92-7.87 (m, 2H), 7.82-7.76 (m, 2H), 3.62-3.54 (m, 2H), 1.71-1.65 (m, 2H), 1.04 (s, 3H), 1.52*/ 1.30 (s, 9H). *represents the isomer

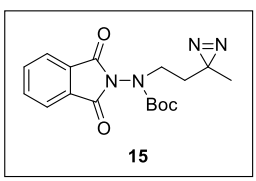

15

***tert*-Butyl-1-(2-(3-methyl-3*H*-diazirin-3-yl)ethyl)hydrazine-1-carboxylate (16)** Hydrazine mono- hydrate (0.09 mL, 1.8 mmol) was added dropwise slowly at -20 °C to a suspension of **15** (0.42 g, 1.21 mmol) in 5 mL ethanol. The resulting solution was warmed to room temperature, and a precipitate was filtered off after 30 min. The filtrate was concentrated and washed by 10 mL water, and the mixture was extracted by 3×10 mL dichloromethane. The combined organic layer was dried over anhydrous Na_2SO_4 and the solvent was evaporated to yield the product **16**. The crude product was used

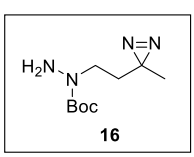

16

directly for the next step without further purification. (0.13 g, 50%). R_f =0.32 (CH_2Cl_2 /MeOH 10:1); ^{1}H-NMR (300 MHz, $CDCl_3$): δ 3.93 (-NH_2, bs, 2H), 3.41 (t, *J* = 6.6 Hz, 2H), 1.56 (t, *J* = 6.9 Hz, 2H), 1.48 (s, 9H), 1.04 (s, 3H).

***tert*-Butyl-2-(4-ethynylbenzoyl)-1-(2-(3-methyl-3*H*-diazirin-3-yl)ethyl)hydrazine-1-carboxylate (18)** To a stirred solution of **16** (0.13 g, 0.61 mmol), EDC (0.17 g, 0.91 mmol), **17** (89 mg, 0.61 mmol) in dichloromethane (4 mL) was added *N*,*N*-Diisopropylethylamine (DIPEA, 0.106 mL, 0.61 mmol) and the reaction mixture was stirred overnight at room temperature. The reaction was quenched with 3 mL of water and extracted with dichloromethane (3 × 10 mL). The combined organic layer was dried over anhydrous sodium sulfate. Upon concentration under reduced pressure, the residue was purified by column chromatography on silica gel (EtOAc/*n*-hexane = 1:2) to give **18** (78 mg, 38%). R_f =0.63 (EtOAc /*n*-Hex 1:1); ^{1}H-NMR (300 MHz, $CDCl_3$): δ 7.91 (-NH, bs, 1H), 7.82-7.73 (d, *J* = 7.8 Hz, 2H), 7.57 (d, *J* = 7.8 Hz, 2H), 3.65 (t, *J* = 6.9 Hz, 2H), 3.23 (s, 1H), 1.62 (t, *J* = 6.9 Hz, 2H), 1.46 (bs, 9H), 1.06 (s, 3H).

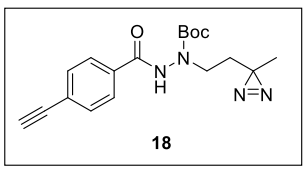

18

4-Ethynyl-*N*′-(2-(3-methyl-3*H*-diazirin-3-yl)ethyl)benzohydrazide (1a) To a suspension of **18** (78 mg, 0.23 mmol) in ethyl acetate (3 mL) was added dropwise concentrated hydrochloric acid (5 drops) and reaction mixture was stirred at room temperature for 2 h. Subsequently, the reaction was quenched by the addition of saturated aqueous sodium bicarbonate (5 mL) and the resulting mixture was extracted with ethyl acetate (3 × 10 mL). The organic phase was dried over

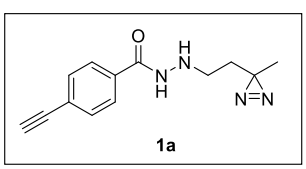

1a

anhydrous magnesium sulfate and concentrated *in vacuo*. The resulting residue was used for the next step without further purification. (51 mg, 91%). R_f =0.52 (EtOAc /*n*-Hex 1:1); ^{1}H-NMR (300 MHz, $CDCl_3$): δ 7.71 (d, *J* = 6.9 Hz, 2H), 7.56 (d, *J* = 6.0 Hz, 2H), 3.22 (s, 1H), 2.92 (t, *J* = 7.2 Hz, 2H), 1.60 (t, *J* = 7.2 Hz, 2H), 1.08 (s, 3H).

2-(4-Ethynylphenyl)-4-(2-(3-methyl-3*H*-diazirin-3-yl)ethyl)-6-phenyl-4*H*-1,3,4-oxadiazin-5(6*H*)-one (OPAL-6) To a stirred solution of **1a** (28 mg, 0.12 mmol) in acetonitrile was added α-chlorophenylacetyl chloride (22 μL, 0.14 mmol). The reaction mixture was refluxed for 2 h and cooled to ~ 60 ºC. After adding anhydrous potassium carbonate (159 mg, 1.15 mmol), the resulting mixture was stirred at 60 ºC for 1 h. The reaction mixture was cooled down to room temperature and the potassium carbonate was removed by filtration. The filtrate was concentrated under reduced pressure and the residue was purified with column chromatography (EtOAc / *n*-Hex = 1 : 5) to obtain the **OPAL-6** as a white solid (23 mg, 52%). R_f =0.71 (EtOAc /*n*-Hex 1:3); ^{1}H-NMR (400 MHz, $CDCl_3$): δ 7.84 (d, *J* = 8.4 Hz, 2H), 7.51 (d, *J* = 8.8 Hz, 2H), 7.44-7.40 (m, 2H), 7.39-7.36 (m, 3H), 5.83 (s, 1H), 3.95-3.82 (m, 2H), 3.19 (s, 1H), 1.78-1.69 (m, 2H), 1.07 (s, 3H); ^{13}C-NMR (100 MHz, $CDCl_3$): δ 159.6, 147.7, 134.8, 132.2 (2C), 129.8, 129.4, 129.0 (2C), 126.7 (2C), 126.4 (2C), 124.7, 83.0, 79.4, 77.1, 43.4, 32.8, 24.1, 19.4; HR-MS (FAB+): m/z calcd for $C_{21}H_{19}N_4O_2$ [M+H]+: 359.1508, found: 359.1508.

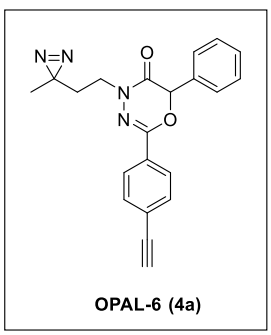

OPAL-6 (4a)

4.2.3 Synthesis of photoaffinity tag (9) for OPAL-8

6-Hydroxy-2,2-dimethyl-5-(pent-4-ynoyl)-4*H*-1,3-dioxin-4-one (6) A mixture of

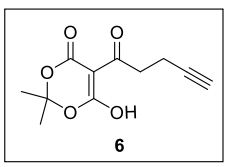

6

4-pentynoic acid (**5**, 1.90 g, 19.37 mmol), EDC (3.71 g, 19.37 mmol), 2,2-Dimethyl-1,3-dioxane-4,6-dione (Meldrum's acid, 2.79 g, 19.37 mmol) and 4-(Dimethylamino)pyridine (DMAP, 2.37 g, 21.31 mmol) were dissolved in dichloromethane (20 mL) and stirred at room temperature for 5 h under nitrogen. The reaction mixture was washed with 1N hydrochloric acid (20 mL) and extracted with dichloromethane (3 × 20 mL). The combined organic layer was dried over sodium sulfate, filtered and concentrated *in vacuo* to give **6** as a bright brown solid (3.95 g, 91%). R_f =0.13 (EtOAc /*n*-Hex 1:1); ^{1}H-NMR (300 MHz, $CDCl_3$): δ 15.23 (-OH, bs, 1H), 3.36 (t, *J* = 7.1 Hz, 2H), 2.64 (td, *J* = 7.1, 2.7 Hz, 2H), 2.00 (t, *J* = 2.7 Hz, 1H), 1.75 (s, 6H).

***tert*-Butyl 3-oxohept-6-ynoate (7)** A solution of **6** (3.52 g, 15.7 mmol) dissolved in

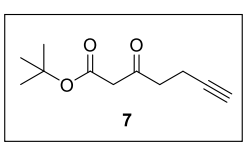

7

t-BuOH (20 mL) was stirred at 90 ºC for 5 h. The resulting mixture was concentrated *in vacuo* and the residue was purified with column chromatography (EtOAc / *n*-Hex = 1 : 20) to obtain the **7** as a pale yellow oil (2.51 g, 95%). R_f =0.47 (EtOAc /*n*-Hex 1:20); ^{1}H-NMR (300 MHz, $CDCl_3$): δ 3.38 (s, 2H), 2.80 (t, *J* = 7.2 Hz, 2H), 2.47 (td, *J* = 7.2, 2.7 Hz, 2H), 1.95 (t, *J* = 2.7 Hz, 1H), 1.46 (s, 9H).

3-Oxohept-6-ynoic acid (8) To stirred solution of **7** (2.51 g, 14.92 mmol) in

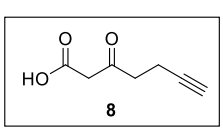

8

dichloromethane (10 mL) was added slowly trifluoroacetic acid (5 mL) and the reaction mixture was stirred at room temperature for 2 h. After removal of the dichloromethane and TFA by evaporation,

the remaining residue was suspended in ethyl acetate. The residue was precipitated, filtered washed with ethyl acetate and dried to give **8** as a grey solid. (1.75 g, 84%). R_f =0.41 (EtOAc /*n*-Hex 1:1); ^{1}H-NMR (300 MHz, $CDCl_3$): δ 3.50 (s, 2H), 2.77 (t, *J* = 7.2 Hz, 2H) 2.43 (td, *J* = 7.2, 2.7 Hz, 2H), 1.91 (t, *J* = 2.7 Hz, 1H).

2-(3-(But-3-yn-1-yl)-3*H*-diazirin-3-yl)acetic acid (9) To a solution of **8** (0.59 g, 4.22 mmol) in methanol (5 mL) at -78 ºC in a pressure vessel was added slowly 7 N ammonia in methanol (10 mL). The reaction mixture was stirred at -30 ºC for 3 h. Hydroxylamine *O*-sulfonic acid (0.72g, 6.34 mmol) in methanol was added into the reaction mixture, followed by warming to room temperature. After stirring overnight, the reaction mixture cooled down to -78 ºC, and the remaining ammonia was removed by gently stirring at room temperature with the vessel cap opened. The grey precipitate was filtered off and the filtrate was concentrated under the reduced pressure. The residual, diaziridine intermediate, was re-dissolved in methanol and cooled to 0 ºC. Subsequently, triethylamine (1.77 mL, 12.67 mmol) was added to the reaction mixture. Iodine was added slowly in a small portion until the color of the solution turned dark brown for more than 10 min. The resulting solution was evaporated and then diluted with dichloromethane, washed with 10% aqueous sodium metabisulfite, followed by extraction with dichloromethane (3 × 10 mL). The combined organic layer was dried over anhydrous sodium sulfate, filtered, and concentrated *in vacuo* to give the crude product, which was purified by column chromatography (EtOAc / *n*-Hex = 1 : 3) to yield the diazirine compound **9** as a light brown liquid (120 mg, 19 %). R_f =0.36 (CH_2Cl_2 /MeOH 20:1); ^{1}H-NMR (300 MHz, $CDCl_3$): δ 2.40 (s, 2H), 2.07 (td, *J* = 7.2, 2.7 Hz, 2H), 2.01 (t, *J* = 2.7 Hz, 1H), 1.80 (t, *J* = 7.2 Hz, 2H).

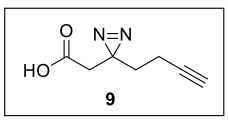

9

4.2.4 Synthesis of OPAL-8

3-(2-(4-Aminophenyl)-5-oxo-6-phenyl-5,6-dihydro-4*H*-1,3,4-oxadiazin-4-yl)pr-

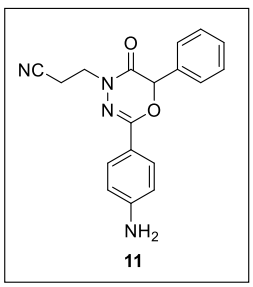

11

opanenitrile (11) The mixture of nitro compound **10** (151 mg, 0.43 mmol) and tin(II) chloride dihydrate (486 mg, 2.15 mmol) in 4 mL of ethanol was stirred at 80 ºC for 2 h. The reaction mixture was slowly cooled down to room temperature and a saturated sodium bicarbonate solution was added until the mixture was basic. The resulting cloudy solution was extracted with ethyl acetate (3 × 10 mL) and the organic layer was dried over anhydrous magnesium sulfate, filtered and concentrated *in vacuo* to yield **11** as a yellow solid (104 mg, 76%). R_f =0.33 (EtOAc /*n*-Hex 1:1); ^{1}H-NMR (300 MHz, $CDCl_3$): δ 7.70 (d, *J* = 9.0 Hz, 2H), 7.43-7.36 (m, 5H), 6.67 (d, *J* = 8.4 Hz, 2H), 5.79 (s, 1H), 4.11 (td, *J* = 6.6, 1.8 Hz, 2H), 2.82 (t, *J* = 6.6 Hz, 2H).

2-(3-(But-3-yn-1-yl)-3*H*-diazirin-3-yl)-N-(4-(4-(2-cyanoethyl)-5-oxo-6-phenyl-

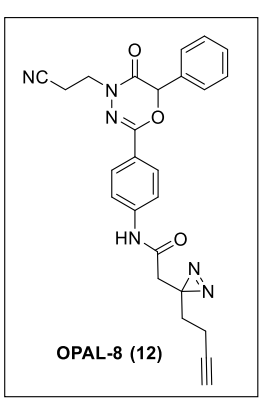

5,6-dihydro-4*H*-1,3,4-oxadiazin-2-yl)phenyl)acetamide (OPAL-8) To a stirred solution of **11** (64 mg, 0.20 mmol), EDC (57 mg, 0.30 mmol), and **9** (46 mg, 0.30 mmol) in dichloromethane (4 mL) was added triethylamine (28 μL, 0.20 mmol) and the reaction mixture was stirred at room temperature overnight. The reaction was quenched with 3 mL of water and extracted with dichloromethane (3 × 10 mL). The combined organic layer was dried over anhydrous sodium sulfate, filtered and concentrated *in vacuo.* The residue was purified by column chromatography (EtOAc/*n*-hexane = 1:2) to

give **OPAL-8** as a pale yellow liquid (61 mg, 67%). R_f =0.48 (EtOAc /*n*-Hex 1:1); ^{1}H-NMR (400 MHz, $CDCl_3$): δ 7.81 (d, *J* = 8.8 Hz, 2H), 7.59 (d, *J* = 8.8 Hz, 2H), 7.55 (-NH, bs, 1H), 7.42-7.37 (m, 5H), 5.84 (s, 1H), 4.14 (t, *J* = 7.2 Hz, 2H), 2.82 (t, *J* = 6.8 Hz, 2H), 2.45 (s, 2H), 2.12 (td, *J* = 7.2, 2.8 Hz, 2H), 2.05 (t, *J* = 2.8 Hz, 1H), 1.83 (t, *J* = 7.2 Hz, 2H); ^{13}C-NMR (100 MHz, $CDCl_3$): δ 166.1, 160.0, 148.6, 140.1, 134.4, 129.5 (2C), 129.1 (2C), 127.8 (2C), 126.6 (2C), 125.3, 119.5, 117.2, 82.7, 77.0, 69.7, 43.4, 42.7, 31.9, 25.9, 16.4, 13.3; HR-MS (FAB+): m/z calcd for $C_{25}H_{23}N_6O_3$ [M+H]+: 455.1832, found: 455.1827.

4.2.5 Synthesis of OPAL-10

***tert*-Butyl 1-(2-cyanoethyl)hydrazine-1-carboxylate (20)** To a stirred solution of

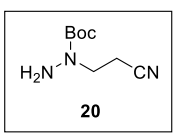

20

19 (0.32 g, 3.76 mmol) and trimethylamine (0.51 mL, 3.76 mmol) in dichloromethane (5 mL) at 0 ºC with an ice bath was added dropwise di-*tert*-butyl dicarbonate (0.81, 3.70 mmol) dissolved in dichloromethane (5 mL) from a dropping funnel. After completion of the addition, the reaction mixture was allowed to warm up to room temperature and stirred for 2 h. The resulting mixture was washed with water (10 mL) and extracted with dichloromethane (3 × 10 mL). The combined organic layer was dried over sodium sulfate, filtered and concentrated *in vacuo* to give the **20** as a pale yellow liquid (0.51 g, 76%). R_f =0.47 (EtOAc /*n*-Hex 1:2); ^{1}H-NMR (300 MHz, $CDCl_3$): δ 4.01 (-NH_2, bs, 2H), 3.68 (t, *J* = 6.6 Hz, 2H), 2.64 (t, *J* = 6.6 Hz, 2H), 1.49 (s, 9H).

***tert*-Butyl 1-(2-cyanoethyl)-2-(4-ethynylbenzoyl)hydrazine-1-carboxylate (21)** A

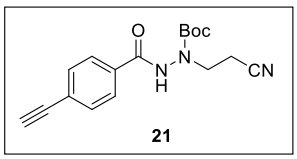

21

mixture of **20** (0.31 g, 1.66 mmol), EDC (0.48 g, 2.50 mmol), **17** (0.24 g, 1.66 mmol) were dissolved in dichloromethane (6 mL) and stirred overnight at room temperature. The reaction mixture was washed with water (10 mL) and extracted with dichloromethane (3 × 10 mL). The organic layer was dried over sodium sulfate, filtered and concentrated under reduced pressure. The residue was purified by column chromatography (EtOAc/*n*-hexane = 1:3) to yield **21** (0.22 g, 42%). R_f =0.33 (EtOAc /*n*-Hex 1:1); ^{1}H-NMR (300 MHz, $CDCl_3$): δ 8.15 / 7.96* (-NH, s, 1H), 7.75 (d, *J* = 7.2 Hz, 2H), 7.57 (bs, 2H), 3.89 (t, *J* = 6.9 Hz, 2H), 3.24 (s, 1H), 2.75 (bs, 2H), 1.53-1.42 (m, 9H). *represents the isomer

***N'*-(2-cyanoethyl)-4-ethynylbenzohydrazide (1b)** To a suspension of **21** (0.14 g,

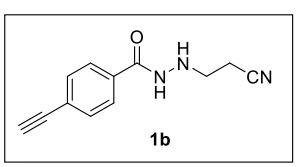

1b

0.44 mmol) in ethyl acetate (3 mL) was added dropwise concentrated hydrochloric acid (10 drops) and reaction mixture was stirred at room temperature for 2 h. The reaction mixture was quenched by the slow addition of saturated aqueous sodium bicarbonate (5 mL) and the resulting solution was extracted with ethyl acetate (3 × 10 mL). The organic phase was dried over anhydrous sodium sulfate, filtered, and concentrated to give the crude product, which was purified by column chromatography (EtOAc / *n*-Hex = 1:2) to yield the **1b** as a white solid (82 mg, 87%). R_f =0.14 (EtOAc /*n*-Hex 2:1); ^{1}H-NMR (300 MHz, $CDCl_3$): δ 7.73 (d, *J* = 8.4 Hz, 2H), 7.57 (d, *J* = 8.4 Hz, 2H), 3.26 (t, *J* = 6.2 Hz, 2H), 3.23 (s, 1H), 2.60 (t, *J* = 6.4 Hz, 2H).

***N′*-(2-(4-benzoylphenyl)-2-bromoacetyl)-N'-(2-cyanoethyl)-4-ethynylbenzohydrazide (3b)** To a stirred solution of **1b** (68 mg, 0.40 mmol) and **2b** (129 mg, 0.40 mmol) in 10 mL of CH_2Cl_2, *N*-ethyl-*N′*-(3-dimethylaminopropyl) carbodiimidehydrochloride (EDC·HCl, 155 mg, 0.81) was added. The reaction mixture was stirred at room temperature for 16 h. The reaction mixture was washed with brine (10 mL) and extracted with dichloromethane (3 × 10 mL). The organic layer was dried over anhydrous sodium sulfate and concentrated to give the crude product, which was further purified by column chromatography (EtOAc/*n*-hexane = 1:2) to afford **3b** (0.14 g, 66%). R_f =0.22 (EtOAc /*n*-Hex 1:1); ^{1}H-NMR (400 MHz, $CDCl_3$): δ 7.83-7.73 (m, 6H), 7.64-7.55 (m, 3H), 7.51-7.47 (m, 4H), 5.72 (s, 1H), 4.02 (bs, 2H), 3.30 (s, 1H), 2.78 (bs, 2H).

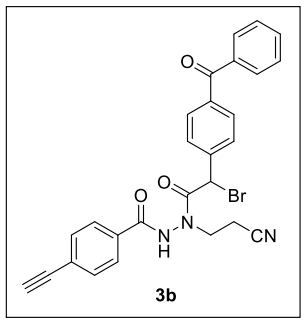

3b

3-(6-(4-benzoylphenyl)-2-(4-ethynylphenyl)-5-oxo-5,6-dihydro-4*H*-1,3,4-oxadiazin-4-yl)propanenitrile (OPAL-10) To a stirred solution of **3b** (61 mg, 0.12 mmol) in CH_3CN, potassium carbonate (K_2CO_3, 164 mg, 1.19 mmol) was added in one portion. The reaction mixture was stirred for 4 h at room temperature and filtered to remove K_2CO_3. The filtrate was concentrated under reduced pressure and the resulting residue was purified by column chromatography (EtOAc/n-hexane = 1:2) to give **OPAL-10** as a while solid (28 mg, 53%). R_f =0.32 (EtOAc /*n*-Hex 1:2); ^{1}H-NMR (600 MHz, $CDCl_3$): δ 7.87 (d, *J* = 8.7 Hz, 2H), 7.80 (d, *J* = 8.3 Hz, 2H), 7.75

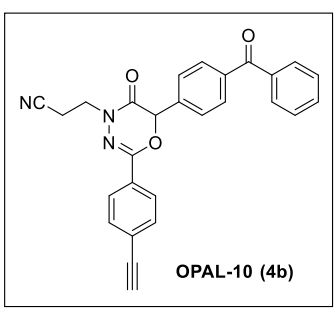

OPAL-10 (4b)

(d, *J* = 8.2 Hz, 2H), 7.57 (t, *J* = 7.4 Hz, 1H), 7.54-7.52 (m, 4H), 7.45 (t, *J* = 7.8 Hz, 2H), 5.92 (s, 1H), 4.13 (t, *J* = 6.9 Hz, 2H), 3.20 (s, 1H), 2.81 (t, *J* = 6.9 Hz, 2H); ^{13}C-NMR (150 MHz, $CDCl_3$): δ 195.8, 159.3, 148.1, 138.6, 138.1, 137.1, 132.7, 132.3 (2C), 130.6 (2C), 130.0 (2C), 129.1, 128.3 (2C), 126.6 (2C), 126.5 (2C), 125.3, 117.0, 82.8, 79.8, 76.6, 43.5, 16.4; HR-MS (FAB+): m/z calcd for $C_{27}H_{20}N_3O_3$ [M+H]+: 434.1505, found: 434.1500.

4.2.6 *In vitro* and i*n situ* labeling experiments

MCF-7 and A549 cells were grown under 5% CO_2 at 37 ºC, in RPMI (GenDEPOT, Katy, TX, USA) supplemented with 10 % heat-inactivated fetal bovine serum (FBS; GenDEPOT, Katy, TX, USA), penicillin, streptomycin and glutamine. HepG2 and HeLa cells were maintained in Dulbecco's modified Eagle medium (DMEM; GenDEPOT, Katy, TX, USA) containing 10 % FBS, penicillin and streptomycin. For *in vitro* labelling experiments, MCF-7, A549, HepG2 and HeLa cells were grown and lysed using 1 % Triton X-100 lysis buffer. The probes (10 μM) were incubated with whole lysates (50 μg) at room temperature for 1 h, followed by irradiation under 365 nm UV light (4 W; VL-4.LC, Vilber Lourmat, Eberhardzell, Germany) at 4 ºC for 20 min. The resulting photocrosslinked proteins were conjugated to rhodamine-azide (0.1 mM) by a click reaction using $CuSO_4$ (1 mM), TCEP (1 mM), and TBTA (0.1 mM) at room temperature for 2 h with gentle shaking. The samples were washed with pre-chilled acetone (500 μL) and precipitated by centrifugation (13,000 rpm, 10 min, 4 ºC), and the resulting pellets were washed again with pre-chilled methanol (200 μL× 2). The pellets were resuspended in 20 μL of 1×SDS buffer and were heated at 95 ºC for 10 min. The resulting proteins were separated by SDS-PAGE

(15%) and were visualized by in-gel fluorescence scanning in a LAS-4000 (GE Healthcare Life Sciences, Marlborough, MA, USA). For *in situ* labelling, cells were grown to 80-90% confluency in a 100 pi dish and were washed twice with cold PBS, followed by treatment with a DMSO stock solution of the probe (1000 to 1 ratio) and incubation at 37 ºC under 5% CO_2 for 5 h. The media were removed, and the cells were washed twice gently with cold PBS. Then, 5 mL of PBS was added, and the cells were irradiated under 365 nm UV light (4 W) at 4 ºC for 20 min. The cells were lysed using 1 % Triton X-100 lysis buffer and centrifuged. All the following experiments were similar to the protocols of the *in vitro* experiments.

For Western blotting analysis, protein samples were separated by SDS-polyacrylamide gels (SDS-PAGE) and transferred onto poly(vinylidene difluoride) membranes. The membranes were then blocked with skim milk (GenDEPOT, Katy, TX, USA) for 1 h at room temperature, followed by incubation with the corresponding primary antibodies at 4 ºC overnight. After washing with TBST (GenDEPOT, Katy, TX, USA), an appropriate secondary antibodies were added and further incubated at room temperature for 1 h. The blots were finally washed with TBST and scanned in a LAS-4000 (GE Healthcare Life Sciences, Marlborough, MA, USA). The excitation wavelength used for the in-gel fluorescence was 460 nm and the emission was >515 nm (Y515-Di, long path filter).

4.2.7 Recombinant protein expression

Production of recombinant bacmid. Recombinant pFastBac1-IGF-1R was constructed by inserting the kinase domain of IGF-1R, tagged with a GST tag at the N-terminus, into the EcoR I-HF and Xho I sites of the donor plasmid pFastBac1 (Addgene, Watertown, MA, USA). The recombinant plasmid was transformed into competent XL1 blue cells for selection, and the inserted sequence was confirmed by colony PCR. The Bac-to-Bac Baculovirus Expression system (Thermo Fisher Scientific, Waltham, MA, USA) was used to generate the recombinant bacmid. The plasmid pFastBac1-IGF-1R was transformed into competent DH10Bac™ *E. coli* cells (Thermo Fisher Scientific, Waltham, MA, USA) containing the bacmid and helper plasmid, followed by spreading on Luria Bertani (LB) agar plates containing antibiotics (kanamycin 50 μg/mL, tetracycline 10 μg/mL and gentamycin 7 μg/mL), X-gal (100 μg/mL), and IPTG (40 μg/mL). White colonies were selected, which resulted from the transposition of GST-IGF-1R into the bacmid and the disruption of the lac Z gene. Recombinant bacmid DNA was purified, and PCR analysis was performed to verify of the transposition.

Transfection and infection Sf21 cells. Sf21 cells (Thermo Fisher Scientific, Waltham, MA, USA) were grown to 1.5-3.75×10^6 cells/mL in suspension culture using Sf-900 II serum free media on a culture flask filter T75 (SPL Life Sciences, Gyeonggi-do, Korea). For transfection, 1 μg of recombinant bacmid containing IGF-1R, (purified using PureLink HiPure plasmid Miniprep Kit (Invitrogen, Carlsbad, CA, USA)) and Cellfectin II were diluted into unsupplemeted Grace's media (GenDEPOT, Katy, TX, USA) and were incubated at 28 ºC for 5 days in a humidified

incubator to generate the P1 viral stock. Sf21 cells were infected with the P1 viral stock (10^6 pfu/mL) at a multiplicity of infection (MOI) of 0.05-0.1 for 3 days, and the infected cells were harvested. The P2 viral stock (10^7 pfu/mL, MOI of 2.5-4.5) was collected with the same protocol used for the P1 stock. The cells infected with the P2 viral stock were harvested, washed with 10 mM potassium phosphate buffer (pH 7.2) containing 150 mM NaCl and centrifuged. The resulting cell pellets were stored at -80 ºC.

4.2.8 Photoaffinity labeling in insect cell lysate

Insect cell pellets containing overexpressed recombinant human IGF-1R were suspended in a lysis buffer (10 mM Tris-HCl, pH 8.0) and subjected to three cycles of freeze-thawing in lysis buffer, followed by centrifugation at 4 ºC at 13,000 rpm for 15 min. The total protein concentration of the supernatant was determined by measuring the absorbance at 280 nm, and the protein concentration was adjusted to 9.5 mg/mL. In a 96-well plate, 200 μg of cell lysate was treated with the OPAL probe (100 μM) and incubated in the dark at room temperature for 1 h with gentle shaking at 50 rpm. The mixtures were then irradiated with 350 nm UV light for 20 min at 4 ºC. Subsequently, conjugation to fluorescent reporter was conducted by click chemistry with rhodamine-azide (4 μL, 1 mM), $CuSO_4$ (2 μL ,1 mM), TCEP (2 μL,1 mM), TBTA (2 μL, 0.1 mM) in 6.6 μL of buffer (40 μL of total volume) for 2 h with gentle mixing (250 rpm) under the dark. The reaction was quenched by the addition of 500 μL of prechilled acetone, and the mixture was kept at -20 ºC for 30 min. The labelled proteins were precipitated by centrifugation at 13,000 rpm at 4 ºC for 15 min, and the pellet was washed twice with 200 μL of prechilled methanol. The pellets

were resuspended in 20 μL of 1×SDS buffer and were heated at 95 ºC for 10 min. The resulting proteins were separated by SDS-PAGE (15%) and were visualized by in-gel fluorescence scanning in a LAS-4000. The excitation wavelength used for the in-gel fluorescence was 460 nm and the emission was >515 nm (Y515-Di, long path filter).

4.2.9 LC-MS/MS analysis

The strong fluorescent band labelled for the overexpressed recombinant human IGF-1R at 59 kDa was cut out of the gel, followed by trypsin digestion. After extraction of the peptides using acetonitrile with 0.1% TFA, the peptide sequences of the samples were analysed using an LTQ-Orbitrap Velos mass spectrometer (Thermo Scientific, Waltham, MA, USA) with a nanoelectrospray ionization source. The MS/MS data were analysed with Thermo Proteome Discoverer Software (Thermo Fisher Scientific, Version 1.2.0.208), and a database search was performed using the SEQUEST algorithm for identification of the target proteins.

4.3 Experiments described in chapter III

4.3.1 General information

All reagents and solvents were purchased from commercial sources. These reagents were used without any further purification. The reaction was monitored by thin-layer chromatography (TLC) on silica coated plate (60 F254, Merck, Darmstadt, Germany) and components were visualized by UV light at 254 nm and 365 nm (VL-4.LC, Vilber Lourmat, Eberhardzell, Germany). Purification by column chromatography was performed on silica gel 230-400 mesh (ZEOprep, Zeochem, Lake Zurich, Switzerland) using a mixture of *n*-hexane, CH_2Cl_2 and EtOAc as eluents. ^{1}H-NMR (300, 400, 500, 600, or 800 MHz) and ^{13}C-NMR (100 or 125 MHz) spectra were recorded on a GEMINI 2000 (VARIAN, Palo Alto, CA, USA), FT-NMR Avance III HD (Bruker, Billerica, MA, USA), JNM-LA300 and JNM-ECA-600 (JEOL, Tokyo, Japan) at ambient temperature. The chemical shifts are reported in δ unit, parts per million (ppm) relative to $CHCl_3$ (7.24 ppm), DMSO (2.49 ppm) and MeOH (3.30 ppm) in the deuterated solvent and coupling constants (*J*) are expressed in hertz (Hz). High-resolution mass spectra (HRMS) were obtained using fast atom bombardments (FAB) method on a JMS-700 MStation (JEOL,Tokyo, Japan).

4.3.2 Synthesis of indolizino[3,2-*c*]quinoline derivatives

A mixture of compound **1** (1 equiv), ArCHO or RCHO (1.2 equiv) and $FeCl_3$ anhydrous (0.2 equiv) in dichloromethane (5 mL) was stirred at 60 ºC for 16 h. The reaction mixture was washed with water (5 mL) and the aqueous layer was extracted with dichloromethane (5 mL) three times. The combined organic layers were dried

over anhydrous sodium sulfate and concentrated to give the crude product, which was further purified by silica gel column chromatography (EtOAc/*n*-hexane) to afford the compound **2**.[152-153]

Methyl 6-(thiophen-2-yl)indolizino[3,2-c]quinoline-12-carboxylate (IQ44) 2-Thiophene-carboxaldehyde (108 mg, 0.96 mmol) was reacted according to the general procedure described above to yield **IQ44** (206 mg, 72%) as a pale yellow solid; mp 196.7 – 197.3 °C; ^{1}H-NMR ($CDCl_3$, 500 MHz) δ 9.63 (d, *J* = 8.5 Hz, 1H), 8.44 (d, *J* = 9.3 Hz, 1H), 8.25 (d, *J* = 7.7 Hz, 1H), 8.04 (d, *J* = 7.2 Hz, 1H), 7.73 (t, *J* = 7.0 Hz, 1H), 7.65 (t, *J* = 7.0 Hz, 1H), 7.61 (d, *J* = 5.0 Hz, 1H), 7.35-7.32 (m, 2H), 7.26 (dd, *J* = 7.0, 3.6 Hz, 1H), 6.67 (d, *J* = 6.8 Hz, 1H), 4.08 (s, 3H); ^{13}C-NMR ($CDCl_3$, 125 MHz) δ 165.7, 144.2, 141.6, 141.0, 140.0, 131.1, 129.6, 128.5, 128.2, 128.1, 127.9, 127.6, 127.5, 127.3, 126.3, 122.5, 122.3, 120.5, 112.2, 99.4, 51.5; HRMS (FAB+) calcd for $C_{21}H_{15}N_2O_2S$ $[M+H]^+$ 359.0854, found 359.0849.

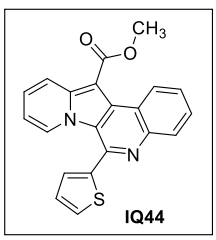

IQ44

Methyl 6-ethylindolizino[3,2-c]quinoline-12-carboxylate (IQ-B27) Propionaldehyde (32 mg, 0.55 mmol) was reacted at 40 ºC according to the general procedure described above to yield **IQ-B27** (51 mg, 36%) as an ivory solid; mp 148.3 – 148.6 °C; ^{1}H-NMR ($CDCl_3$, 400 MHz) δ 9.50 (dd, *J* = 8.2 ,1.4 Hz, 1H), 8.87 (d, *J* = 6.8 Hz, 1H), 8.48 (d, *J* = 9.2 Hz, 1H), 8.18 (d, *J* = 8.4 Hz, 1H), 7.70 (ddd, *J* = 15.0 ,6.8, 1.2 Hz, 1H), 7.59 (ddd, *J* = 15.2, 6.8, 1.2 Hz, 1H), 7.40 (dd, *J* = 9.2, 6.4 Hz, 1H), 7.00 (td, *J* = 6.8, 1.0 Hz), 4.08 (s, 3H), 3.54 (q, *J* = 7.2, 2H), 1.54 (t, *J* = 7.4, 3H);^{13}C-

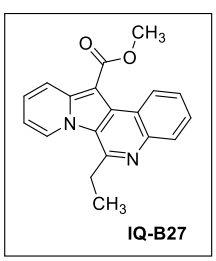

IQ-B27

NMR ($CDCl_3$, 100 MHz) δ 165.9, 150.1, 144.0, 141.2, 130.8, 128.6, 128.4, 127.6, 127.4, 126.9, 125.5, 122.9, 121.9, 120.9, 113.2, 99.6, 51.6, 31.3, 12.3; HRMS (FAB+) calcd for $C_{19}H_{17}N_2O_2$ $[M+H]^+$ 305.1290, found 305.1283.

Methyl 6-(furan-2-yl)indolizino[3,2-c]quinoline-12-carboxylate (IQ-B28) 2-

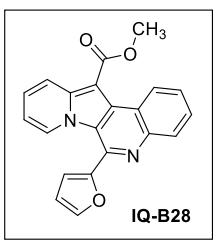

Furaldehyde (17 mg, 0.18 mmol) was reacted according to the general procedure described above to yield **IQ-B28** (27 mg, 51%) as a bright brown solid; mp 157.5 – 157.9 °C; ^{1}H-NMR ($CDCl_3$, 400 MHz) δ 9.65 (dd, *J* = 8.6, 1.4, 1H), 8.45 (d, *J* = 9.2, 1H), 8.30 (d, *J* = 8.4, 1H), 7.74 (td, *J* = 6.8, 1.6, 1H), 7.70-7.64 (m, 3H), 7.37 (dd, *J* = 8.0, 6.8, 1H), 7.08 (d, *J* = 3.2, 1H), 6.77 (td, *J* = 6.4, 1.2, 1H), 6.74 (dd, *J* = 3.4, 1.8, 1H), 4.08 (s, 3H); ^{13}C-NMR ($CDCl_3$, 100 MHz) δ 165.7, 150.4, 144.1, 143.6, 141.9, 137.6, 131.5, 129.5, 128.8, 127.9, 127.6, 127.5, 126.6, 122.7, 122.5, 120.6, 112.6 (2C), 112.2, 99.6, 51.6; HRMS (FAB+) calcd for $C_{21}H_{15}N_2O_3$ $[M+H]^+$ 343.1083, found 343.1085.

4.3.3 Optical characterization

The UV-Vis absorption spectra and steady-state fluorescence emission spectra were obtained at room temperature using a Lamda 25 (Perkin Elmer, Waltham, MA, USA) and a JASCO FP-6500 spectrofluorometer (Jasco, Tokyo, Japan), respectively. Stock solutions of IQ compounds in DMSO at a concentration of 10 mM were prepared for the optical measurements. 15 metal ions ($FeSO_4 \cdot 7H_2O$, $Fe(NO_3)_3 \cdot 9H_2O$, $CdCl_2$, KBr, NaCl, $Mg(NO_3)_2 \cdot 6H_2O$, $AgNO_3$, $Pb(NO_3)_2$, $CuCl_2 \cdot 2H_2O$, $ZnCl_2$, $HgCl_2$, $MnCl_2 \cdot 4H_2O$, $CoCl_2$, $AlPO_4$, $Cr(NO_3)_3 \cdot 9H_2O$) were prepared as a stock solution (10 mM) in water. Proper volumes of metal stock solutions were added into the IQ

solutions in a quartz cuvette, and the mixture was equilibrated for 30 sec before measurement. The solid state fluorescence spectra were measured at room temperature by using a Fluoromax-4 spectrometer (Horiba Jobin Yvon, Kyoto, Japan). The measurement of optical properties for metal screening and metal competition test of the IQ compound were performed by a high throughput screening system using a multiplate reader, Mithras^2 LB 943 (Berthold Technologies, Bad Wildbad, Germany). Fluorescence quantum yields (Φ_F) of the IQ compounds in solution were measured with coumarin 153 in ethanol as a standard and the absolute fluorescence quantum yields (Φ_F) of solids were measured using a Fluoromax-4 spectrofluorometer (Horiba) with an integrating sphere assembly.

4.3.4 Time-resolved fluorescence measurement

Fluorescence decay of **IQ44** and **IQ-B27** were measured using a time-correlated single photon counting (TCSPC) technique using a DeltaTime on FluoroMax-4 spectrofluorometer (Horiba Jobin Yvon, Kyoto, Japan). DeltaDiode (DD-470L, Horiba) with ~90 ps pulse width and 100 MHz repetition rate was used as an excitation laser source at 464 nm. The time window size for fluorescence decay was 200 ns or 400 ns with 4096 time bins. The decays were accumulated 10000 counts at the peak. Analysis of the time domain fluorescence lifetime was performed by using a fluorescence decay analysis software (DAS6, Horiba). The fluorescence decays were reconvoluted with the instrumental response function (IRF) and fitted to the sum of exponential components.

4.3.5 Nanoaggregate characterization

Dynamic light scattering was employed to analyze the particle size distribution using a ELSZ-2000 (Otsuka, chiyoda, Japan). High-resolution transmission electron microscopy (HRTEM) images were obtained using a JEM-3010 electron microscope (JEOL, Tokyo, Japan) with an accelerating voltage of 300 kV. The samples were prepared by dropping the suspended solution of IQ on 400 mesh carbon grids with a copper support and dried over in a desiccator overnight.

4.3.6 Single crystal x-ray crystallographic data

Single Crystal X-ray Diffraction Studies. Single crystals of **IQ44**, **IQ-B27** and **IQ44**-Fe^{3+} with the dimension of 0.397 × 0.308 × 0.203 mm^3, 0.261 × 0.073 × 0.043 mm^3 and 0.404 × 0.169 × 0.059 mm^3, respectively, were grown by the vapor diffusion method using CH_2Cl_2 and *n*-hexane for **IQ44** and **IQ-B27**, and acetone and *n*-hexane for **IQ44**-Fe^{3+}. The suitable crystal was mounted on SuperNova, Dual, Cu at home/near, AtlasS2 diffractometer (Agilent, Santa Clara, CA, USA). The data collection of **IQ44** and **IQ-B27** was performed using a SuperNova dual source diffractometer operating with Cu-K_α radiation (λ= 1.542 mm^{-1}) at 101 K for **IQ44** and **IQ44**-Fe^{3+} and 99.9 K for **IQ-B27** respectively. Using Olex2 [1], the structure was solved by direct methods with the ShelXT [2] and refined by least squares minimization method using the ShelXL [3]. Supplementary crystallographic data of **IQ44**, **IQ-B27** and **IQ44**-Fe^{3+} in this paper can be obtained from the Cambridge Crystallographic Data Centre via www.ccdc.cam.ac.uk/data_request/cif. The deposition number of **IQ44**, **IQ-B27** and **IQ44**-Fe^{3+} are CCDC-1813169, CCDC-

1859855 and CCDC-1864199, respectively. All copies of the data can be downloaded upon request to CCDC, 12 Union Road, Cambridge CB2 1EZ, UK.

Crystal structure determination of IQ44. Crystal Data for $C_{21}H_{14}N_2O_2S$ (*M* =358.40 g/mol): monoclinic, space group $P2_1/n$ (no. 14), a = 14.6413(2) Å, b = 14.1292(2) Å, c = 15.8465(2) Å, β = 93.6190(10)°, V = 3271.63(8) Å^3, Z = 8, T = 101(2) K, μ(CuKα) = 1.912 mm^{-1}, *Dcalc* = 1.455 g/cm^3, 62202 reflections measured (7.974° ≤ 2Θ ≤ 147.79°), 6595 unique (R_{int} = 0.0255, R_{sigma} = 0.0097) which were used in all calculations. The final R_1 was 0.0378 ($I > 2\sigma(I)$) and wR_2 was 0.1035 (all data).

Crystal structure determination of IQ-B27. Crystal Data for $C_{19}H_{16}N_2O_2$ (*M* =304.34 g/mol): monoclinic, space group $P2_1/c$ (no. 14), a = 7.14450(10) Å, b = 11.17090(10) Å, c = 17.9465(2) Å, β = 91.6190(10)°, V = 1431.75(3) Å^3, Z = 4, T = 99.9(8) K, μ(CuKα) = 0.747 mm^{-1}, *Dcalc* = 1.412 g/cm^3, 14034 reflections measured (9.326° ≤ 2Θ ≤ 147.524°), 2856 unique (R_{int} = 0.0252, R_{sigma} = 0.0179) which were used in all calculations. The final R_1 was 0.0393 ($I > 2\sigma(I)$) and wR_2 was 0.1038 (all data).

Crystal structure determination of IQ44-Fe^{3+} Crystal Data for $C_{21}H_{14}Cl_4FeN_2O_2S$ (*M* =557.09 g/mol): triclinic, space group *P*-1 (no. 2), a = 6.8916(2) Å, b = 13.1016(5) Å, c = 15.9417(5) Å, α = 110.967(3)°, β = 102.254(3)°, γ = 95.340(3)°, V = 1290.74(8) Å^3, Z = 2, T = 101(2) K, μ(CuKα) = 9.418 mm^{-1}, *Dcalc* = 1.433 g/cm^3, 8703 reflections measured (6.16° ≤ 2Θ ≤ 134.14°), 4612 unique (R_{int} = 0.0294, R_{sigma} = 0.0331) which were used in all calculations. The final R_1 was 0.0367 ($I > 2\sigma(I)$) and wR_2 was 0.0948 (all data).

Table 2. Crystallographic data of **IQ44**, **IQ-B27** and **IQ44**-Fe^{3+}

	IQ44	**IQ-B27**	**IQ44-Fe^{3+}**
molecular formula	$C_{21}H_{14}N_2O_2S$	$C_{19}H_{16}N_2O_2$	$C_{21}H_{14}Cl_4FeN_2O_2S$
formula weight	358.40	304.34	557.09
crystal system	monoclinic	monoclinic	triclinic
space group	$P2_1/n$	$P2_1/c$	*P-1*
a [Å]	14.6413 (2)	7.14450(10)	6.8916(2)
b [Å]	14.1292 (2)	11.17090(10)	13.1016(5)
c [Å]	15.8465 (2)	17.9465(2)	15.9417(5)
α [°]	90	90	110.967(3)
β [°]	93.6190 (10)	91.6190(10)	102.254(3)
γ [°]	90	90	95.340(3)
V [$Å^3$]	3271.63(8)	1431.75(3)	1290.74(8)
Z	8	4	2
ρ_{calcd} [g cm^{-3}]	1.455	1.412	1.433
μ [mm^{-1}]	1.912	0.747	9.418
F(000)	1488.0	640.0	564.5
reflns measured	62202	14034	8703
unique reflns (R_{int})	6595 (0.0255)	2856 (0.0252)	4612 (0.0294)
R_1 [$I > 2\sigma(I)$]	0.0378	0.0393	0.0367
wR_2 (all data)	0.1035	0.1038	0.0948
Goodness of fit	1.049	1.064	1.039

V. REFERENCES

1. Ke, S. Y.; Qian, X. H.; Liu, F. Y.; Wang, N.; Yang, Q.; Li, Z., Novel 4H-1,3,4-oxadiazin-5(6H)-ones with hydrophobic and long alkyl chains: Design, synthesis, and bioactive diversity on inhibition of monoamine oxidase, chitin biosynthesis and tumor cell. *Eur. J. Med. Chem.* **2009,** *44* (5), 2113-2121.

2. Mazouz, F.; Gueddari, S.; Burstein, C.; Mansuy, D.; Milcent, R., 5-[4-(Benzyloxy)Phenyl]-1,3,4-Oxadiazol-2(3h)-One Derivatives and Related Analogs - New Reversible, Highly Potent, and Selective Monoamine-Oxidase Type-B Inhibitors. *J. Med. Chem.* **1993,** *36* (9), 1157-1167.

3. Mazouz, F.; Lebreton, L.; Milcent, R.; Burstein, C., Inhibition of Monoamine-Oxidase Type-a and Type-B by 2-Aryl-4h-1,3,4-Oxadiazin-5(6h)-One Derivatives. *European J. Med. Chem.* **1988,** *23* (5), 441-451.

4. Sweeney, Z. K.; Acharya, S.; Briggs, A.; Dunn, J. P.; Elworthy, T. R.; Fretland, J.; Giannetti, A. M.; Heilek, G.; Li, Y.; Kaiser, A. C.; Martin, M.; Saito, Y. D.; Smith, M.; Suh, J. M.; Swallow, S.; Wu, J.; Hang, J. Q.; Zhou, A. S.; Klumpp, K., Discovery of triazolinone non-nucleoside inhibitors of HIV reverse transcriptase. *Bioorg. Med. Chem. Lett.* **2008,** *18* (15), 4348-4351.

5. Hibi, S.; Ueno, K.; Nagato, S.; Kawano, K.; Ito, K.; Norimine, Y.; Takenaka, O.; Hanada, T.; Yonaga, M., Discovery of 2-(2-Oxo-1-phenyl-5-pyridin-2-yl-1,2-dihydropyridin-3-yl)benzonitrile (Perampanel): A Novel, Noncompetitive alpha-Amino-3-hydroxy-5-methyl-4-isoxazolepropanoic Acid (AMPA) Receptor Antagonist. *J. Med. Chem.* **2012,** *55* (23), 10584-10600.

6. Hameurlaine, A.; Abramov, M. A.; Dehaen, W., Formation of new heterocycles by intramolecular cyclization reactions of alkynethiolates with nitrogen nucleophiles. *Tetrahedron Lett.* **2002,** *43* (6), 1015-1017.

7. Kudelko, A.; Zielinski, W., Synthesis of novel 1,3,4-oxadiazin-5(6H)-ones and 2-hydroxymethyl-1,3,4-oxadiazoles. *Heterocycles* **2006,** *68* (11), 2269-2283.

8. Alam, M. M.; Lee, S. C.; Jung, Y.; Yun, H. J.; Min, H. Y.; Lee, H. J.; Pham, P. C.; Moon, J.; Kwon, D. I.; Lim, B.; Suh, Y. G.; Lee, J.; Lee, H. Y., Novel C6-substituted

1,3,4-oxadiazinones as potential anti-cancer agents. *Oncotarget* **2015,** *6* (38), 40598-40610.

9. Ruble, J. C.; Wakefield, B. D.; Kamilar, G. M.; Marotti, K. R.; Melchior, E.; Sweeney, M. T.; Zurenko, G. E.; Romero, D. L., Structure-activity relationships of bioisosteres of a carboxylic acid in a novel class of bacterial translation inhibitors. *Bioorg. Med. Chem. Lett.* **2007,** *17* (14), 4040-4043.

10. Zampieri, D.; Mamolo, M. G.; Laurini, E.; Fermeglia, M.; Posocco, P.; Pricl, S.; Banfi, E.; Scialino, G.; Vio, L., Antimycobacterial activity of new 3,5-disubstituted 1,3,4-oxadiazol-2(3H)-one derivatives. Molecular modeling investigations. *Bioorg. Med. Chem.* **2009,** *17* (13), 4693-4707.

11. Kiss, L. E.; Ferreira, H. S.; Beliaev, A.; Torrão, L.; Bonifácio, M. J.; Learmonth, D. A., Design, synthesis, and structure–activity relationships of 1,3,4-oxadiazol-2(3H)-ones as novel FAAH inhibitors. *Med. Chem. Commun.* **2011,** *2* (9), 889-894.

12. Patel, J. Z.; Parkkari, T.; Laitinen, T.; Kaczor, A. A.; Saario, S. M.; Savinainen, J. R.; Navia-Paldanius, D.; Cipriano, M.; Leppanen, J.; Koshevoy, I. O.; Poso, A.; Fowler, C. J.; Laitinen, J. T.; Nevalainen, T., Chiral 1,3,4-oxadiazol-2-ones as highly selective FAAH inhibitors. *J. Med. Chem.* **2013,** *56* (21), 8484-8496.

13. Patel, J. Z.; van Bruchem, J.; Laitinen, T.; Kaczor, A. A.; Navia-Paldanius, D.; Parkkari, T.; Savinainen, J. R.; Laitinen, J. T.; Nevalainen, T. J., Revisiting 1,3,4-Oxadiazol-2-ones: Utilization in the Development of ABHD6 Inhibitors. *Bioorg. Med. Chem.* **2015,** *23* (19), 6335-6345.

14. Sarma, B. K.; Liu, X.; Wu, H.; Gao, Y.; Kodadek, T., Solid phase synthesis of 1,3,4-oxadiazin-5 (6R)-one and 1,3,4-oxadiazol-2-one scaffolds from acyl hydrazides. *Org. Biomol. Chem.* **2015,** *13* (1), 59-63.

15. Romine, J. L.; Martin, S. W.; Meanwell, N. A.; Gribkoff, V. K.; Boissard, C. G.; Dworetzky, S. I.; Natale, J.; Moon, S.; Ortiz, A.; Yeleswaram, S.; Pajor, L.; Gao, Q.; Starrett, J. E., 3-[(5-chloro-2-hydroxyphenyl)methyl]-5-[4-(trifluoromethyl)phenyl]-1,3,4-oxadiazol-2(3H)-one, BMS-191011: Opener of large-conductance Ca2+-activated potassium (Maxi-K) channels, identification, solubility, and SAR. *J. Med. Chem.* **2007,** *50* (3), 528-542.

16. Chen, H.; Li, Z.; Han, Y., Synthesis and fungicidal activity against Rhizoctonia solani of 2-alkyl (Alkylthio)-5-pyrazolyl-1,3,4-oxadiazoles (Thiadiazoles). *J. Agric. Food Chem.* **2000,** *48* (11), 5312-5315.

17. Sarker, S. R.; Stone, D. M.; Evain, E. J.; Cooley, J. H.; Scott, B. L.; Willett, R. D., Reaction of Oxalyl and Malonyl Chloride with 1,1-Dimethyl-2-Substituted Hydrazides. *J. Heterocyclic. Chem.* **1994,** *31* (6), 1535-1539.

18. Mulvihill, M. J.; Nguyen, D. V.; MacDougall, B. S.; Weaver, D. G.; Mathis, W. D., A novel convenient synthesis of 1,3,4-oxadiazol-2-ones and -thiones from N-tert-butyldiacylhydrazines. *Synthesis-Stuttgart* **2001,** (13), 1965-1970.

19. Bancerz, M.; Georges, M. K., Verdazyl radicals as substrates for organic synthesis: a synthesis of 3-methyl-5-aryl-1,3,4-oxadiazolones. *J. Org. Chem.* **2011,** *76* (15), 6377-6382.

20. Le Quement, S. T.; Flagstad, T.; Mikkelsen, R. J. T.; Hansen, M. R.; Givskov, M. C.; Nielsen, T. E., Petasis Three-Component Coupling Reactions of Hydrazides for the Synthesis of Oxadiazolones and Oxazolidinones. *Org. Lett.* **2012,** *14* (2), 640-643.

21. Sugimoto, O.; Arakaki, T.; Kamio, H.; Tanji, K., The use of a Mitsunobu reagent for the formation of heterocycles: a simple method for the preparation of 3-alkyl-5-aryl-1,3,4-oxadiazol-2(3H)-ones from carboxylic acids. *Chem. Commun.* **2014,** *50* (55), 7314-7317.

22. Ji, F.; Li, X.; Guo, W.; Wu, W.; Jiang, H., Palladium-Catalyzed Oxidative O-H/N-H Carbonylation of Hydrazides: Access to Substituted 1,3,4-Oxadiazole-2(3H)-ones. *J. Org. Chem.* **2015,** *80* (11), 5713-5718.

23. Wang, Y.; Meng, X.; Yang, Y.; Zhang, L.; Guo, S.; Tang, D.; Li, Y.; Chen, B., Palladium-catalyzed oxidative carbonylation of hydrazides: synthesis of 1,3,4-oxadiazol-2(3H)-ones. *Chem. Commun.* **2015,** *51* (10), 1905-1907.

24. Patel, S. S.; Chandna, N.; Kumar, S.; Jain, N., I2 mediated synthesis of 5-substituted-3-methyl/benzyl-1,3,4-oxadiazol-2(3H)-ones via sequential condensation/oxidative cyclization and rearrangement. *Org. Biomol. Chem.* **2016,** *14* (24), 5683-5689.

25. Sheldon, R., *Green Chemistry in the Pharmaceutical Industry*. WILEY-VCH Verlag

GmbH & Co. KGaA: Weinheim, **2010**; p 1-18.

26. Gerfaud, T.; Wei, H. L.; Neuville, L.; Zhu, J. P., Unexpected C-C Bond Cleavage: Synthesis of 1,2,4-Oxadiazol-5-ones from Amidoximes with Pentafluorophenyl or Trifluoromethyl Anion Acting as Leaving Group. *Org. Lett.* **2011,** *13* (23), 6172-6175.

27. Allen, S. E.; Walvoord, R. R.; Padilla-Salinas, R.; Kozlowski, M. C., Aerobic copper-catalyzed organic reactions. *Chem. Rev.* **2013,** *113* (8), 6234-458.

28. Zhang, C.; Feng, P.; Jiao, N., Cu-catalyzed esterification reaction via aerobic oxygenation and C-C bond cleavage: an approach to alpha-ketoesters. *J. Am. Chem. Soc.* **2013,** *135* (40), 15257-15262.

29. Zhang, L.; Bi, X.; Guan, X.; Li, X.; Liu, Q.; Barry, B. D.; Liao, P., Chemoselective oxidative C(CO)-C(methyl) bond cleavage of methyl ketones to aldehydes catalyzed by CuI with molecular oxygen. *Angew. Chem., Int. Ed. Engl.* **2013,** *52* (43), 11303-11307.

30. Huang, X.; Li, X.; Zou, M.; Song, S.; Tang, C.; Yuan, Y.; Jiao, N., From ketones to esters by a Cu-catalyzed highly selective C(CO)-C(alkyl) bond cleavage: aerobic oxidation and oxygenation with air. *J. Am. Chem. Soc.* **2014,** *136* (42), 14858-14865.

31. Ma, R.; He, L. N.; Liu, A. H.; Song, Q. W., Cu(II)-catalyzed esterification reaction via aerobic oxidative cleavage of C(CO)-C(alkyl) bonds. *Chem. Commun.* **2016,** *52* (10), 2145-2148.

32. Tsang, A. S.; Kapat, A.; Schoenebeck, F., Factors That Control C-C Cleavage versus C-H Bond Hydroxylation in Copper-Catalyzed Oxidations of Ketones with O2. *J. Am. Chem. Soc.* **2016,** *138* (2), 518-526.

33. Xing, Q.; Lv, H.; Xia, C.; Li, F., Iron-catalyzed aerobic oxidative cleavage of the C-C sigma-bond using air as the oxidant: chemoselective synthesis of carbon chain-shortened aldehydes, ketones and 1,2-dicarbonyl compounds. *Chem. Commun.* **2016,** *52* (3), 489-492.

34. Liang, Y. F.; Jiao, N., Oxygenation via C-H/C-C Bond Activation with Molecular Oxygen. *Acc. Chem. Res.* **2017,** *50* (7), 1640-1653.

35. Liu, H.; Wang, M.; Li, H.; Luo, N.; Xu, S.; Wang, F., New protocol of copper-catalyzed oxidative C(CO)C bond cleavage of aryl and aliphatic ketones to organic acids using O2 as the terminal oxidant. *J. Catal.* **2017,** *346*, 170-179.

36. Lin, R. Y.; Chen, F.; Jiao, N., Metal-Free, NHPI Catalyzed Oxidative Cleavage of C-C Double Bond Using Molecular Oxygen as Oxidant. *Org. Lett.* **2012,** *14* (16), 4158-4161.

37. Liu, H.; Dong, C.; Zhang, Z.; Wu, P.; Jiang, X., Transition-metal-free aerobic oxidative cleavage of C-C bonds in alpha-hydroxy ketones and mechanistic insight to the reaction pathway. *Angew. Chem., Int. Ed. Engl.* **2012,** *51* (50), 12570-12574.

38. Tiwari, B.; Zhang, J.; Chi, Y. R., Facile access to chiral ketones through metal-free oxidative C-C bond cleavage of aldehydes by O2. *Angew. Chem., Int. Ed. Engl.* **2012,** *51* (8), 1911-1914.

39. Zhao, Q.; Li, H.; Wang, L., The direct amidation of alpha-diketones with amines via TBHP-promoted oxidative cleavage of C(sp(2))-C(sp(2)) bonds. *Org. Biomol. Chem.* **2013,** *11* (39), 6772-6779.

40. Liang, Y. F.; Jiao, N., Highly efficient C-H hydroxylation of carbonyl compounds with oxygen under mild conditions. *Angew. Chem., Int. Ed. Engl.* **2014,** *53* (2), 548-552.

41. Chaudhari, M. B.; Sutar, Y.; Malpathak, S.; Hazra, A.; Gnanaprakasam, B., Transition-Metal-Free C-H Hydroxylation of Carbonyl Compounds. *Org. Lett.* **2017,** *19* (13), 3628-3631.

42. Reddy, C. N.; Krishna, N. H.; Reddy, V. G.; Alarifi, A.; Kamal, A., Metal-Free Aerobic Oxidative C−C Bond Cleavage between the Carbonyl Carbon and the α-Carbon of α-Azido Ketones: A Novel Synthesis of N-Alkylated Benzamides. *Asian J. Org. Chem.* **2017,** *6* (10), 1498-1504.

43. Sheng, X.; Zhang, J.; Yang, H.; Jiang, G., Tunable Aerobic Oxidative Hydroxylation/Dehydrogenative Homocoupling of Pyrazol-5-ones under Transition-Metal-Free Conditions. *Org. Lett.* **2017,** *19* (10), 2618-2621.

44. Gao, Q.; Liu, S.; Wu, X.; Zhang, J.; Wu, A., Direct Annulation of Hydrazides to 1,3,4-Oxadiazoles via Oxidative C(CO)-C(Methyl) Bond Cleavage of Methyl Ketones. *Org.*

Lett. **2015,** *17* (12), 2960-2963.

45. Venkateswarlu, V.; Kumar, K. A. A.; Gupta, S.; Singh, D.; Vishwakarma, R. A.; Sawant, S. D., DMSO/I-2 mediated C-C bond cleavage of alpha-ketoaldehydes followed by C-O bond formation: a metal-free approach for one-pot esterification. *Org. Biomol. Chem.* **2015,** *13* (29), 7973-7978.

46. Allen, S. E.; Walvoord, R. R.; Padilla-Salinas, R.; Kozlowski, M. C., Aerobic Copper-Catalyzed Organic Reactions. *Chem. Rev.* **2013,** *113* (8), 6234-6458.

47. Liu, Z. Q.; Zhao, L. X.; Shang, X. J.; Cui, Z. L., Unexpected Copper-Catalyzed Aerobic Oxidative Cleavage of C(sp(3))-C(sp(3)) Bond of Glycol Ethers. *Org. Lett.* **2012,** *14* (12), 3218-3221.

48. De Risi, C.; Pollini, G. P.; Zanirato, V., Recent Developments in General Methodologies for the Synthesis of alpha-Ketoamides. *Chem. Rev.* **2016,** *116* (5), 3241-3305.

49. Liu, C.; Yang, Z.; Guo, S.; Zeng, Y.; Zhu, N.; Li, X.; Fang, Z.; Guo, K., Copper-TEMPO-catalyzed synthesis of alpha-ketoamides via tandem sp(3)C-H aerobic oxidation and amination of phenethyl alcohol derivatives. *Org. Biomol. Chem.* **2016,** *14* (36), 8570-8575.

50. Christoffers, J.; Werner, T.; Unger, S.; Frey, W., Preparation of acyloins by cerium-catalyzed, direct hydroxylation of beta-dicarbonyl compounds with molecular oxygen. *Eur. J. Org. Chem.* **2003,** (3), 425-431.

51. Chudasama, V.; Fitzmaurice, R. J.; Caddick, S., Hydroacylation of alpha,beta-unsaturated esters via aerobic C-H activation. *Nature Chem.* **2010,** *2* (7), 592-596.

52. Park., S. Study on synthesis and subsituent effects of 1,3,4-oxadiazin-5(6H)-one derivatives functionalized at the C6 position. Master of Science in Pharmacy. Thesis, Seoul National University, February, 2017.

53. Hansch, C.; Leo, A.; Taft, R. W., A Survey of Hammett Substituent Constants and Resonance and Field Parameters. *Chem. Rev.* **1991,** *91* (2), 165-195.

54. Anslyn, E. V.; Dougherty, D. A., *Modern Physical Organic Chemistry*. University

Science Books: Sausalito, CA, 2005; p 445.

55. Simon, G. M.; Niphakis, M. J.; Cravatt, B. F., Determining target engagement in living systems. *Nat. Chem. Biol* **2013,** *9* (4), 200-205.

56. Ziegler, S.; Pries, V.; Hedberg, C.; Waldmann, H., Target identification for small bioactive molecules: finding the needle in the haystack. *Angew. Chem. Int. Ed.* **2013,** *52* (10), 2744-2792.

57. Kambe, T.; Correia, B. E.; Niphakis, M. J.; Cravatt, B. F., Mapping the protein interaction landscape for fully functionalized small-molecule probes in human cells. *J. Am. Chem. Soc.* **2014,** *136* (30), 10777-10782.

58. Gao, J.; Mfuh, A.; Amako, Y.; Woo, C. M., Small Molecule Interactome Mapping by Photoaffinity Labeling Reveals Binding Site Hotspots for the NSAIDs. *J. Am. Chem. Soc.* **2018,** *140* (12), 4259-4268.

59. Schenone, M.; Dancik, V.; Wagner, B. K.; Clemons, P. A., Target identification and mechanism of action in chemical biology and drug discovery. *Nat. Chem. Biol* **2013,** *9* (4), 232-240.

60. Kotzybahibert, F.; Kapfer, I.; Goeldner, M., Recent Trends in Photoaffinity-Labeling. *Angew. Chem. Int. Ed.* **1995,** *34* (12), 1296-1312.

61. Hashimoto, M.; Hatanaka, Y., Recent Progress in Diazirine-Based Photoaffinity Labeling. *Eur. J. Org. Chem.* **2008,** (15), 2513-2523.

62. Das, J., Aliphatic diazirines as photoaffinity probes for proteins: recent developments. *Chem. Rev.* **2011,** *111* (8), 4405-4417.

63. Smith, E.; Collins, I., Photoaffinity labeling in target- and binding-site identification. *Future Med. Chem.* **2015,** *7* (2), 159-183.

64. Hamouda, A. K.; Jayakar, S. S.; Chiara, D. C.; Cohen, J. B., Photoaffinity Labeling of Nicotinic Receptors: Diversity of Drug Binding Sites! *J. Mol. Neurosci.* **2014,** *53* (3), 480-486.

65. Jack, T.; Leuenberger, M.; Ruepp, M. D.; Vernekar, S. K. V.; Thompson, A. J.; Braga-Lagache, S.; Heller, M.; Lochner, M., Mapping the Orthosteric Binding Site of the

Human 5-HT3 Receptor Using Photo-cross-linking Antagonists. *ACS Chem. Neurosci.* **2019**, *10* (1), 438-450.

66. Terstappen, G. C.; Schlupen, C.; Raggiaschi, R.; Gaviraghi, G., Target deconvolution strategies in drug discovery. *Nat. Rev. Drug Discovery* **2007,** *6* (11), 891-903.

67. Shi, H. B.; Zhang, C. J.; Chen, G. Y. J.; Yao, S. Q., Cell-Based Proteome Profiling of Potential Dasatinib Targets by Use of Affinity-Based Probes. *J. Am. Chem. Soc.* **2012,** *134* (6), 3001-3014.

68. Li, Z.; Hao, P.; Li, L.; Tan, C. Y.; Cheng, X.; Chen, G. Y.; Sze, S. K.; Shen, H. M.; Yao, S. Q., Design and synthesis of minimalist terminal alkyne-containing diazirine photo-crosslinkers and their incorporation into kinase inhibitors for cell- and tissue-based proteome profiling. *Angew. Chem. Int. Ed.* **2013,** *52* (33), 8551-856.

69. Horning, B. D.; Suciu, R. M.; Ghadiri, D. A.; Ulanovskaya, O. A.; Matthews, M. L.; Lum, K. M.; Backus, K. M.; Brown, S. J.; Rosen, H.; Cravatt, B. F., Chemical Proteomic Profiling of Human Methyltransferases. *J. Am. Chem. Soc.* **2016,** *138* (40), 13335-13343.

70. Kleiner, P.; Heydenreuter, W.; Stahl, M.; Korotkov, V. S.; Sieber, S. A., A Whole Proteome Inventory of Background Photocrosslinker Binding. *Angew. Chem. Int. Ed.* **2017,** *56* (5), 1396-1401.

71. Wang, D. Y.; Cao, Y.; Zheng, L. Y.; Chen, L. D.; Chen, X. F.; Hong, Z. Y.; Zhu, Z. Y.; Li, X.; Chai, Y. F., Target Identification of Kinase Inhibitor Alisertib (MLN8237) by Using DNA-Programmed Affinity Labeling. *Chemistry* **2017,** *23* (45), 10906-10914.

72. Li, R.; Pourpak, A.; Morris, S. W., Inhibition of the Insulin-like Growth Factor-1 Receptor (IGF1R) Tyrosine Kinase as a Novel Cancer Therapy Approach. *J. Med. Chem.* **2009,** *52* (16), 4981-5004.

73. Shin, D. H.; Lee, H. J.; Min, H. Y.; Choi, S. P.; Lee, M. S.; Lee, J. W.; Johnson, F. M.; Mehta, K.; Lippman, S. M.; Glisson, B. S.; Lee, H. Y., Combating resistance to anti-IGFR antibody by targeting the integrin beta3-Src pathway. *J. Natl. Cancer Inst.* **2013,** *105* (20), 1558-1570.

74. Peterson, J. E.; Kulik, G.; Jelinek, T.; Reuter, C. W.; Shannon, J. A.; Weber, M. J., Src

phosphorylates the insulin-like growth factor type I receptor on the autophosphorylation sites. Requirement for transformation by src. *J. Bio.l Chem.* **1996,** *271* (49), 31562-31571.

75. Yeatman, T. J., A renaissance for SRC. *Nat. Rev. Cancer* **2004,** *4* (6), 470-480.

76. Mackinnon, A. L.; Taunton, J., Target Identification by Diazirine Photo-Cross-linking and Click Chemistry. *Curr. Protoc. Chem. Biol.* **2009,** *1*, 55-73.

77. Hill, J. R.; Robertson, A. A. B., Fishing for Drug Targets: A Focus on Diazirine Photoaffinity Probe Synthesis. *J. Med. Chem.* **2018,** *61* (16), 6945-6963.

78. Rostovtsev, V. V.; Green, L. G.; Fokin, V. V.; Sharpless, K. B., A stepwise huisgen cycloaddition process: copper(I)-catalyzed regioselective "ligation" of azides and terminal alkynes. *Angew. Chem. Int. Ed.* **2002,** *41* (14), 2596-9.

79. Best, M. D., Click chemistry and bioorthogonal reactions: unprecedented selectivity in the labeling of biological molecules. *Biochemistry* **2009,** *48* (28), 6571-6584.

80. Wu, J.; Li, W.; Craddock, B. P.; Foreman, K. W.; Mulvihill, M. J.; Ji, Q. S.; Miller, W. T.; Hubbard, S. R., Small-molecule inhibition and activation-loop trans-phosphorylation of the IGF1 receptor. *EMBO J.* **2008,** *27* (14), 1985-1994.

81. Brosse, N.; Pinto, M. F.; Jamart-Gregoire, B., Preparation of multiply protected alkylhydrazine derivatives by mitsunobu and PTC approaches. *Eur. J. Org. Chem.* **2003,** (24), 4757-4764.

82. Shigdel, U. K.; Zhang, J. L.; He, C., Diazirine-based DNA photo-cross-linking probes for the study of protein-DNA interactions. *Angew. Chem. Int. Ed.* **2008,** *47* (1), 90-93.

83. Wright, A. T.; Song, J. D.; Cravatt, B. F., A Suite of Activity-Based Probes for Human Cytochrome P450 Enzymes. *J. Am. Chem. Soc.* **2009,** *131* (30), 10692-10700.

84. Lim, B.; Park, S.; Park, J. H.; Gam, J.; Kim, S.; Yang, J. W.; Lee, J., A metal-free and mild approach to 1,3,4-oxadiazol-2(3H)-ones via oxidative C-C bond cleavage using molecular oxygen. *Org. Biomol. Chem.* **2018,** *16* (12), 2105-2113.

85. Cisneros, J. A.; Bjorklund, E.; Gonzalez-Gil, I.; Hu, Y. L.; Canales, A.; Medrano, F. J.; Romero, A.; Ortega-Gutierrez, S.; Fowler, C. J.; Lopez-Rodriguez, M. L.,

Structure-Activity Relationship of a New Series of Reversible Dual Monoacylglycerol Lipase/Fatty Acid Amide Hydrolase Inhibitors. *J. Med. Chem.* **2012,** *55* (2), 824-836.

86. Preston, G. W.; Wilson, A. J., Photo-induced covalent cross-linking for the analysis of biomolecular interactions. *Chem. Soc. Rev.* **2013,** *42* (8), 3289-3301.

87. Koide, Y.; Urano, Y.; Hanaoka, K.; Terai, T.; Nagano, T., Evolution of Group 14 Rhodamines as Platforms for Near-Infrared Fluorescence Probes Utilizing Photoinduced Electron Transfer. *Acs. Chem. Biol.* **2011,** *6* (6), 600-608.

88. Yuan, L.; Lin, W. Y.; Zheng, K. B.; He, L. W.; Huang, W. M., Far-red to near infrared analyte-responsive fluorescent probes based on organic fluorophore platforms for fluorescence imaging. *Chem. Soc. Rev.* **2013,** *42* (2), 622-661.

89. Kowada, T.; Maeda, H.; Kikuchi, K., BODIPY-based probes for the fluorescence imaging of biomolecules in living cells. *Chem. Soc. Rev.* **2015,** *44* (14), 4953-4972.

90. Hong, S. C.; Murale, D. P.; Lee, M.; Lee, S. M.; Park, J. S.; Lee, J. S., Bulk Aggregation Based Fluorescence Turn-On Sensors for Selective Detection of Progesterone in Aqueous Solution. *Angew. Chem. Int. Ed.* **2017,** *56* (46), 14642-14647.

91. Lu, X. D.; Hou, M. R.; Xia, Q.; Yan, C. G.; Xu, Y. K.; Liu, R. Y., Mitochondrial targeted fluorescent probe with AIE characteristics for bioimaging. *Mat. Sci. Eng. C,* **2017,** *77*, 129-135.

92. Xu, W.; He, L.; Xia, Q.; Jia, C.; Geng, L.; Yang, M.; Xu, Z.; Chen, P.; Cheng, Y.; Zhao, J.; Wang, H.; Chen, H.; Zhang, Y.; Gong, S.; Liu, R., A far-red-emissive AIE active fluorescent probe with large stokes shift for detection of inflammatory bowel disease in vivo. *J. Mater.. Chem. B,* **2018,** *6* (5), 809-815.

93. Yapici, N. B.; Bi, Y.; Li, P.; Chen, X.; Yan, X.; Mandalapu, S. R.; Faucett, M.; Jockusch, S.; Ju, J.; Gibson, K. M.; Pavan, W. J.; Bi, L., Highly stable and sensitive fluorescent probes (LysoProbes) for lysosomal labeling and tracking. *Sci. Rep.* **2015,** *5*, 8576.

94. Leung, C. W.; Wang, Z.; Zhao, E.; Hong, Y.; Chen, S.; Kwok, R. T.; Leung, A. C.; Wen, R.; Li, B.; Lam, J. W.; Tang, B. Z., A Lysosome-Targeting AIEgen for Autophagy Visualization. *Adv. Healthc. Mate.r* **2016,** *5* (4), 427-431.

95. Gui, C.; Zhao, E. G.; Kwok, R. T. K.; Leung, A. C. S.; Lam, J. W. Y.; Jiang, M. J.; Deng, H. Q.; Cai, Y. J.; Zhang, W. J.; Su, H. F.; Tang, B. Z., AIE-active theranostic system: selective staining and killing of cancer cells. *Chem. Sci.* **2017,** *8* (3), 1822-1830.

96. Long, L. L.; Huang, M. Y.; Wang, N.; Wu, Y. J.; Wang, K.; Gong, A. H.; Zhang, Z. J.; Sessler, J. L., A Mitochondria-Specific Fluorescent Probe for Visualizing Endogenous Hydrogen Cyanide Fluctuations in Neurons. *J. Am. Chem. Soc.* **2018,** *140* (5), 1870-1875.

97. Carter, K. P.; Young, A. M.; Palmer, A. E., Fluorescent Sensors for Measuring Metal Ions in Living Systems. *Chem. Rev.* **2014,** *114* (8), 4564-4601.

98. Abbate, V.; Reelfs, O.; Hider, R. C.; Pourzand, C., Design of novel fluorescent mitochondria-targeted peptides with iron-selective sensing activity. *Biochem. J.* **2015,** *469* (3), 357-366.

99. Zecca, L.; Youdim, M. B.; Riederer, P.; Connor, J. R.; Crichton, R. R., Iron, brain ageing and neurodegenerative disorders. *Nat. Rev. Neurosc.i* **2004,** *5* (11), 863-873.

100. Torti, S. V.; Torti, F. M., Iron and cancer: more ore to be mined. *Nat. Rev. Cancer.* **2013,** *13* (5), 342-355.

101. Ward, R.; Zucca, F. A.; Duyn, J. H.; Crichton, R. R.; Zecca, L., The role of iron in brain ageing and neurodegenerative disorders. *Lancet. Neurol.* **2014,** *13* (10), 1045-1060.

102. Martin-Bastida, A.; Ward, R. J.; Newbould, R.; Piccini, P.; Sharp, D.; Kabba, C.; Patel, M. C.; Spino, M.; Connelly, J.; Tricta, F.; Crichton, R. R.; Dexter, D. T., Brain iron chelation by deferiprone in a phase 2 randomised double-blinded placebo controlled clinical trial in Parkinson's disease. *Sci. Rep.* **2017,** *7* (1), 1398.

103. Dixon, S. J.; Stockwell, B. R., The role of iron and reactive oxygen species in cell death. *Nat. Chem. Biol.* **2014,** *10* (1), 9-17.

104. Parzych, K. R.; Klionsky, D. J., An Overview of Autophagy: Morphology, Mechanism, and Regulation. *Antioxid. Redox. Sign.* **2014,** *20* (3), 460-473.

105. Xie, Y.; Hou, W.; Song, X.; Yu, Y.; Huang, J.; Sun, X.; Kang, R.; Tang, D., Ferroptosis: process and function. *Cell. Death. Diffe.r* **2016,** *23* (3), 369-379.

106. Fakih, S.; Podinovskaia, M.; Kong, X.; Collins, H. L.; Schaible, U. E.; Hider, R. C., Targeting the lysosome: Fluorescent iron(III) chelators to selectively monitor endosomal/lysosomal labile iron pools. *J. Med. Chem.* **2008,** *51* (15), 4539-4552.

107. Kurz, T.; Terman, A.; Gustafsson, B.; Brunk, U. T., Lysosomes in iron metabolism, ageing and apoptosis. *Histochem. Cell. Biol.* **2008,** *129* (4), 389-406.

108. Sahoo, S. K.; Sharma, D.; Bera, R. K.; Crisponi, G.; Callan, J. F., Iron(III) selective molecular and supramolecular fluorescent probes. *Chem. Soc. Rev.* **2012,** *41* (21), 7195-7227.

109. Ma, Y.; Abbate, V.; Hider, R. C., Iron-sensitive fluorescent probes: monitoring intracellular iron pools. *Metallomics* **2015,** *7* (2), 212-222.

110. Fryknas, M.; Zhang, X.; Bremberg, U.; Senkowski, W.; Olofsson, M. H.; Brandt, P.; Persson, I.; D'Arcy, P.; Gullbo, J.; Nygren, P.; Schughart, L. K.; Linder, S.; Larsson, R., Iron chelators target both proliferating and quiescent cancer cells. *Sci. Rep.* **2016,** *6*, 38343.

111. Kazan, H. H.; Urfali-Mamatoglu, C.; Gunduz, U., Iron metabolism and drug resistance in cancer. *Biometals* **2017,** *30* (5), 629-641.

112. Abbate, V.; Reelfs, O.; Kong, X.; Pourzand, C.; Hider, R. C., Dual selective iron chelating probes with a potential to monitor mitochondrial labile iron pools. *Chem. Commun.* **2016,** *52* (4), 784-787.

113. Biswas, S.; Sharma, V.; Kumar, P.; Koner, A. L., Selective sensing of lysosomal iron(III) via three-component fluorescence-based strategy in living cells. *Sens. Actuators, B* **2018,** *260*, 460-464.

114. Zhang, X. Y.; Wang, K.; Liu, M. Y.; Zhang, X. Q.; Tao, L.; Chen, Y. W.; Wei, Y., Polymeric AIE-based nanoprobes for biomedical applications: recent advances and perspectives. *Nanoscale* **2015,** *7* (27), 11486-11508.

115. Gao, M.; Tang, B. Z., Fluorescent Sensors Based on Aggregation-Induced Emission:

Recent Advances and Perspectives. *ACS. Sens.* **2017,** *2* (10), 1382-1399.

116. Long, Z.; Mao, L. C.; Liu, M. Y.; Wan, Q.; Wan, Y. Q.; Zhang, X. Y.; Wei, Y., Marrying multicomponent reactions and aggregation-induced emission (AIE): new directions for fluorescent nanoprobes. *Polym. Chem.* **2017,** *8* (37), 5644-5654.

117. Mao, L. C.; Liu, Y. Z.; Yang, S. J.; Li, Y. X.; Zhang, X. Y.; Wei, Y., Recent advances and progress of fluorescent bio-/chemosensors based on aggregation-induced emission molecules. *Dyes Pigm.* **2019,** *162*, 611-623.

118. An, B. K.; Kwon, S. K.; Jung, S. D.; Park, S. Y., Enhanced emission and its switching in fluorescent organic nanoparticles. *J. Am. Chem. Soc.* **2002,** *124* (48), 14410-14415.

119. Kwok, R. T.; Leung, C. W.; Lam, J. W.; Tang, B. Z., Biosensing by luminogens with aggregation-induced emission characteristics. *Chem Soc Rev* **2015,** *44* (13), 4228-38.

120. Mei, J.; Leung, N. L. C.; Kwok, R. T. K.; Lam, J. W. Y.; Tang, B. Z., Aggregation-Induced Emission: Together We Shine, United We Soar! *Chem. Rev.* **2015,** *115* (21), 11718-11940.

121. Shi, J. Q.; Suarez, L. E. A.; Yoon, S. J.; Varghese, S.; Serpa, C.; Park, S. Y.; Luer, L.; Roca-Sanjuan, D.; Milian-Medina, B.; Gierschner, J., Solid State Luminescence Enhancement in a pi-Conjugated Materials: Unraveling the Mechanism beyond the Framework of AIE/AIEE. *J. Phys. Chem. C* **2017,** *121* (41), 23166-23183.

122. Li, Q. Q.; Li, Z., The Strong Light-Emission Materials in the Aggregated State: What Happens from a Single Molecule to the Collective Group. *Ad.v Sci.* **2017,** *4* (7), 1600484.

123. Lou, X. D.; Zhang, M. S.; Zhao, Z. J.; Min, X. H.; Hakeem, A.; Huang, F. J.; Gao, P. C.; Xia, F.; Tang, B. Z., A photostable AIE fluorogen for lysosome-targetable imaging of living cells. *J. Mater. Chem. B* **2016,** *4* (32), 5412-5417.

124. Shyamal, M.; Mazumdar, P.; Maity, S.; Sahoo, G. P.; Salgado-Moran, G.; Misra, A., Pyrene Scaffold as Real-Time Fluorescent Turn-on Chemosensor for Selective Detection of Trace-Level Al(III) and Its Aggregation-Induced Emission Enhancement. *J. Phy.Chem. A* **2016,** *120* (2), 210-220.

125. Guo, J.; Hu, S.; Luo, W.; Hu, R.; Qin, A.; Zhao, Z.; Tang, B. Z., A novel aggregation-induced emission platform from 2,3-diphenylbenzo[b]thiophene S,S-dioxide. *Chem. Commun.* **2017,** *53* (9), 1463-1466.

126. Raghuvanshi, A.; Jha, A. K.; Sharma, A.; Umar, S.; Mishra, S.; Kant, R.; Goel, A., A Nonarchetypal 5,6-Dihydro-2H-pyrano[3,2-g]indolizine-Based Solution-Solid Dual Emissive AIEgen with Multicolor Tunability. *Chemistry* **2017,** *23* (19), 4527-4531.

127. Bhalla, V.; Gupta, A.; Kumar, M., A pentacenequinone derivative with aggregation-induced emission enhancement characteristics for the picogram detection of Fe(3+) ions in mixed aqueous media. *Dalton Trans.* **2013,** *42* (13), 4464-4469.

128. Ye, J.-H.; Liu, J.; Wang, Z.; Bai, Y.; Zhang, W.; He, W., A new Fe3+ fluorescent chemosensor based on aggregation-induced emission. *Tetrahedron Lett.* **2014,** *55* (27), 3688-3692.

129. Yang, X.; Chen, X.; Lu, X.; Yan, C.; Xu, Y.; Hang, X.; Qu, J.; Liu, R., A highly selective and sensitive fluorescent chemosensor for detection of CN−, SO32− and Fe3+ based on aggregation-induced emission. *J. Mater. Chem. C* **2016,** *4* (2), 383-390.

130. Zhang, H.; Zhang, G.; Xu, J.; Wen, Y.; Lu, B.; Zhang, J.; Ding, W., Novel highly selective fluorescent sensor based on electrosynthesized poly(9-fluorenecarboxylic acid) for efficient and practical detection of iron(III) and its agricultural application. *Sens. Actuators, B* **2016,** *230*, 123-129.

131. Wang, X.; Wang, H.; Feng, S., A novel thiophene functionalized silicon-cored compounds: Aggregation-induced emission enhancement and aqueous fluorogenic Fe 3+ probes in bovine serum albumin. *Sens. Actuators, B* **2017,** *241*, 65-72.

132. Azadbakht, R.; Hakimi, M.; Khanabadi, J., Fluorescent organic nanoparticles with enhanced fluorescence by self-aggregation and their application for detection of Fe3+ ions. *New J. Chem.* **2018,** *42* (8), 5929-5936.

133. Chen, X.; Shen, X. Y.; Guan, E.; Liu, Y.; Qin, A.; Sun, J. Z.; Tang, B. Z., A pyridinyl-functionalized tetraphenylethylene fluorogen for specific sensing of trivalent cations. *Chem. Commun.* **2013,** *49* (15), 1503-1505.

134. Han, C. P.; Huang, T. H.; Liu, Q.; Xu, H. T.; Zhuang, Y. P.; Li, J. J.; Hu, J. F.; Wang,

A. M.; Xu, K., Design and synthesis of a highly sensitive "Turn-On" fluorescent organic nanoprobe for iron(III) detection and imaging. *J. Mater. Chem. C* **2014,** *2* (43), 9077-9082.

135. Feng, X.; Li, Y.; He, X. W.; Liu, H. X.; Zhao, Z.; Kwok, R. T. K.; Elsegood, M. R. J.; Lam, J. W. Y.; Tang, B. Z., A Substitution-Dependent Light-Up Fluorescence Probe for Selectively Detecting Fe3+ Ions and Its Cell Imaging Application. *Adv. Funct. Mater.* **2018,** *28* (35), 1802833.

136. Li, K.; Liu, B., Polymer-encapsulated organic nanoparticles for fluorescence and photoacoustic imaging. *Chem. Soc. Rev.* **2014,** *43* (18), 6570-6597.

137. Zhang, X.; Zhang, X.; Yang, B.; Liu, M.; Liu, W.; Chen, Y.; Wei, Y., Fabrication of aggregation induced emission dye-based fluorescent organic nanoparticles via emulsion polymerization and their cell imaging applications. *Polym. Chem.* **2014,** *5* (2), 399-404.

138. Li, F. Y.; Lu, J. X.; Kong, X. Q.; Hyeon, T.; Ling, D. S., Dynamic Nanoparticle Assemblies for Biomedical Applications. *Adv. Mater.* **2017,** *29* (14). 1605897.

139. Long, Z.; Liu, M.; Jiang, R.; Wan, Q.; Mao, L.; Wan, Y.; Deng, F.; Zhang, X.; Wei, Y., Preparation of water soluble and biocompatible AIE-active fluorescent organic nanoparticles via multicomponent reaction and their biological imaging capability. *Chem. Eng. J.* **2017,** *308*, 527-534.

140. Wan, Q.; Huang, Q.; Liu, M.; Xu, D.; Huang, H.; Zhang, X.; Wei, Y., Aggregation-induced emission active luminescent polymeric nanoparticles: Non-covalent fabrication methodologies and biomedical applications. *Appl. Mater. Today* **2017,** *9*, 145-160.

141. Chen, J.; Liu, M.; Huang, Q.; Huang, L.; Huang, H.; Deng, F.; Wen, Y.; Tian, J.; Zhang, X.; Wei, Y., Facile preparation of fluorescent nanodiamond-based polymer composites through a metal-free photo-initiated RAFT process and their cellular imaging. *Chem. Eng. J.* **2018,** *337*, 82-90.

142. Huang, H.; Liu, M.; Jiang, R.; Chen, J.; Mao, L.; Wen, Y.; Tian, J.; Zhou, N.; Zhang, X.; Wei, Y., Facile modification of nanodiamonds with hyperbranched polymers based on supramolecular chemistry and their potential for drug delivery. *J. Colloid Interface*

Sci. **2018,** *513*, 198-204.

143. Huang, H.; Liu, M.; Wan, Q.; Jiang, R.; Xu, D.; Huang, Q.; Wen, Y.; Deng, F.; Zhang, X.; Wei, Y., Facile fabrication of luminescent hyaluronic acid with aggregation-induced emission through formation of dynamic bonds and their theranostic applications. *Mater. Sci. Eng. C* **2018,** *91*, 201-207.

144. Jiang, R.; Liu, M.; Huang, H.; Mao, L.; Huang, Q.; Wen, Y.; Cao, Q. Y.; Tian, J.; Zhang, X.; Wei, Y., Facile fabrication of organic dyed polymer nanoparticles with aggregation-induced emission using an ultrasound-assisted multicomponent reaction and their biological imaging. *J. Colloid Interface Sci.* **2018,** *519*, 137-144.

145. Zhang, X.; Zhang, X.; Yang, B.; Liu, M.; Liu, W.; Chen, Y.; Wei, Y., Polymerizable aggregation-induced emission dye-based fluorescent nanoparticles for cell imaging applications. *Polym. Chem.* **2014,** *5* (2), 356-360.

146. Long, Z.; Liu, M.; Wang, K.; Deng, F.; Xu, D.; Liu, L.; Wan, Y.; Zhang, X.; Wei, Y., Facile synthesis of AIE-active amphiphilic polymers: Self-assembly and biological imaging applications. *Mater. Sci. Eng. C* **2016,** *66*, 215-220.

147. Cheung, S.; O'Shea, D. F., Directed self-assembly of fluorescence responsive nanoparticles and their use for real-time surface and cellular imaging. *Nat Commun* **2017,** *8*, 1885.

148. Jiang, R.; Liu, M.; Chen, T.; Huang, H.; Huang, Q.; Tian, J.; Wen, Y.; Cao, Q.-y.; Zhang, X.; Wei, Y., Facile construction and biological imaging of cross-linked fluorescent organic nanoparticles with aggregation-induced emission feature through a catalyst-free azide-alkyne click reaction. *Dyes Pigm.* **2018,** *148*, 52-60.

149. Huang, L.; Yang, S.; Chen, J.; Tian, J.; Huang, Q.; Huang, H.; Wen, Y.; Deng, F.; Zhang, X.; Wei, Y., A facile surface modification strategy for fabrication of fluorescent silica nanoparticles with the aggregation-induced emission dye through surface-initiated cationic ring opening polymerization. *Mater. Sci. Eng. C* **2019,** *94*, 270-278.

150. Singh, A.; Sinha, S.; Kaur, R.; Kaur, N.; Singh, N., Rhodamine based organic nanoparticles for sensing of Fe3+ with high selectivity in aqueous medium: Application to iron supplement analysis. *Sens. Actuators, B* **2014,** *204*, 617-621.

151. Yang, Y.; Wang, X. Y.; Cui, Q. L.; Cao, Q.; Li, L. D., Self-Assembly of Fluorescent Organic Nanoparticles for Iron(III) Sensing and Cellular Imaging. *Acs. App.l Mater. Inter.* **2016,** *8* (11), 7440-7448.

152. Park, S.; Kwon, D. I.; Lee, J.; Kim, I., When Indolizine Meets Quinoline: Diversity-Oriented Synthesis of New Polyheterocycles and Their Optical Properties. *Acs. Comb. Sci.* **2015,** *17* (8), 459-469.

153. Kwon, S.; Lee, Y.; Jung, Y.; Kim, J. H.; Baek, B.; Lim, B.; Lee, J.; Kim, I.; Lee, J., Mitochondria-targeting indolizino[3,2-c]quinolines as novel class of photosensitizers for photodynamic anticancer activity. *Eur. J. Med. Chem.* **2018,** *148*, 116-127.

154. M. J. Frisch, G. W. T., H. B. Schlegel, G. E. Scuseria, M. A. Robb, J. R. Cheeseman, G. Scalmani, V. Barone, B. Mennucci, G. A. Petersson, H. Nakatsuji, M. Caricato, X. Li, H. P. Hratchian, A. F. Izmaylov, J. Bloino, G. Zheng, J. L. Sonnenberg, M. Hada, M. Ehara, K. Toyota, R. Fukuda, J. Hasegawa, M. Ishida, T. Nakajima, Y. Honda, O. Kitao, H. Nakai, T. Vreven, J. A. Montgomery, Jr., J. E. Peralta, F. Ogliaro, M. Bearpark, J. J. Heyd, E. Brothers, K. N. Kudin, V. N. Staroverov, R. Kobayashi, J. Normand, K. Raghavachari, A. Rendell, J. C. Burant, S. S. Iyengar, J. Tomasi, M. Cossi, N. Rega, J. M. Millam, M. Klene, J. E. Knox, J. B. Cross, V. Bakken, C. Adamo, J. Jaramillo, R. Gomperts, R. E. Stratmann, O. Yazyev, A. J. Austin, R. Cammi, C. Pomelli, J. W. Ochterski, R. L. Martin, K. Morokuma, V. G. Zakrzewski, G. A. Voth, P. Salvador, J. J. Dannenberg, S. Dapprich, A. D. Daniels, Ö. Farkas, J. B. Foresman, J. V. Ortiz, J. Cioslowski, and D. J. Fox *Gaussian 09*, Wallingford, CT, 2009.

VI. APPENDIX

^{1}H-NMR of compound **3a** (500 MHz, $CDCl_3$)

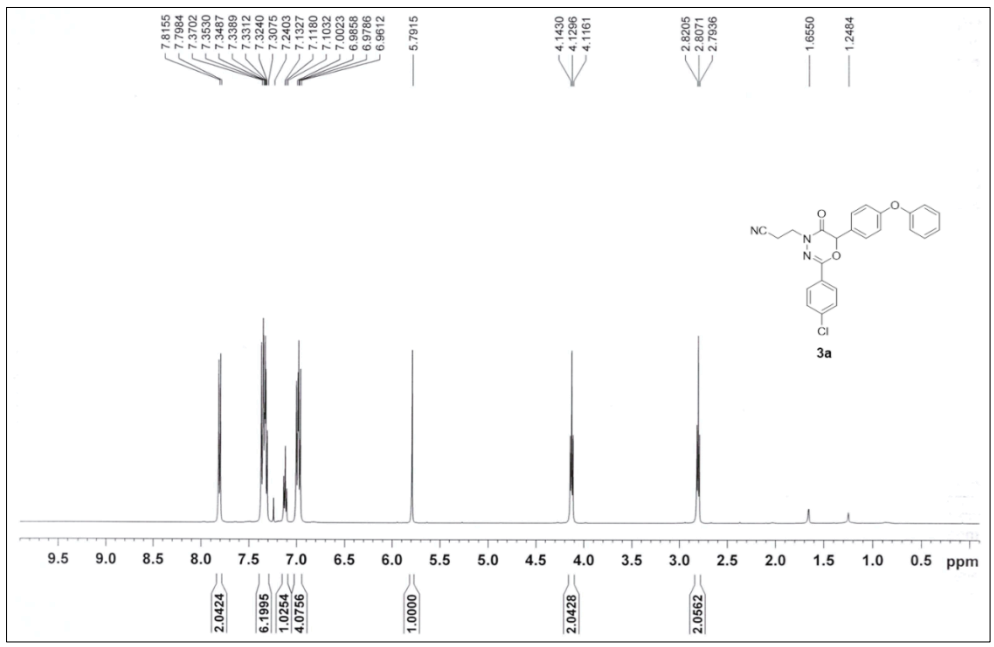

^{13}C-NMR of compound **3a** (125 MHz, $CDCl_3$)

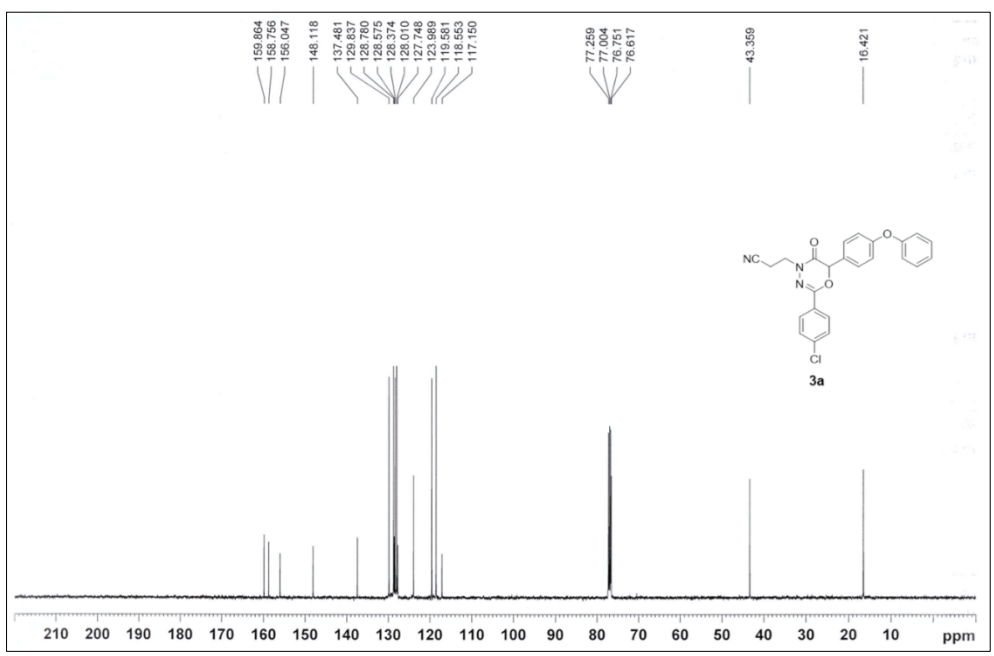

^{1}H-NMR of compound **3b** (500 MHz, $CDCl_3$)

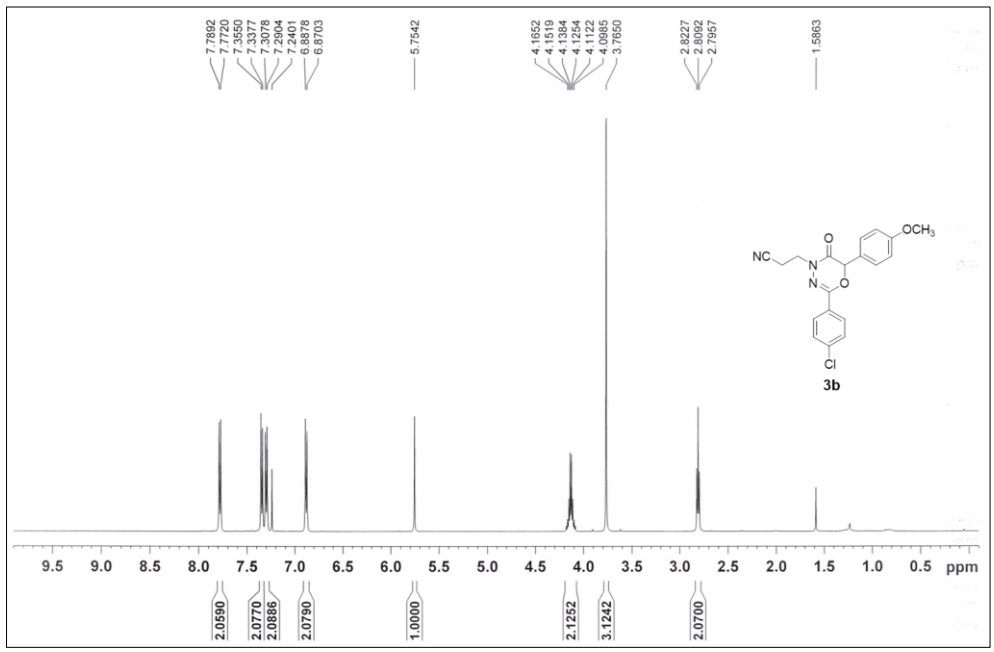

^{13}C-NMR of compound **3b** (125 MHz, $CDCl_3$)

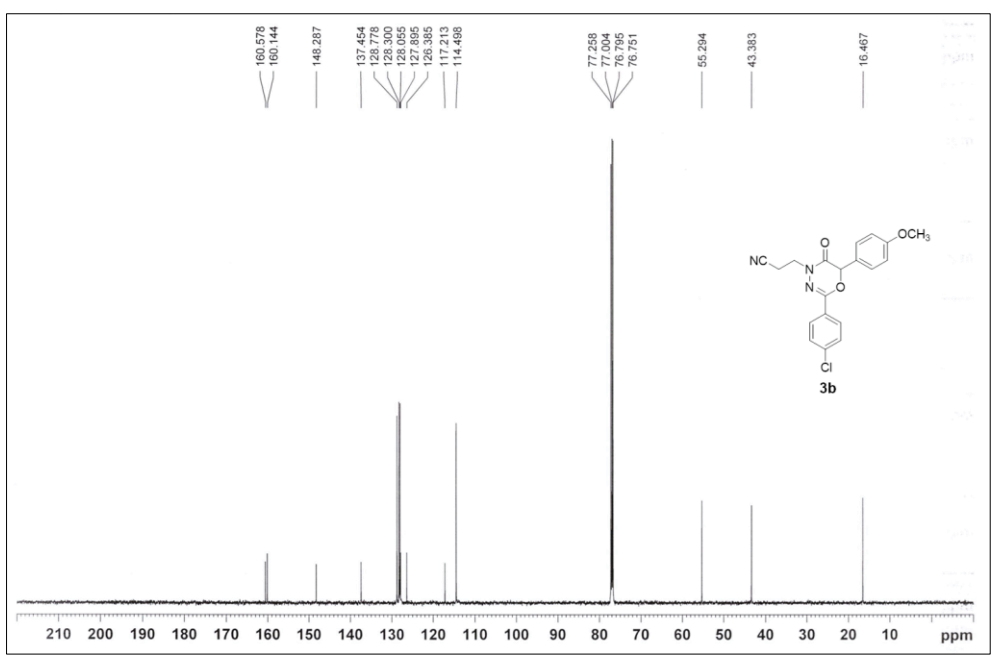

^{1}H-NMR of compound **3c** (500 MHz, $CDCl_3$)

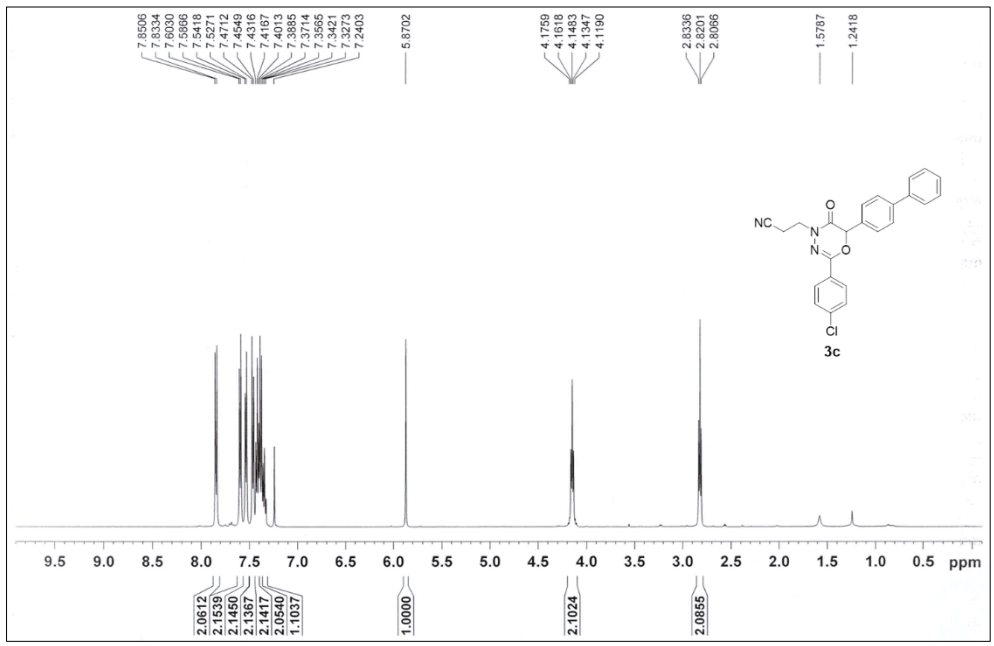

^{13}C-NMR of compound **3c** (125 MHz, $CDCl_3$)

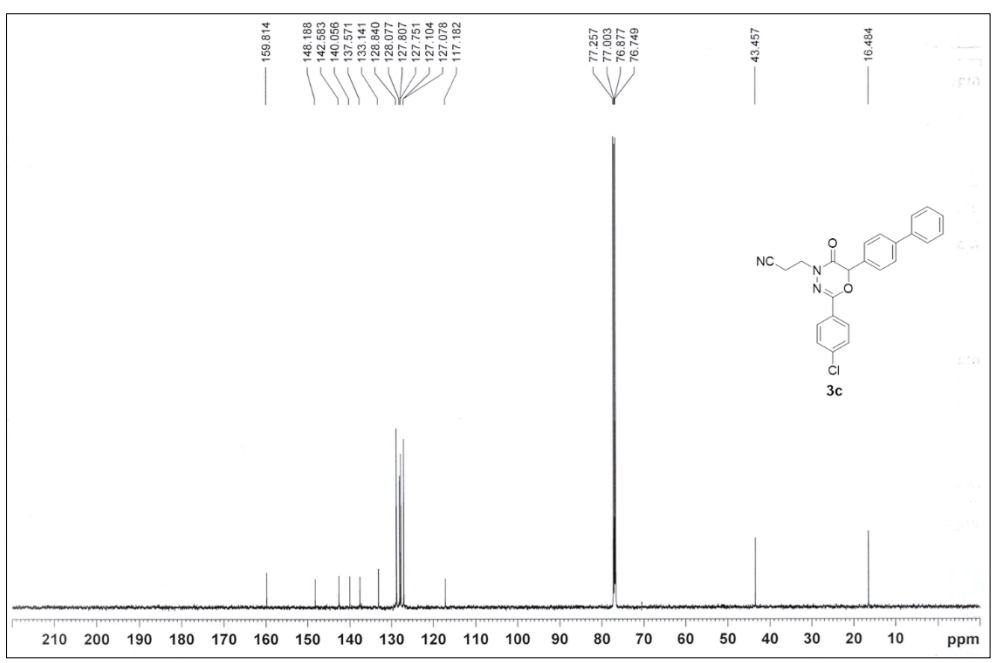

^{1}H-NMR of compound **3d** (500 MHz, $CDCl_3$)

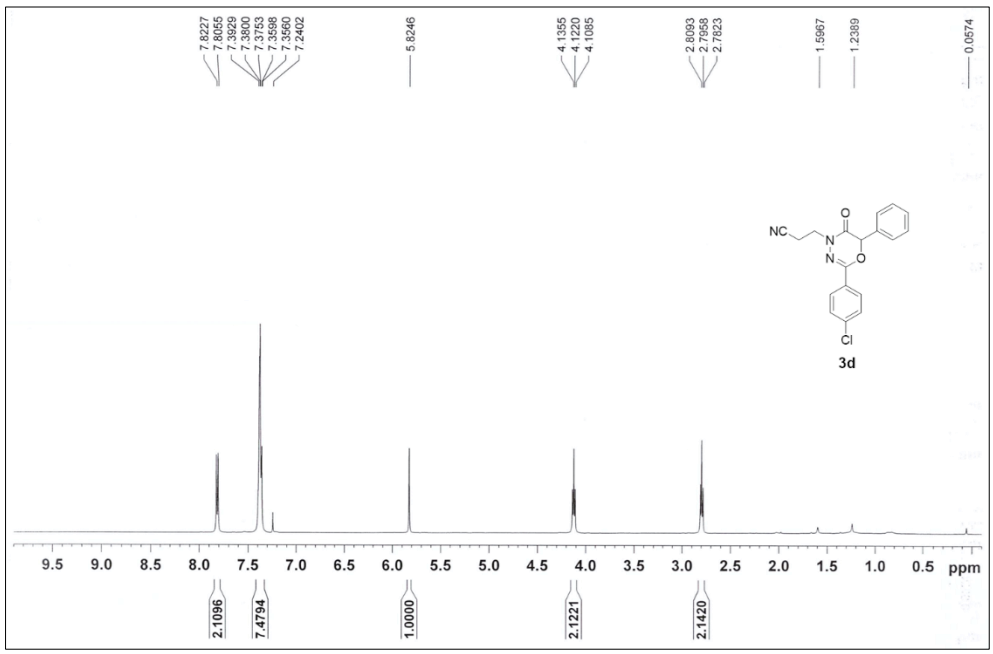

^{13}C-NMR of compound **3d** (125 MHz, $CDCl_3$)

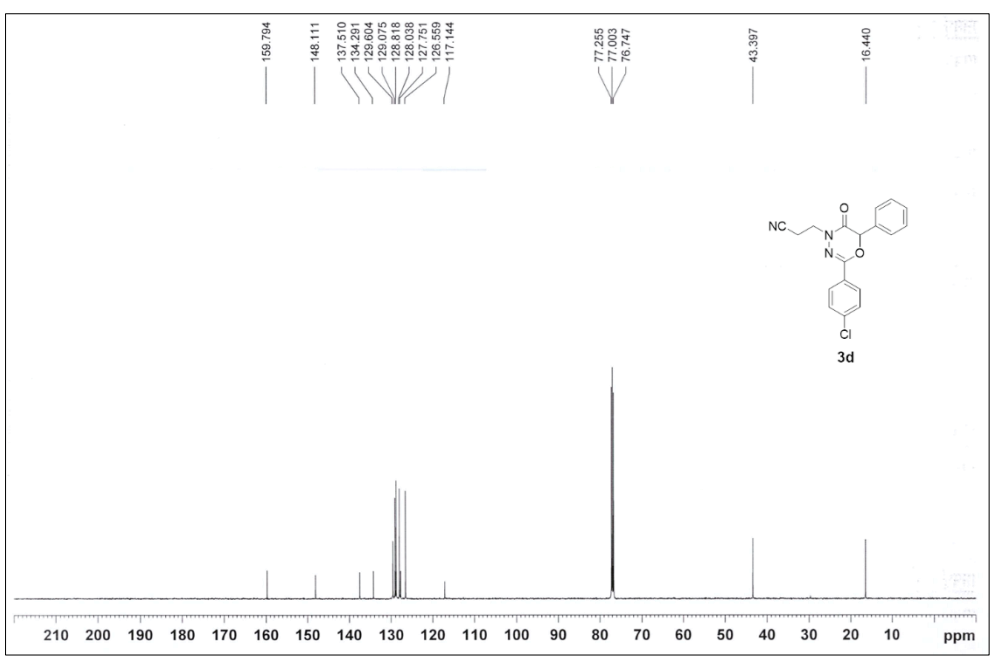

^{1}H-NMR of compound **3e** (500 MHz, $CDCl_3$)

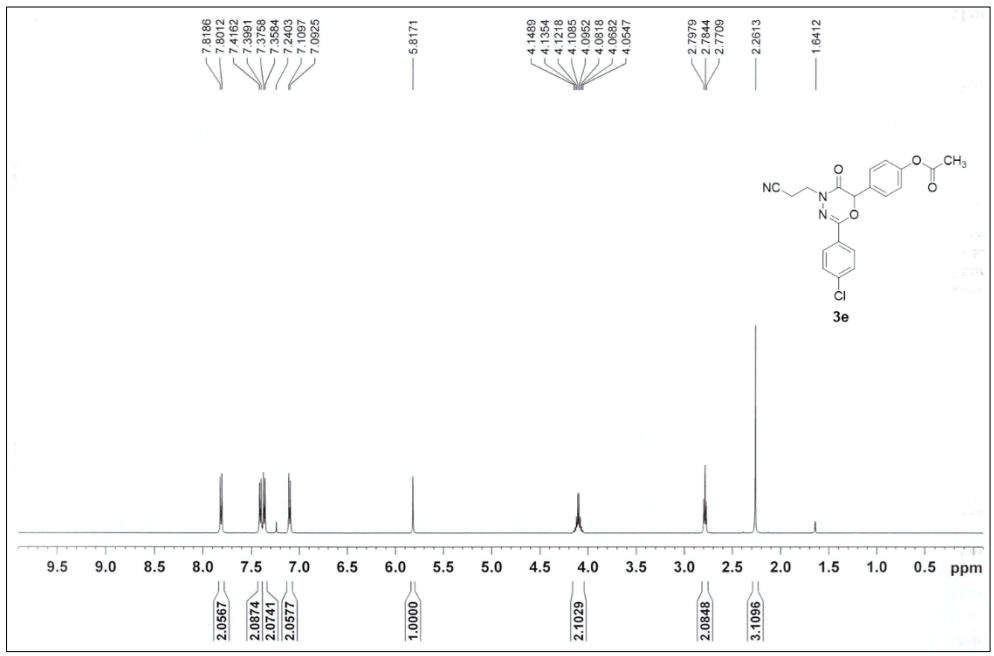

^{13}C-NMR of compound **3e** (125 MHz, $CDCl_3$)

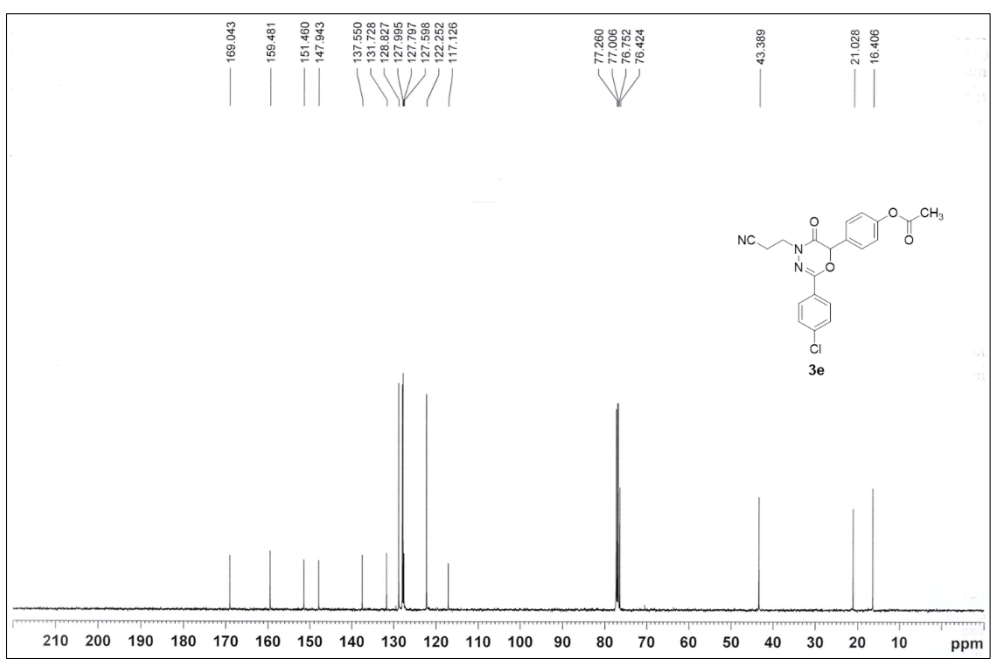

^{1}H-NMR of compound **3f** (500 MHz, $CDCl_3$)

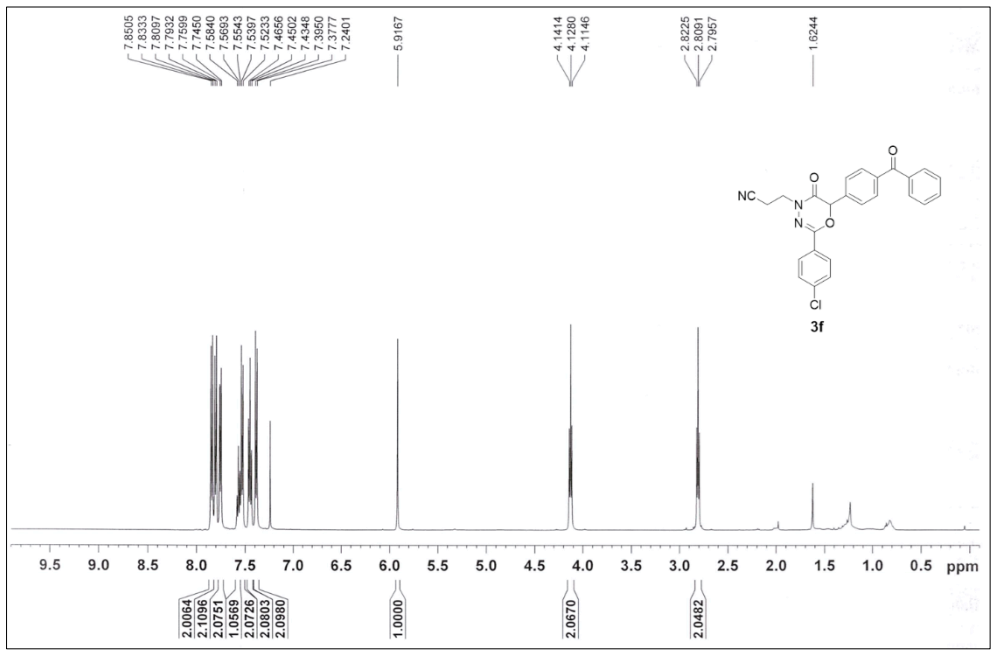

^{13}C-NMR of compound **3f** (125 MHz, $CDCl_3$)

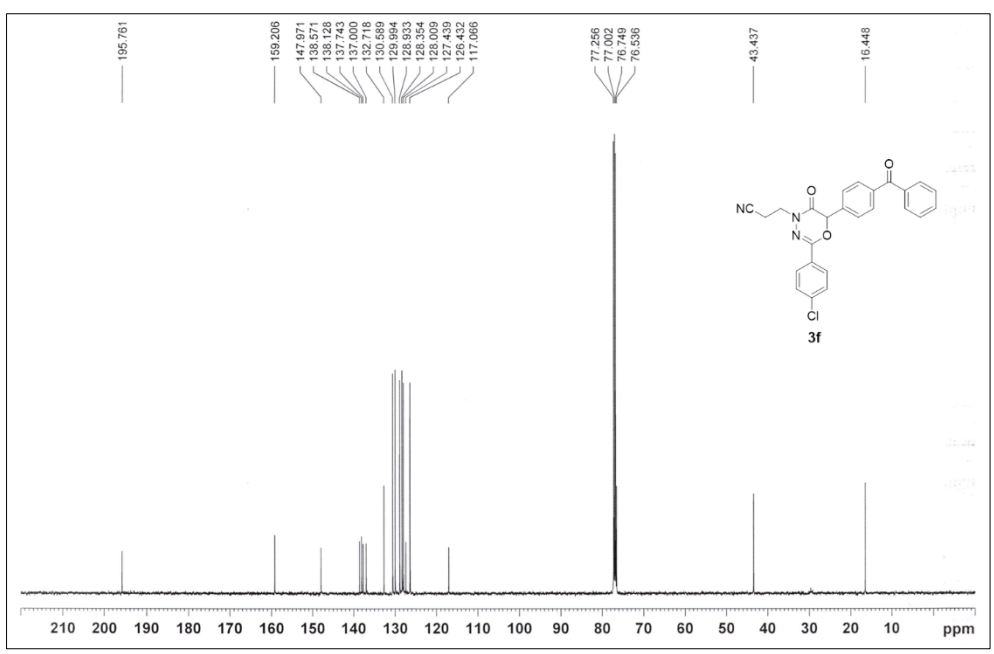

^{1}H-NMR of compound **3g** (600 MHz, $CDCl_3$)

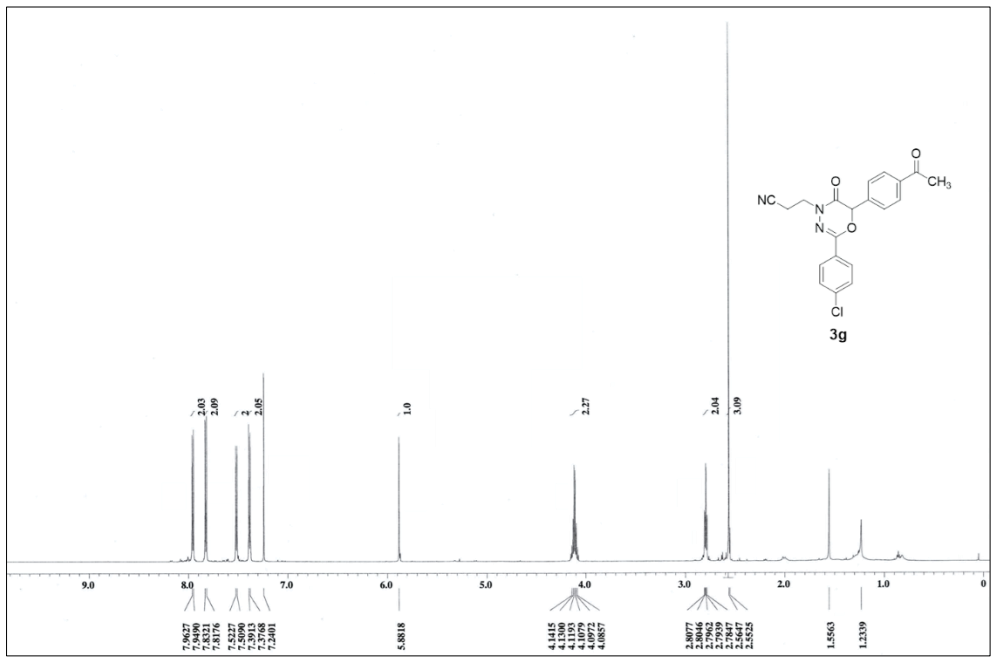

^{13}C-NMR of compound **3g** (150 MHz, $CDCl_3$)

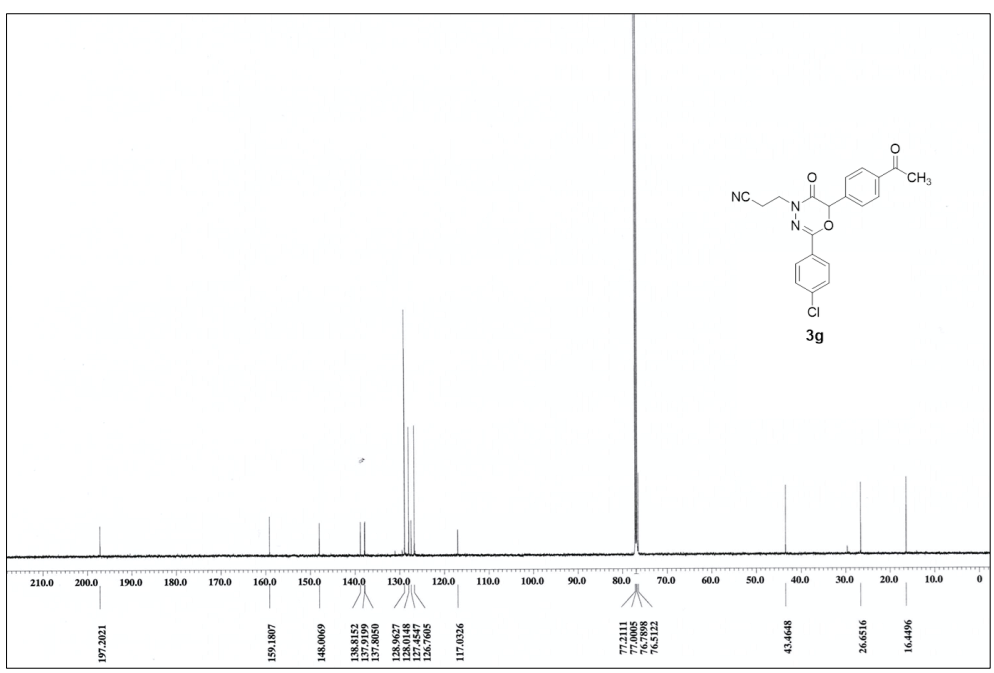

^{1}H-NMR of compound **3h** (500 MHz, $CDCl_3$)

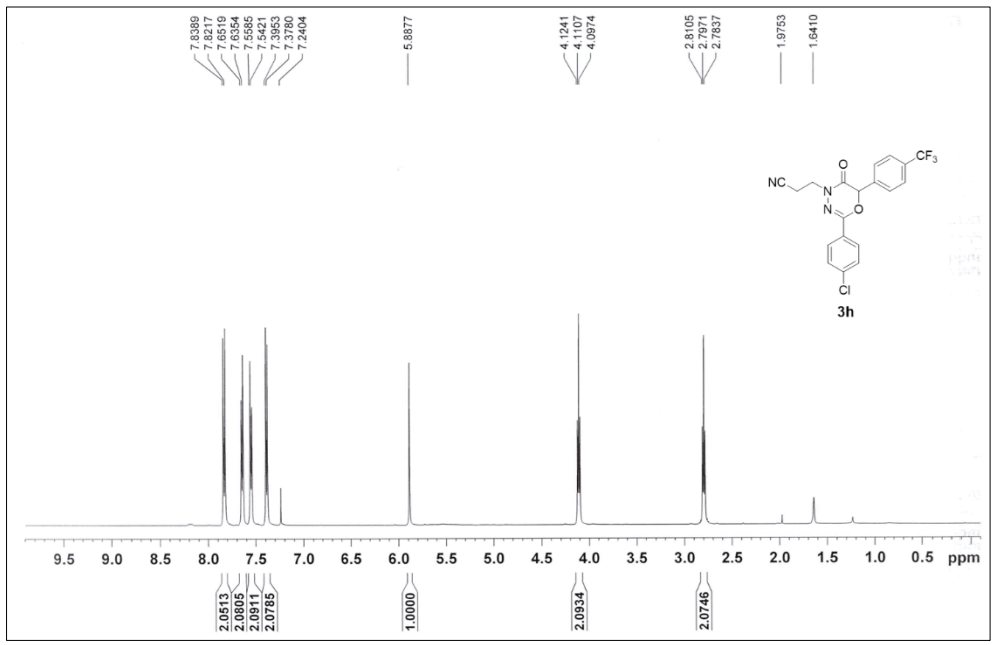

^{13}C-NMR of compound **3h** (125 MHz, $CDCl_3$)

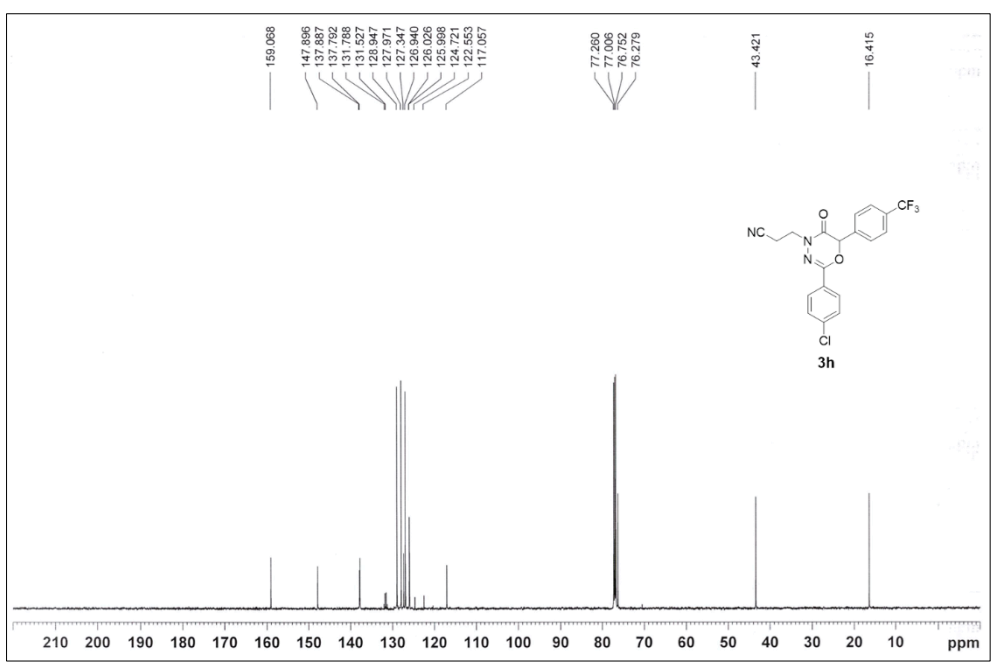

^{1}H-NMR of compound **3i** (500 MHz, $CDCl_3$)

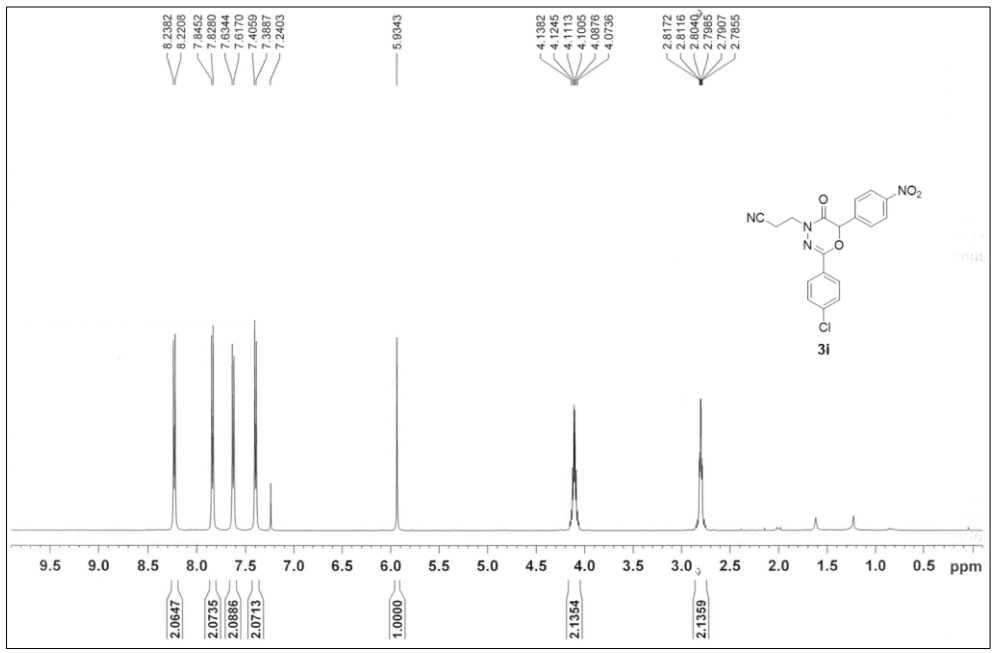

^{13}C-NMR of compound **3i** (125 MHz, $CDCl_3$)

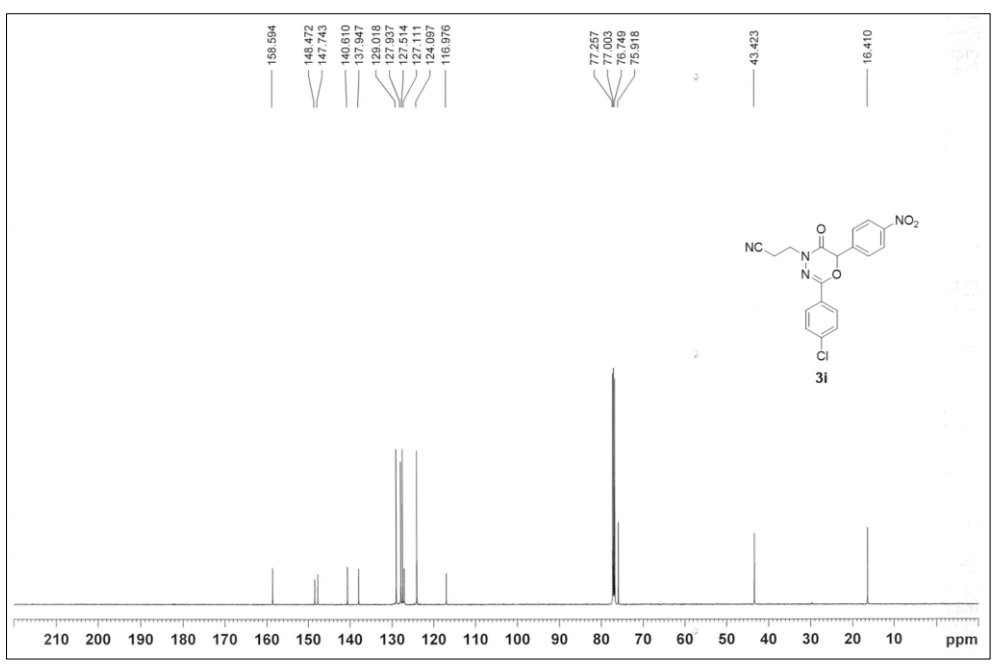

^{1}H-NMR of compound **3j** (400 MHz, $CDCl_3$)

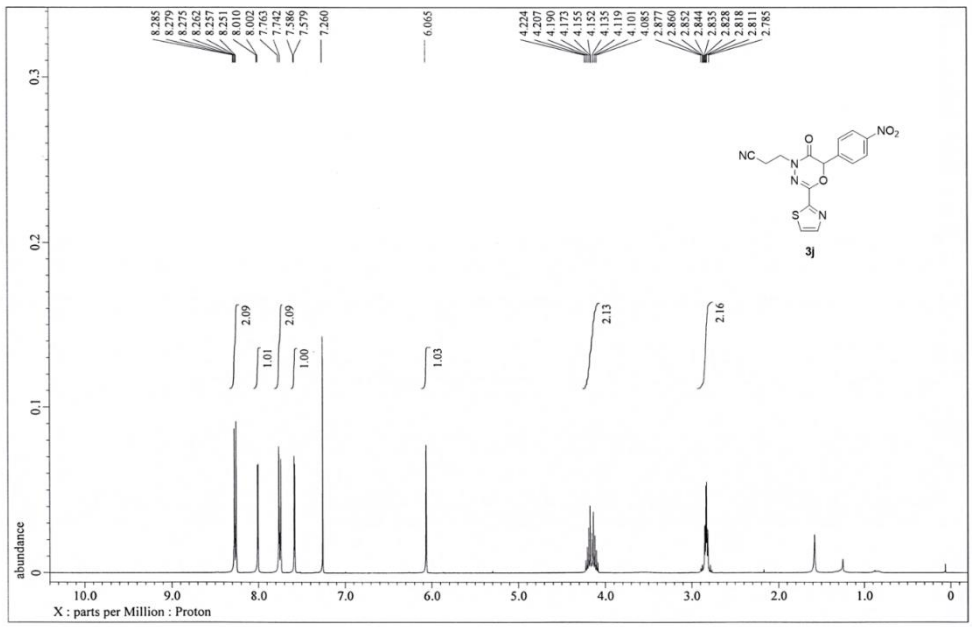

^{13}C-NMR of compound **3j** (100 MHz, $CDCl_3$)

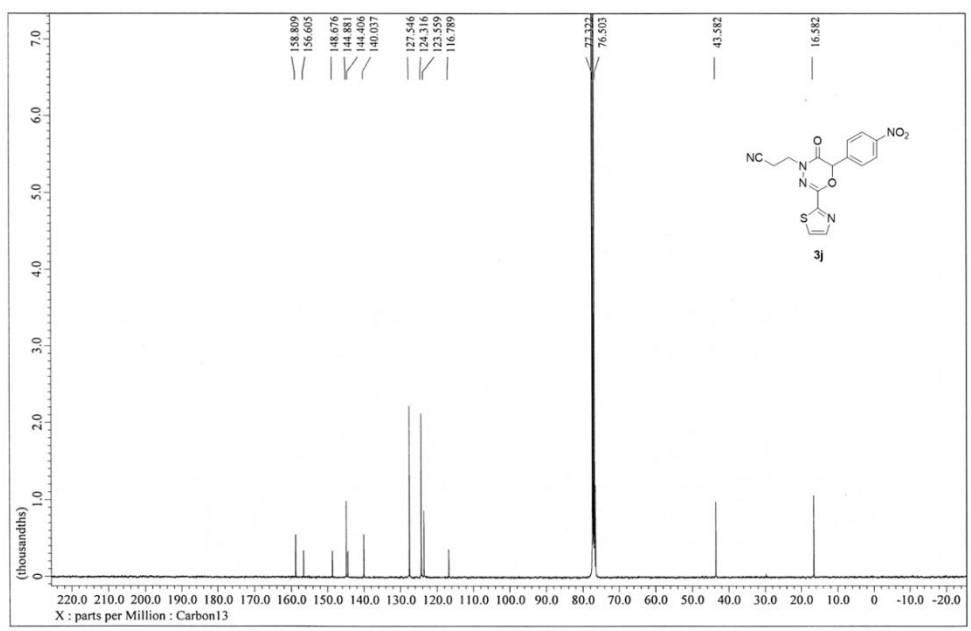

^{1}H-NMR of compound **5a** (600 MHz, $CDCl_3$)

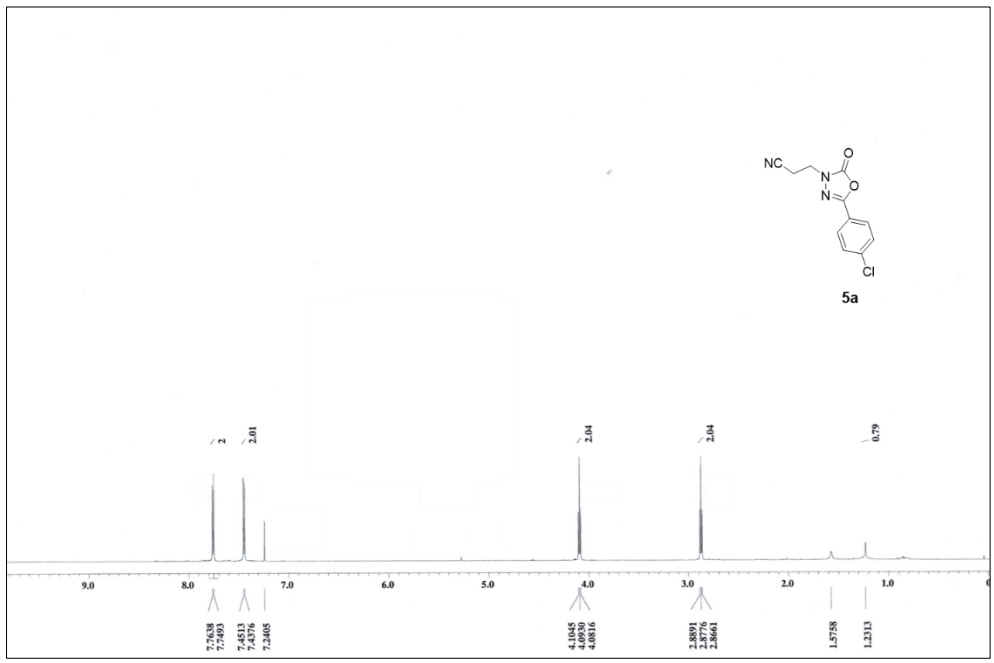

^{13}C-NMR of compound **5a** (150 MHz, $CDCl_3$)

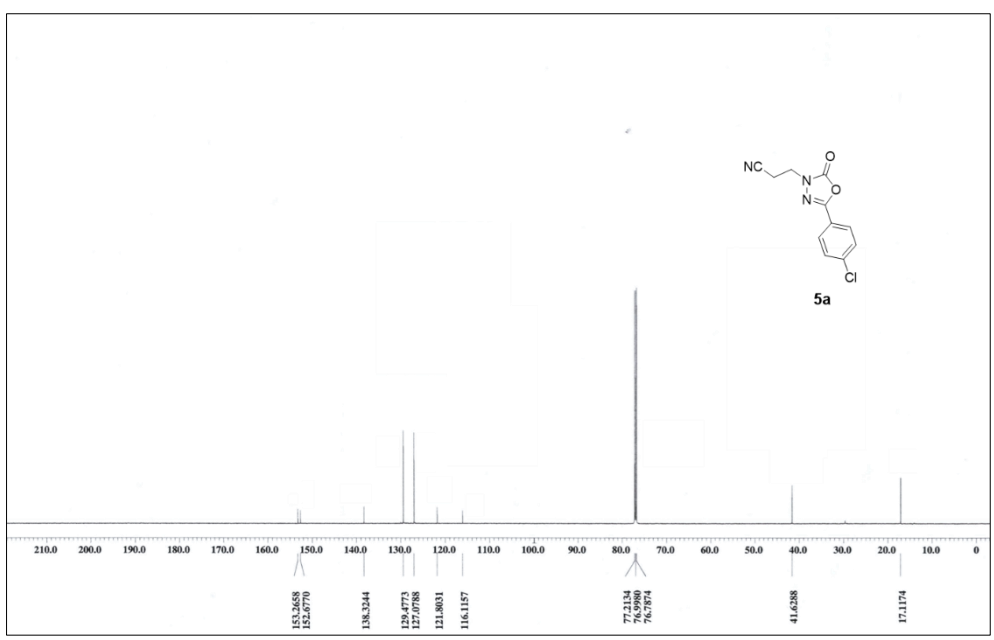

^{1}H-NMR of compound **5b** (800 MHz, $CDCl_3$)

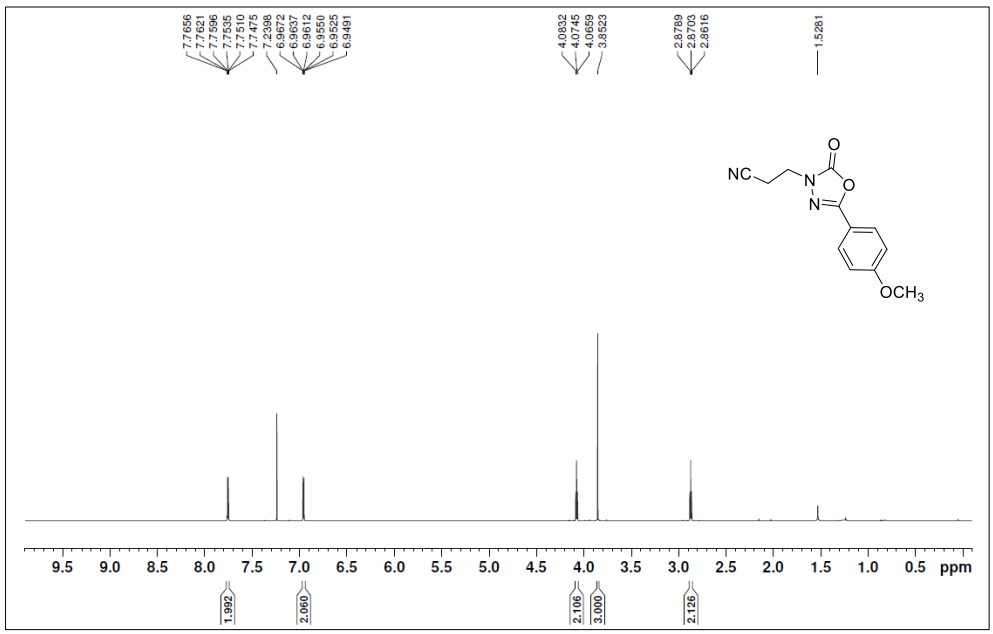

^{13}C-NMR of compound **5b** (200 MHz, $CDCl_3$)

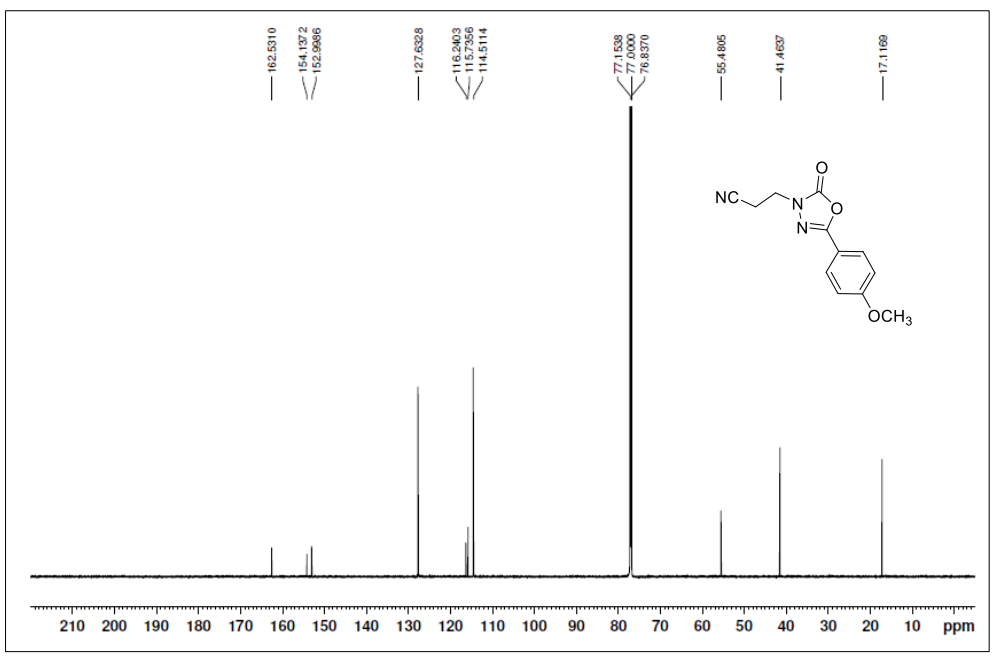

^{1}H-NMR of compound **5c** (400 MHz, $CDCl_3$)

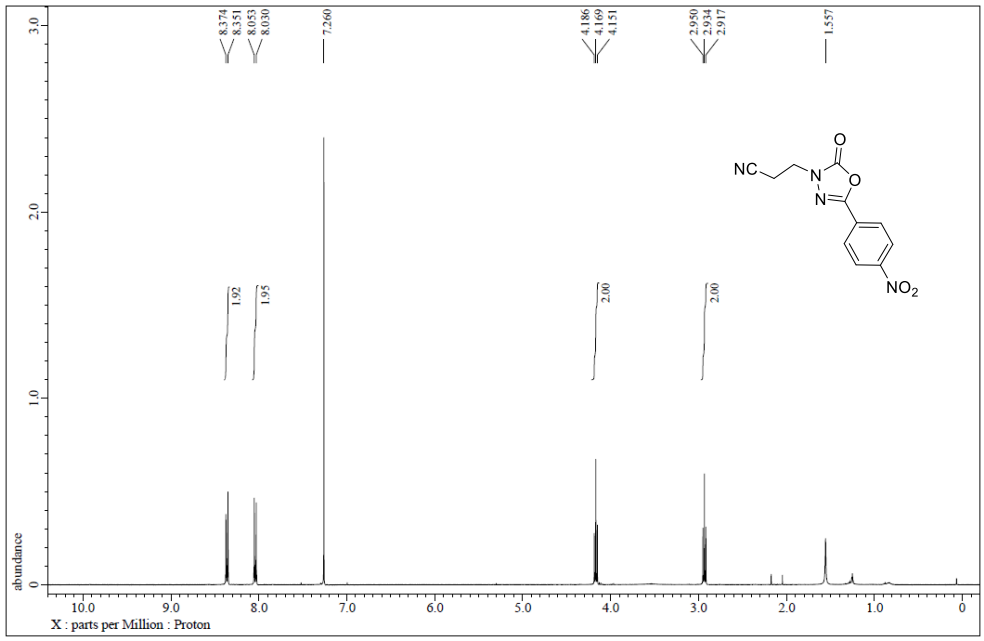

^{13}C-NMR of compound **5c** (100 MHz, $CDCl_3$)

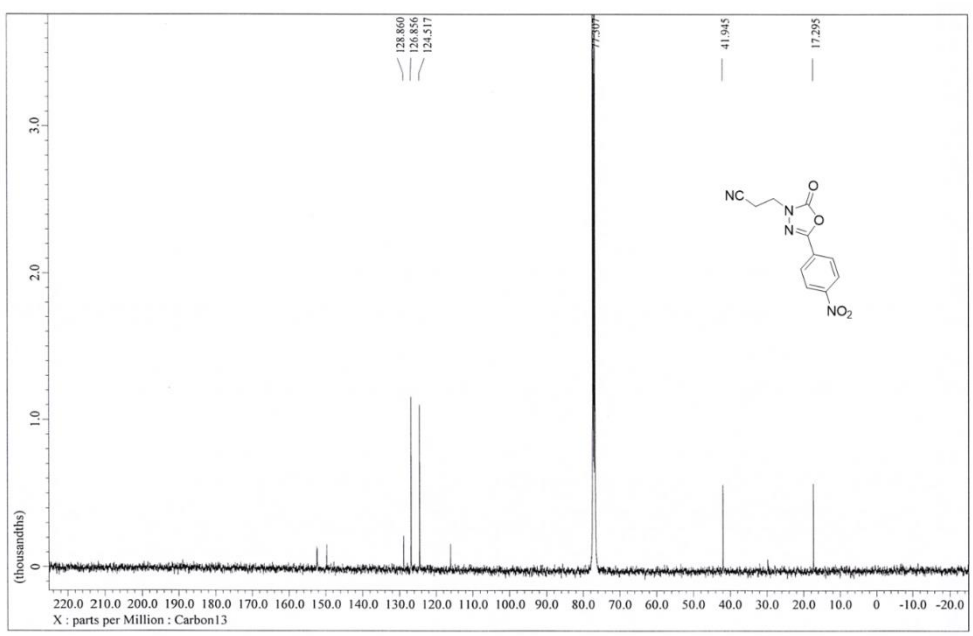

^{1}H-NMR of compound **5d** (400 MHz, $CDCl_3$)

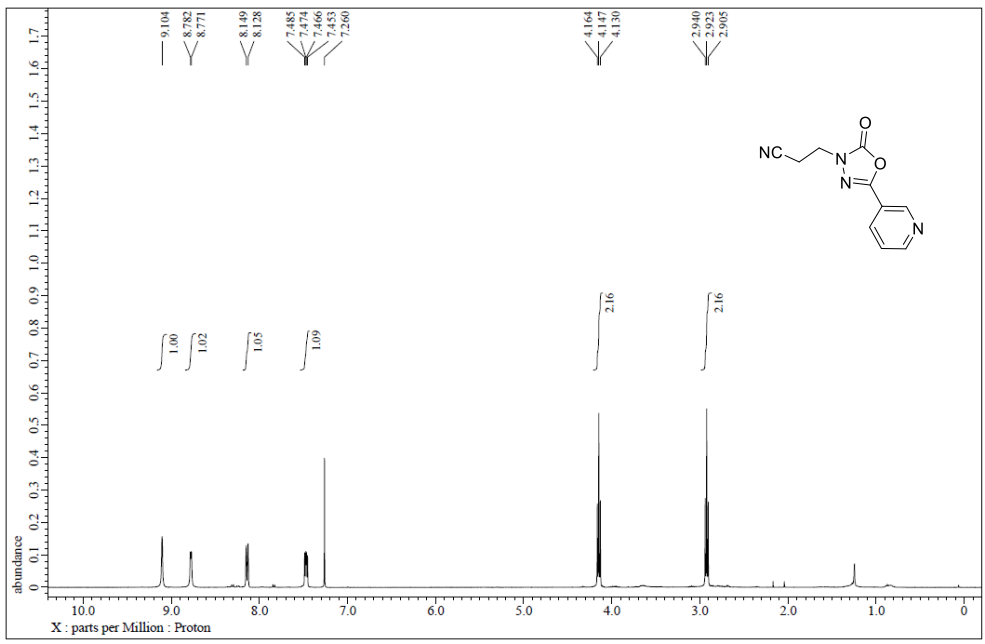

^{13}C-NMR of compound **5d** (200 MHz, $CDCl_3$)

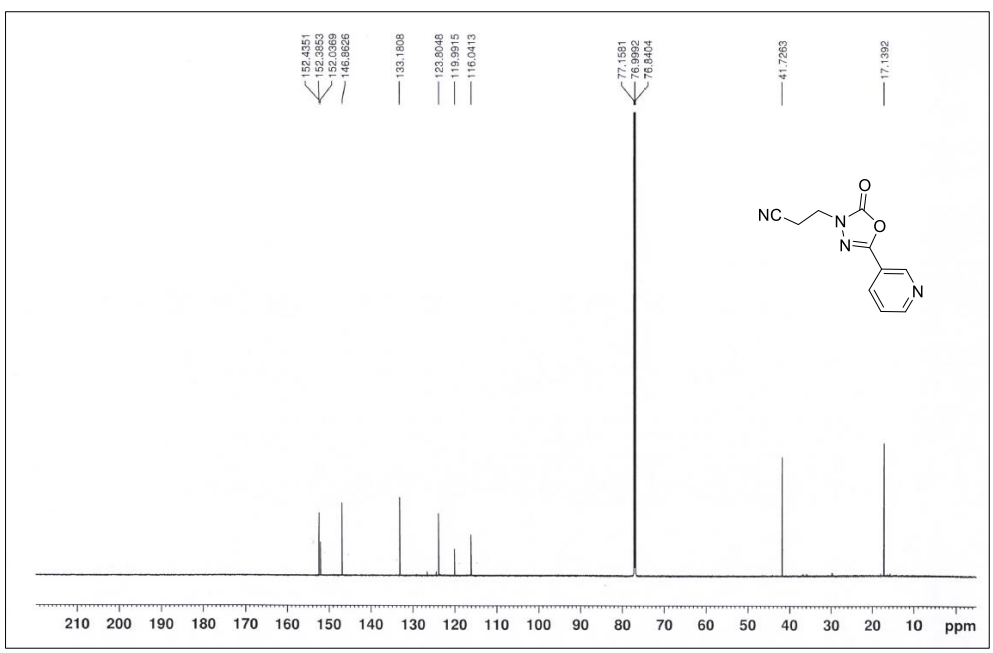

^{1}H-NMR of compound **5e** (400 MHz, $CDCl_3$)

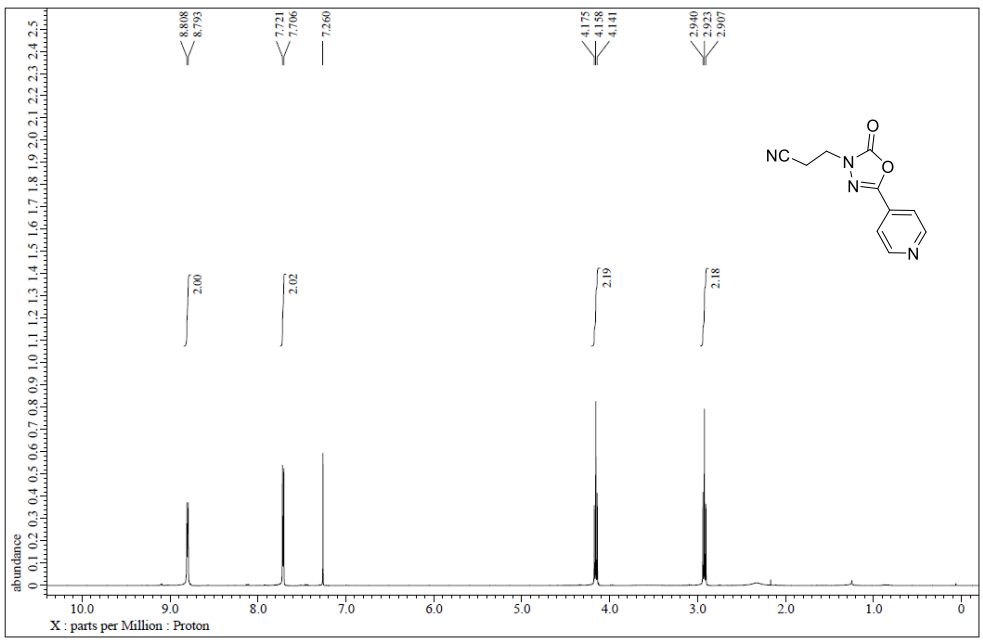

^{13}C-NMR of compound **5e** (200 MHz, $CDCl_3$)

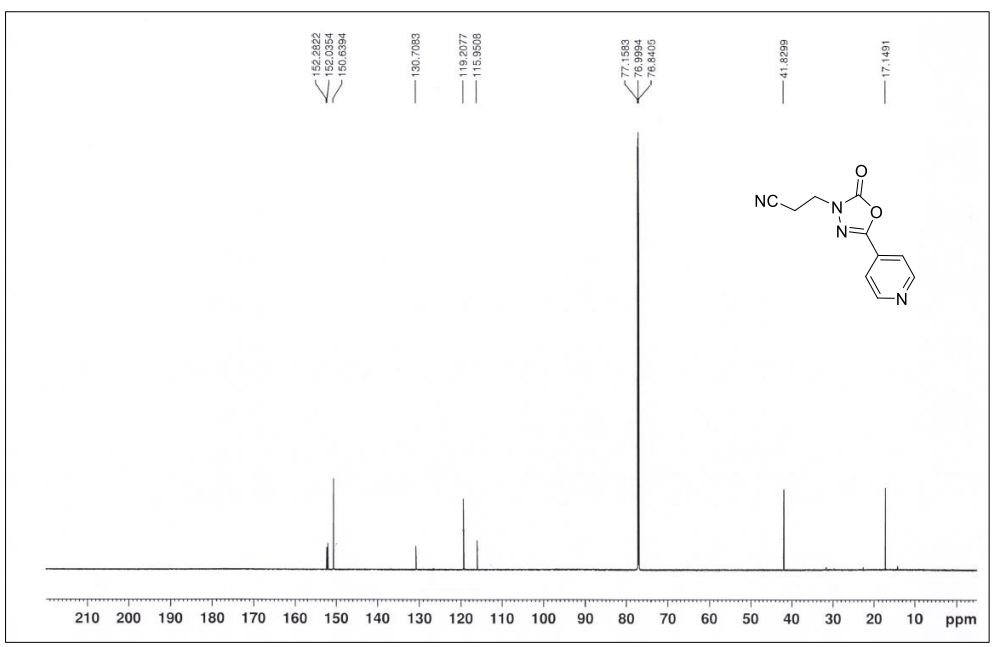

^{1}H-NMR of compound **4** (800 MHz, DMSO-d_6)

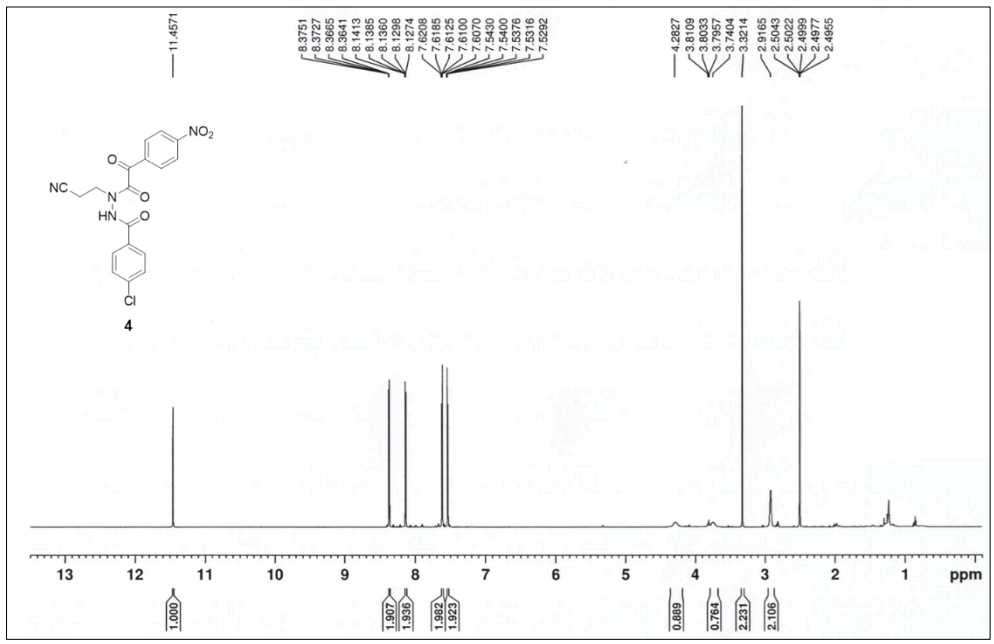

^{13}C-NMR of compound **4** (200 MHz, DMSO-d_6)

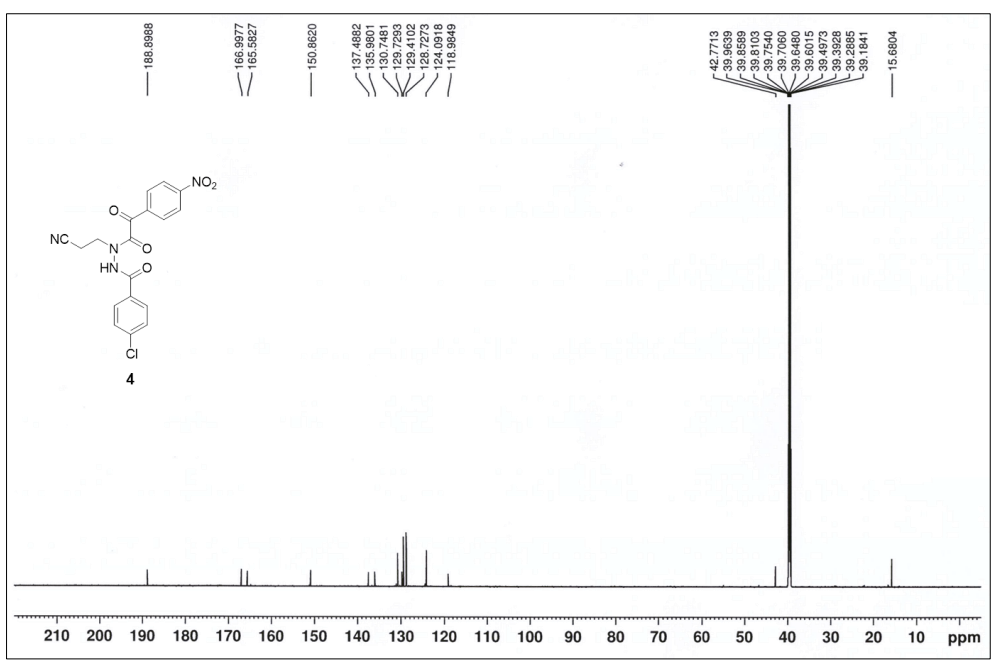

^{1}H-NMR of **OPAL-6** (400 MHz, $CDCl_3$)

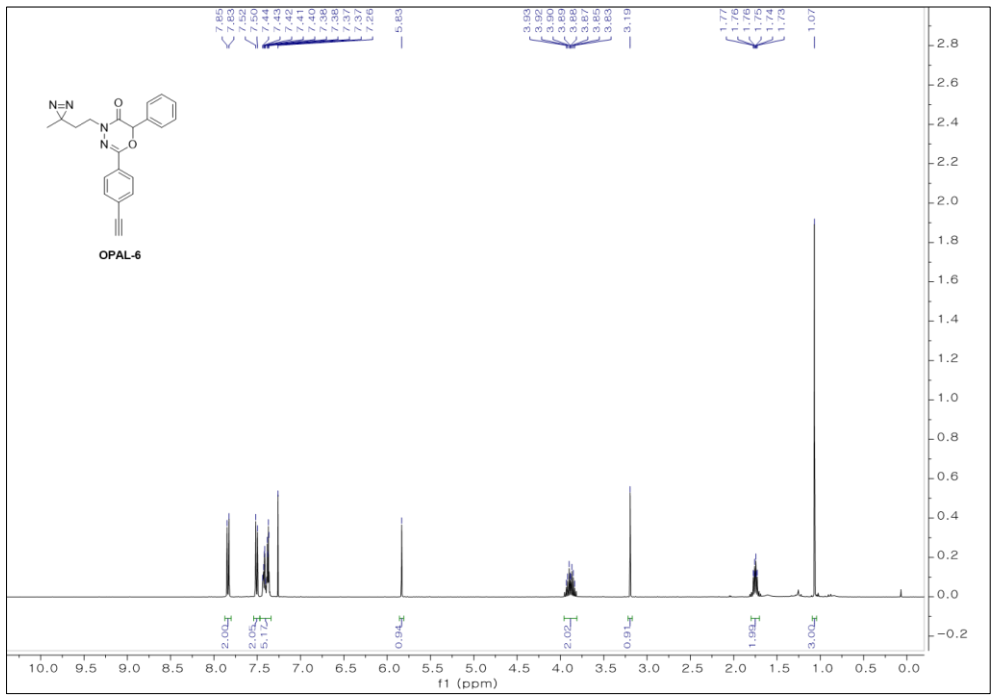

^{13}C-NMR of **OPAL-6** (100 MHz, $CDCl_3$)

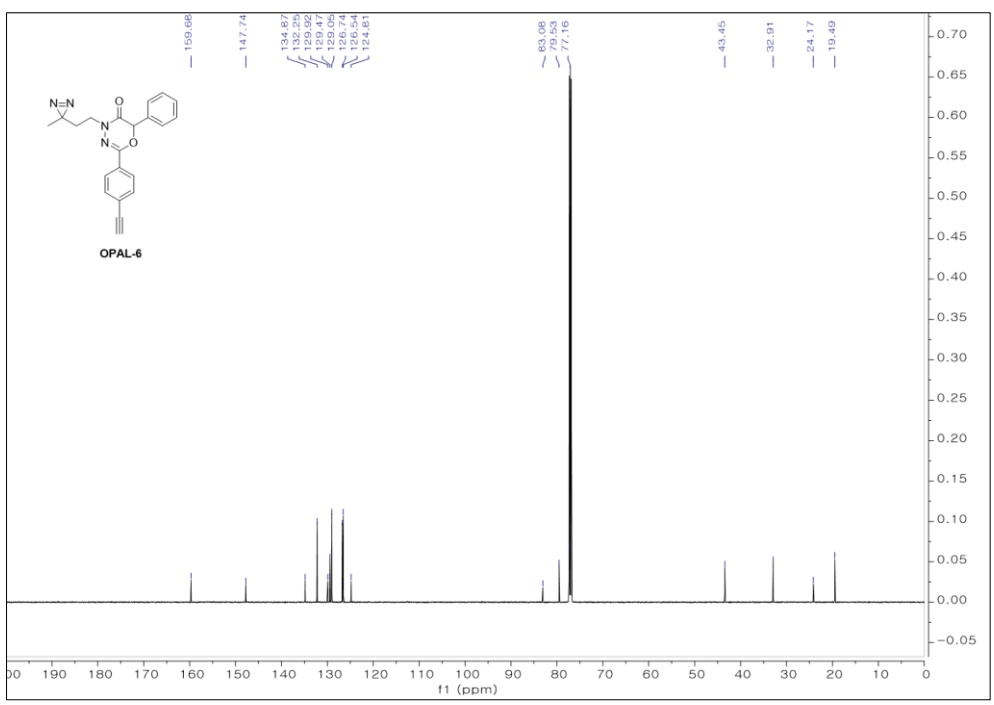

^{1}H-NMR of **OPAL-8** (400 MHz, $CDCl_3$)

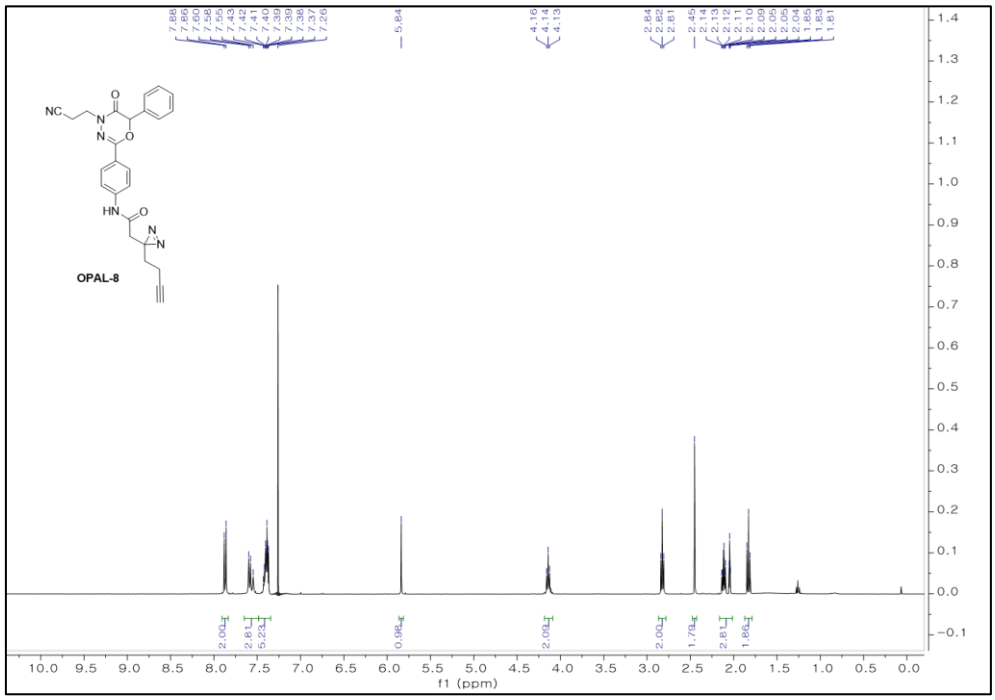

^{13}C-NMR of **OPAL-8** (100 MHz, $CDCl_3$)

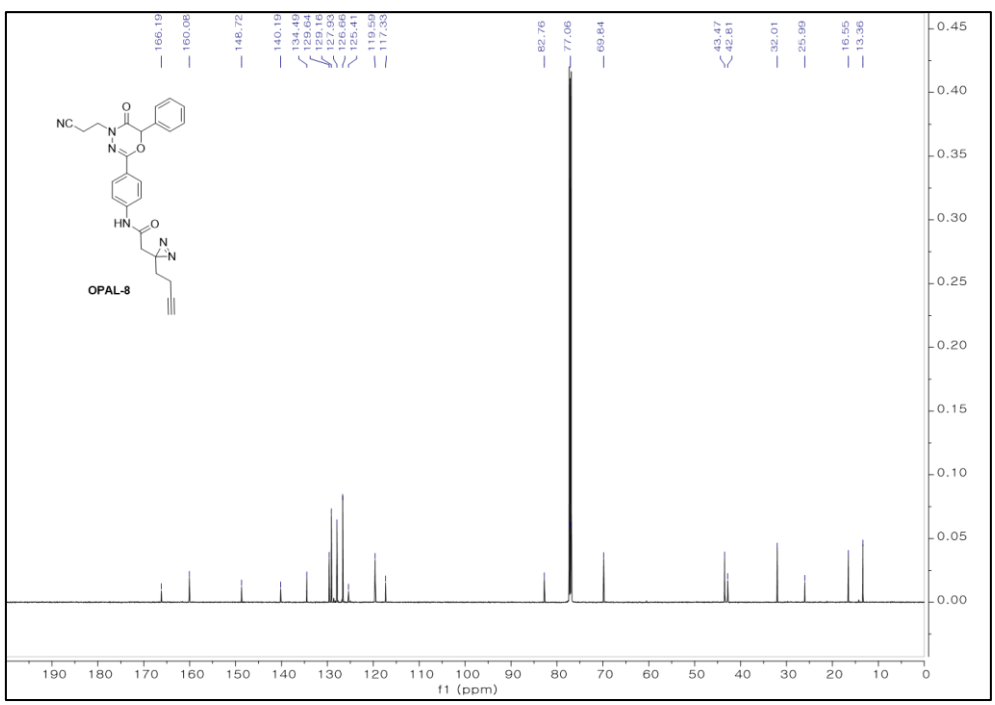

^{1}H-NMR of **OPAL-10** (600 MHz, $CDCl_3$)

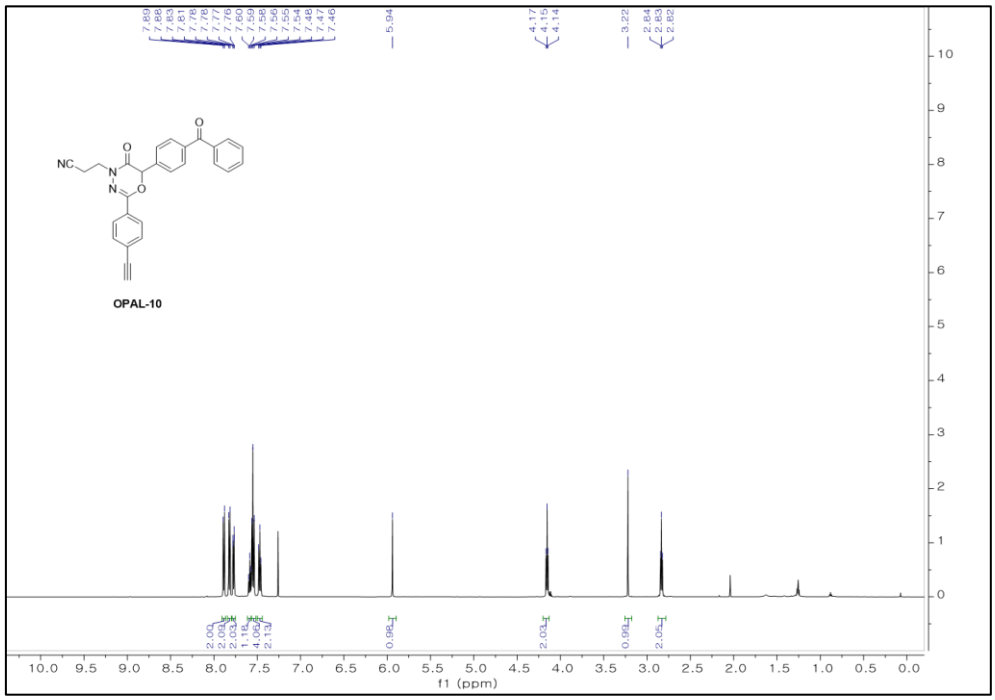

^{13}C-NMR of **OPAL-10** (150 MHz, $CDCl_3$)

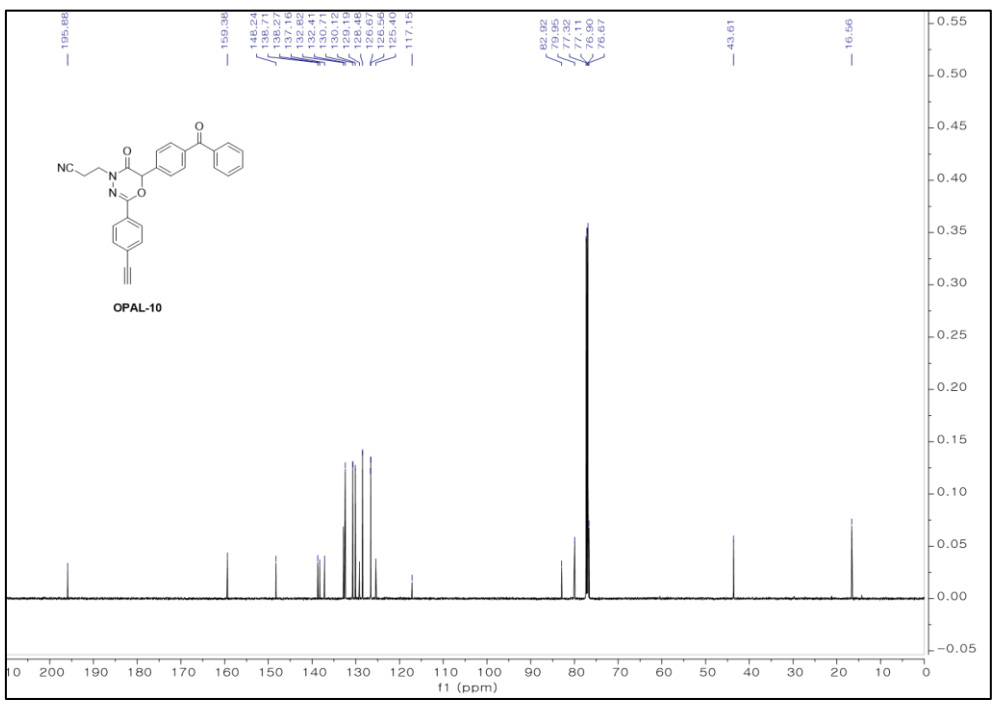

^{1}H-NMR of compound **IQ44** (500 MHz, $CDCl_3$)

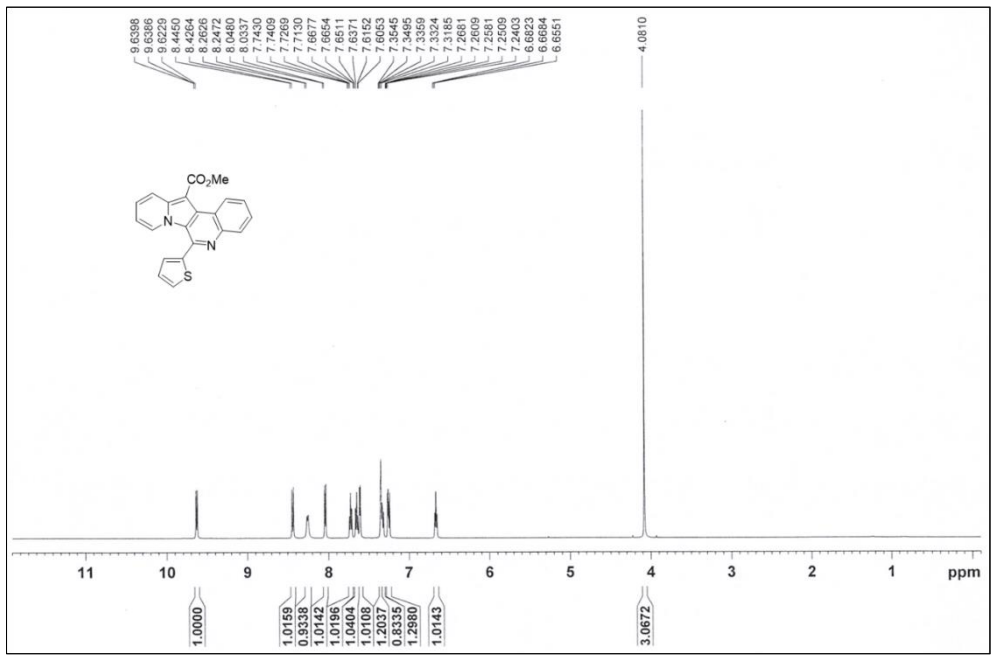

^{13}C-NMR of compound **IQ44** (125 MHz, $CDCl_3$)

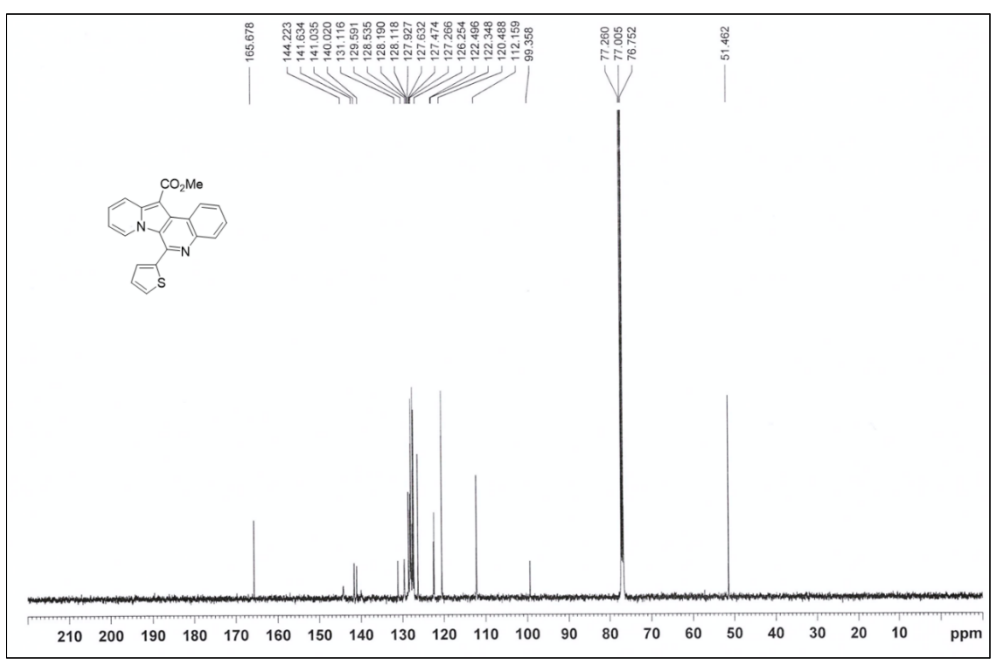

^{1}H-NMR of compound **IQ-B27** (400 MHz, $CDCl_3$)

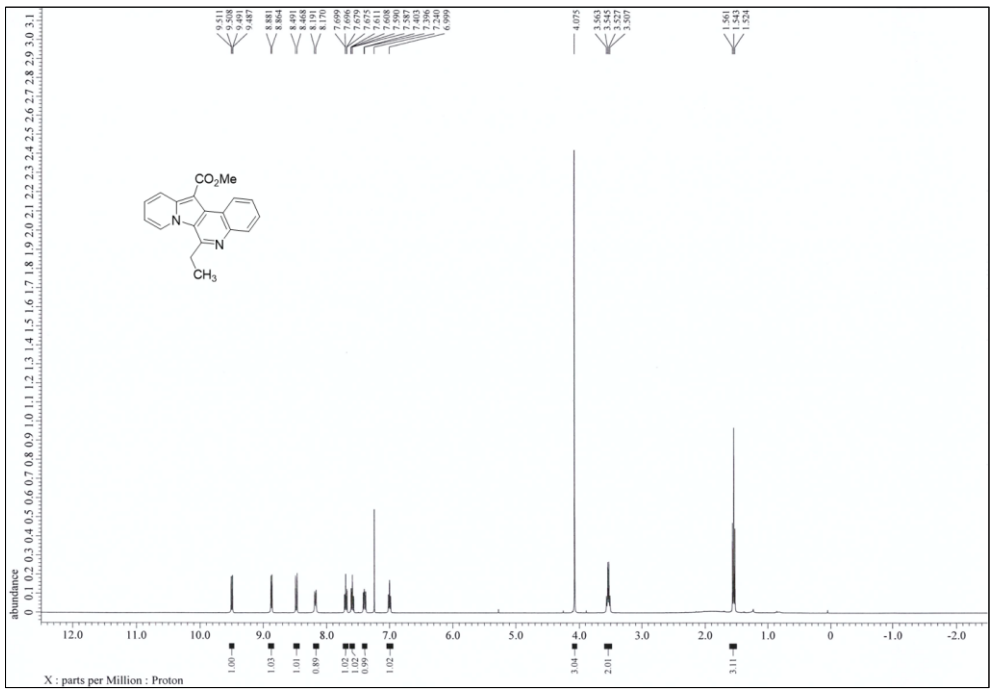

^{13}C-NMR of compound **IQ-B27** (100 MHz, $CDCl_3$)

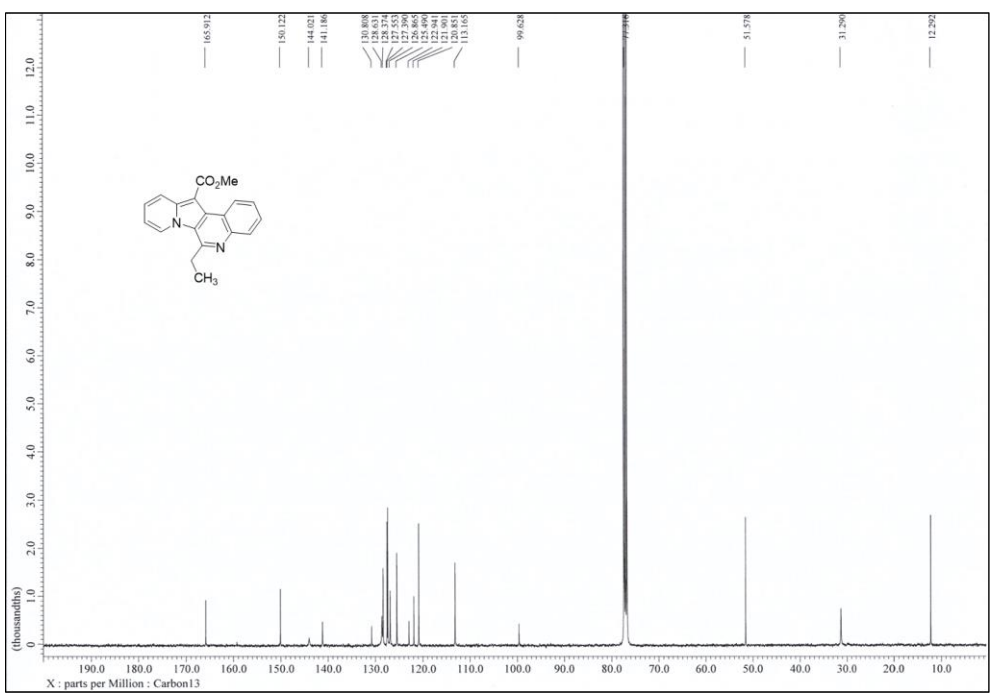

^{1}H-NMR of compound **IQ-B28** (400 MHz, $CDCl_3$)

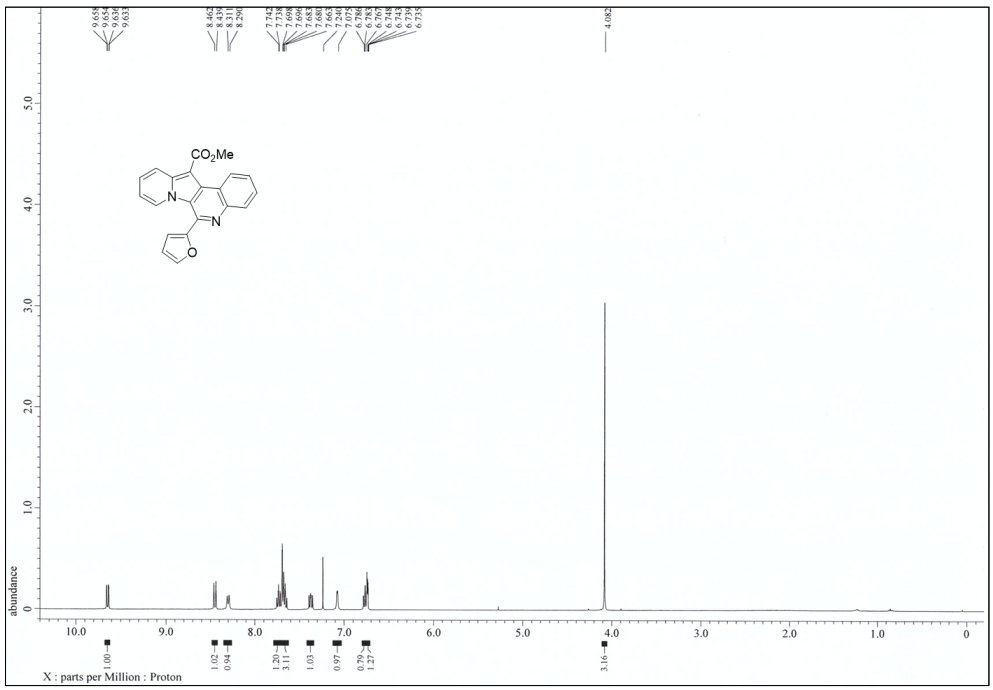

^{13}C-NMR of compound **IQ-B28** (100 MHz, $CDCl_3$)

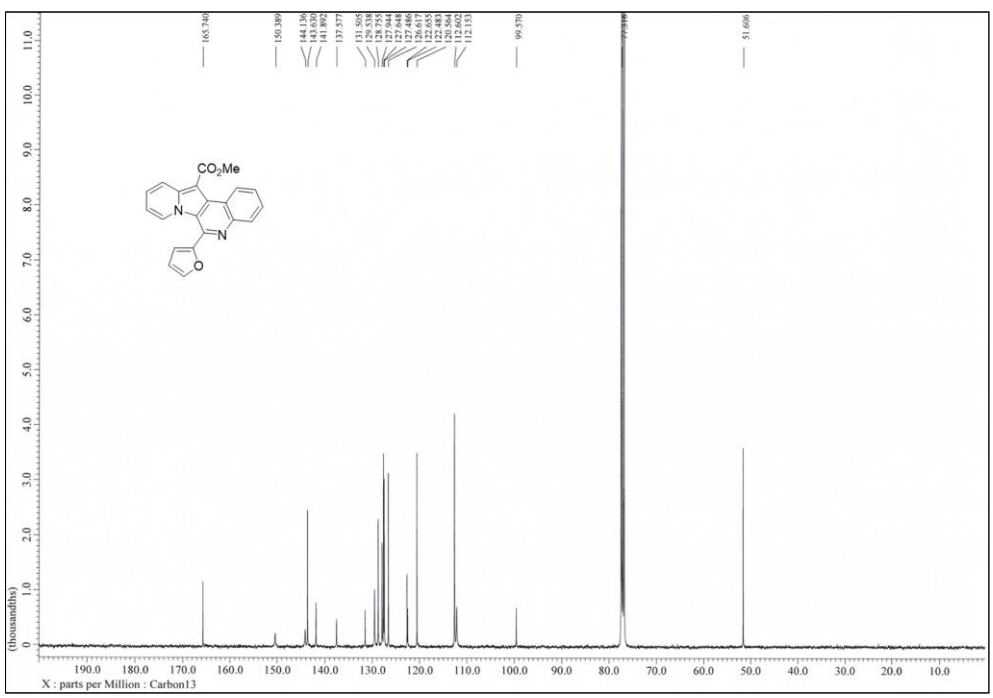

^{1}H-^{1}H COSY NMR of compound **IQ44** (800 MHz, CD_3OD)

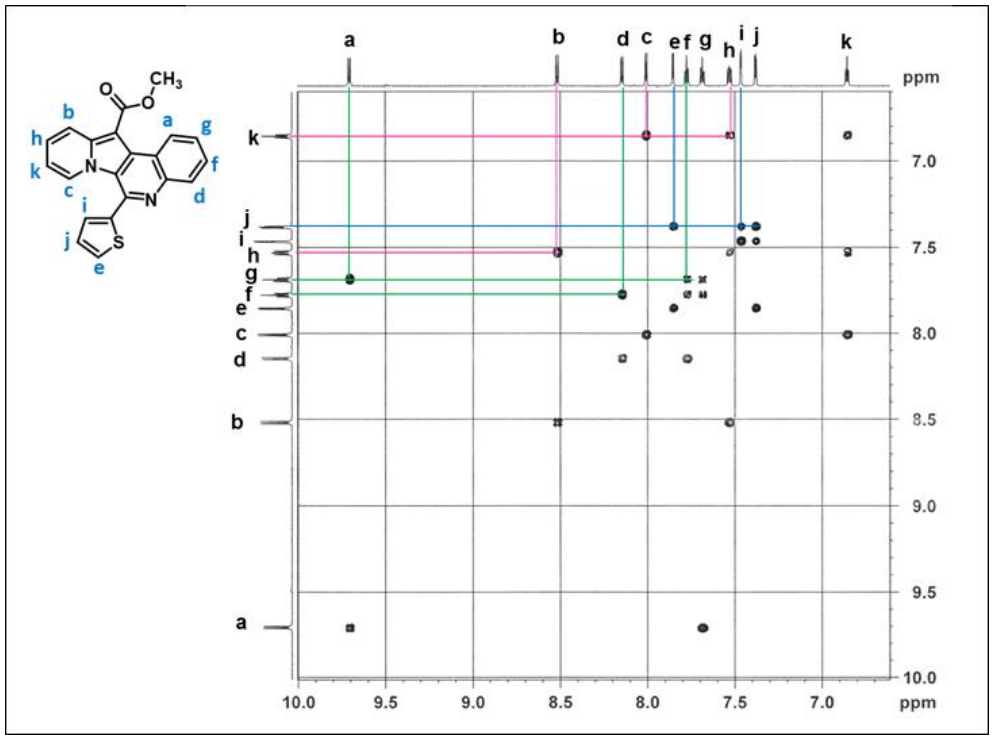

^{1}H-^{1}H NOESY NMR of compound **IQ44** (800 MHz, CD_3OD)

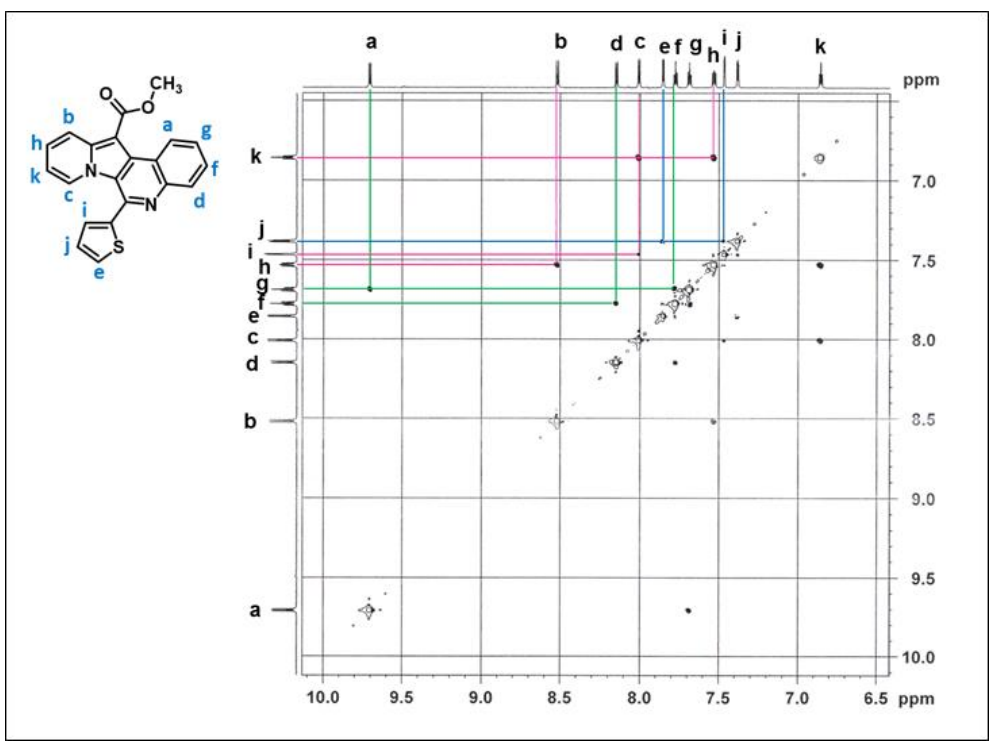

^{1}H-^{1}H COSY NMR of compound **IQ44**-Fe^{3+} (800 MHz, CD_3OD)

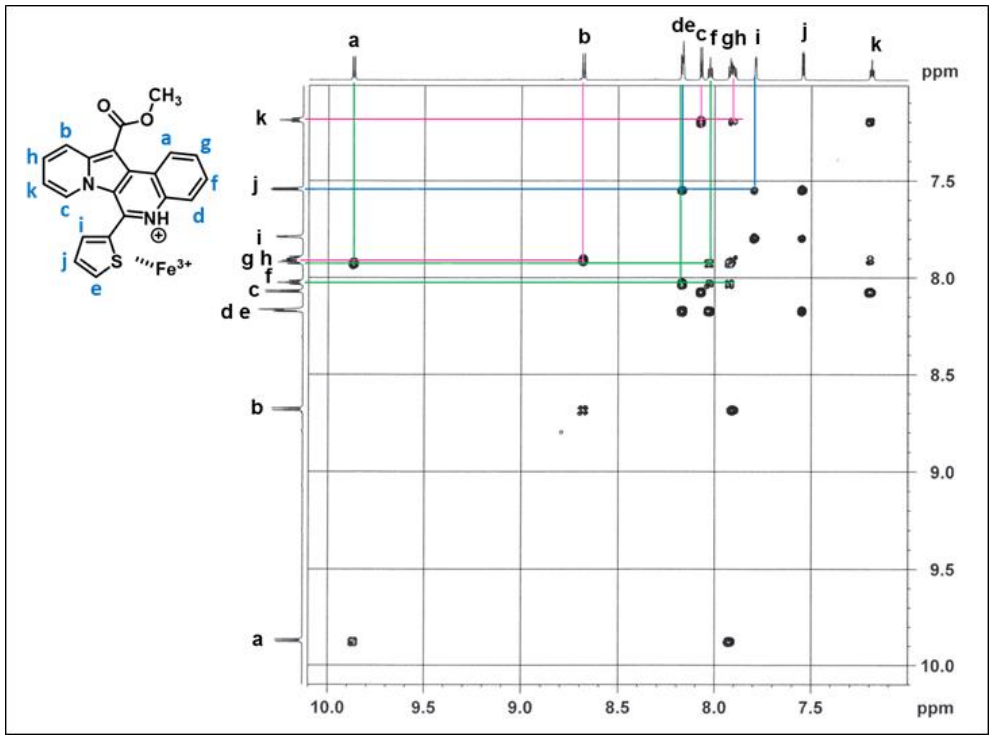

^{1}H-^{1}H NOESY NMR of compound **IQ44**-Fe^{3+} (800 MHz, CD_3OD)

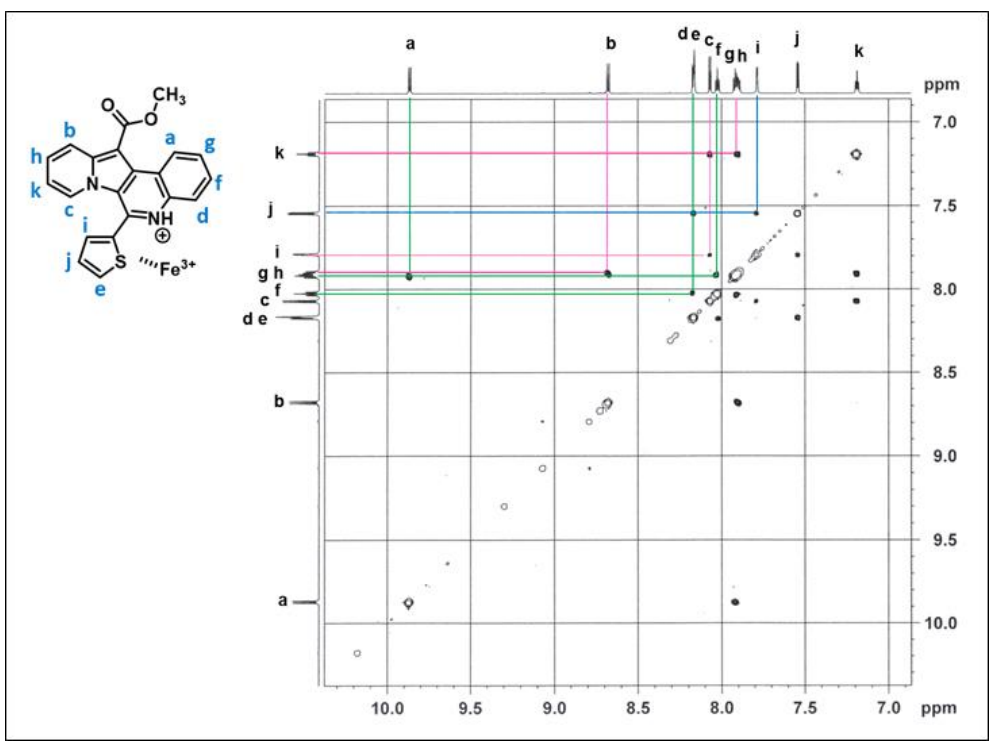

VII. 국문초록

I. Metal-free and mild approach to 1,3,4-oxadiazol-2(3*H*)-ones via oxidative C-C bond cleavage of 1,3,4-oxadiazin-5(6*H*)-ones

산화성 탄소-탄소 결합 분해반응을 수반한 1,3,4-oxadiazin-5(6*H*)-ones 으로부터 1,3,4-oxadiazol-2(3*H*)-ones의 전환

본 연구에서는 금속을 사용하지 않은 온화한 반응 조건 하에서 1,3,4-oxadiazin-5(6*H*)-one이 산화성의 탄소-탄소 결합 분해 반응 (oxidative C-C bond cleavage)을 통해 1,3,4-oxadiazol-2(3*H*)-one 구조로 전환되는 새로운 합성법을 개발하였다. 이 새로운 전환 반응은 α-carbonyl 위치에 있는 phenyl기의 *p*-위치에 전자 당김 작용기 (electron donating group)에 의해 촉진되며 산소 분자에 의한 산화성 하이드록실화 반응(oxidative hydroxylation)에 이은 탄소-탄소 결합 분해반응을 통해 일어난다는 것을 확인하였다. 전이 금속 촉매나 산화제, 어떠한 첨가제 없이 산소 존재 하에 K_2CO_3를 이용하는 유독하지 않은 반응 조건으로 용이하게 1,3,4-oxadiazol-2(3*H*)-one을 합성할 수 있었다. 또한 이 반응의 조건을 조절함으로써 1,3,4-oxadiazin-5(6*H*)-one과 1,3,4-oxadiazol-2(3*H*)-one, 중간체인 α-keto-maide을 선택적으로 생성할 수 있었다.

주요어 : 1,3,4-oxadiazol-2(3*H*)-one, 1,3,4-oxadiazin-5(6*H*)-one, Oxidative C-C bond cleavage, Metal free reaction, molecular oxygen

학 번 : 2014-31255

II. Target identification of a 1,3,4-oxadiazin-5(6*H*)-one anticancer agent *via* photoaffinity labelling

항암 활성물질의 표적 규명을 위한 1,3,4-oxadiazin-5(6*H*)-ones 구조 기반의 화학 프로브 개발

생물학적 활성 물질에 의한 표적 단백질의 규명에 쓰이는 광반응 표지 (Photoaffinity labelling, PAL) 물질 개발에 있어서 합리적 분자 설계와 합성의 용이성은 매우 중요한 요소이다. 본 연구에서는 IGF-1R과 Src를 이중 타겟으로 하는 항암활성 물질인 LL-2003을 바탕으로 1,3,4-oxadiazin-5(6*H*)-ones 구조 기반의 광반응 표지 물질 (Oxa-photoaffinity labelling probe, OPAL)을 성공적으로 합성하였다. 또한 OPAL-6과 OPAL-8 프로브는 MCF7, A549, HepG2, HeLa의 암세포에 대해 live cell과 cell lysate 상태 모두에서 공유결합 형성을 통하여 표적 단백질에 성공적으로 표지되는 것을 확인하였다. OPAL 프로브를 이용한 *in vitro*와 *in situ* 표지 실험을 통하여 각각의 단백질 발현의 정도와 양상이 세포에 따라 다른 것을 발견하였고 그 중 A549 세포의 Src 단백질을 가장 잘 표지하는 결과를 얻었다. OPAL-6과 OPAL-8 프로브로 IGF-1R이 과발현된 곤충세포를 이용한 표적 확인 실험을 진행하였고 in-gel 형광 결과와 더불어 LC-MS/MS 분석을 통해 IGF-1R과의 결합 위치를 확인하였다.

주요어 : Photoaffinity labelling, Target identification, 1,3,4-oxadiazin-5(6*H*)-ones, IGF-1R, Src

학 번 : 2014-31255

III. Novel turn-on fluorescent biosensors for selective detection of cellular Fe^{3+} in lysosomes

라이소좀 선택적 철 (Fe^{3+}) 탐지를 위한 새로운 바이오 형광 센서의 개발

선택적인 철 이온의 형광 센서는 철과 연관된 세포 사멸 기전과 나아가 인체 질병의 이해에 있어서 필수적인 도구 화합물이다. 본 연구에서는 높은 선택성으로 Fe^{3+}를 감지하는 indolizino[3,2,c]quinolone (IQ) 골격에 기반한 새로운 유형의 형광 센서를 개발하였다. IQ44는 에탄올뿐만 아니라 물에서도 Fe^{3+}를 감지하여 형광 증가를 보였다. 수용액 상에서 IQ44는 150 nm 정도의 크기의 나노 입자를 형성하였고, 물에서의 나노 입자 상태일 때에는 형광이 감소하였다가 Fe^{3+}를 감지하였을 때에는 형광이 증가하였다. IQ 형광 센서 유도체들의 구조-기능 상관관계 분석을 통하여 IQ44의 선택적 Fe^{3+}의 감지는 thiophene 고리에 의한 것임을 알아냈고, Fe^{3+}와의 결합으로 인해 thiophene 고리의 회전이 제한됨에 따라 형광 증가를 보이는 것을 밝혔다.

공초점 형광 현미경 관찰을 통해 IQ44가 세포 내에서 Fe^{3+}를 감지하여 형광 증가를 보이는 것을 확인하였고 또한 라이소좀에 특이적으로 잘 위치하는 것을 확인하였다. 더불어 pmRPF-LC3를 감염시킨 autophagosome과 IQ44가 동일하게 위치함과 동시에 형광 증가가 관찰되어 Fe^{3+}가 관여하는 autophagy과정 역시 관찰할 수 있음을 확인하였다.

주요어 : Fluorescent biosensor, Fe^{3+} sensor, Indolizino[3,2,*c*]quinolone, Lysosome, Autophage

학 번 : 2014-31255